

2-7-2008

Advanced parallel magnetic resonance imaging methods with applications to MR spectroscopic imaging

Ricardo Otazo

Follow this and additional works at: https://digitalrepository.unm.edu/ece_etds

Recommended Citation

Otazo, Ricardo. "Advanced parallel magnetic resonance imaging methods with applications to MR spectroscopic imaging." (2008).
https://digitalrepository.unm.edu/ece_etds/196

This Dissertation is brought to you for free and open access by the Engineering ETDs at UNM Digital Repository. It has been accepted for inclusion in Electrical and Computer Engineering ETDs by an authorized administrator of UNM Digital Repository. For more information, please contact disc@unm.edu.

Advanced Parallel Magnetic Resonance Imaging Methods with Applications to MR Spectroscopic Imaging

by

Ricardo Otazo

B.Sc., Electrical Engineering, Universidad Católica, Paraguay, 2001

M.Sc., Electrical Engineering, University of New Mexico, USA, 2006

DISSERTATION

Submitted in Partial Fulfillment of the
Requirements for the Degree of

Doctor of Philosophy
Electrical Engineering

The University of New Mexico

Albuquerque, New Mexico

December, 2007

©2007, Ricardo Otazo

Dedication

To my wife Primi, for her infinite patience and support.

Acknowledgments

I would like first to express my sincere gratitude to my main research advisor Stefan Posse. Stefan has been a mentor and a friend who has supported me with no reserves for the last four years. I am also indebted to my advisor at ECE Ramiro Jordan for his unconditional support and guidance. I would like also to thank Fa-Hsuan Lin for fruitful discussions and support to develop my research work at the MGH-HMS-MIT Martinos Center in Boston with large-N array coils. Special thanks to the rest of my thesis committee Arvind Caprihan and Marios Pattichis for their helpful feedback. Thanks go as well to Chuck Gasparovic from the MIND institute for his advice and motivation during my first steps in the MRI field.

A very special thank you goes to my family. I am deeply indebted to them for providing me encouragement and support in every step of the way.

Advanced Parallel Magnetic Resonance Imaging Methods with Applications to MR Spectroscopic Imaging

by

Ricardo Otazo

ABSTRACT OF DISSERTATION

Submitted in Partial Fulfillment of the
Requirements for the Degree of

Doctor of Philosophy
Electrical Engineering

The University of New Mexico

Albuquerque, New Mexico

December, 2007

Advanced Parallel Magnetic Resonance Imaging Methods with Applications to MR Spectroscopic Imaging

by

Ricardo Otazo

B.Sc., Electrical Engineering, Universidad Católica, Paraguay, 2001

M.Sc., Electrical Engineering, University of New Mexico, USA, 2006

Ph.D., Electrical Engineering, University of New Mexico, 2007

Abstract

Parallel magnetic resonance imaging offers a framework for acceleration of conventional MRI encoding using an array of receiver coils with spatially-varying sensitivities. Novel encoding and reconstruction techniques for parallel MRI are investigated in this dissertation. The main goal is to improve the actual reconstruction methods and to develop new approaches for massively parallel MRI systems that take advantage of the higher information content provided by the large number of small receivers. A generalized forward model and inverse reconstruction with regularization for parallel MRI with arbitrary k-space sub-sampling is developed. Regularization methods using the singular value decomposition of the encoding matrix and pre-conditioning of the forward model are proposed to desensitize the solution from data noise and model errors. Variable density k-space sub-sampling is presented to improve the reconstruction with the common uniform sub-sampling. A novel

method for massively parallel MRI systems named Superresolution Sensitivity Encoding (SURE-SENSE) is proposed where acceleration is performed by acquiring the low spatial resolution representation of the object being imaged and the stronger sensitivity variation from small receiver coils is used to perform intra-pixel reconstruction. SURE-SENSE compares favorably the performance of standard SENSE reconstruction for low spatial resolution imaging such as spectroscopic imaging.

The methods developed in this dissertation are applied to Proton Echo Planar Spectroscopic Imaging (PEPSI) for metabolic imaging in human brain with high spatial and spectral resolution in clinically feasible acquisition times.

The contributions presented in this dissertation are expected to provide methods that substantially enhance the utility of parallel MRI for clinical research and to offer a framework for fast MRSI of human brain with high spatial and spectral resolution.

Acronyms

DFT Discrete Fourier Transform

EPI Echo Planar Imaging

FOV Field Of View

GRAPPA Generalized Auto Calibrating Partially Parallel Acquisition

MRI Magnetic Resonance Imaging

MSE Mean Square Error

PEPSI Proton Echo Planar Spectroscopic Imaging

SENSE Sensitivity Encoding

SMASH Simultaneous Acquisition of Spatial Harmonics

SNR Signal to Noise Ratio

SVD Singular Value Decomposition

Contents

List of Figures	xvi
List of Tables	xxvii
1 Introduction	1
1.1 Overview and Motivation	1
1.2 Goals and Contributions.	5
1.2.1 SVD-Based Regularization of Parallel MRI Reconstruction . .	5
1.2.2 Parallel MRI with Variable k-Space Sub-Sampling	6
1.2.3 Superresolution Parallel MRI Reconstruction	6
1.2.4 Proton Echo Planar Spectroscopic Imaging (PEPSI) at High- Field: SNR and Spectral Resolution Improvements	7
1.2.5 Parallel 3D-PEPSI	7
1.2.6 Superresolution Parallel PEPSI	8
1.3 Organization	9

2	Background	10
2.1	The MR Signal	10
2.2	Generalized Spatial Encoding and Image Reconstruction	13
2.3	Conventional MRI	14
2.3.1	Spatial Encoding Using Magnetic Field Gradients	14
2.3.2	Fourier Reconstruction, Spatial Resolution and SNR	16
2.3.3	Limitations on Conventional MRI Speed	18
2.4	Parallel MRI	18
2.4.1	Spatial Encoding Using RF Coil Sensitivities	18
2.4.2	Conventional MRI Acceleration	20
2.4.3	Parallel MRI Reconstruction	21
2.4.4	Coil Sensitivity Estimation	27
2.5	Parallel Transmission	28
2.5.1	Spatial Encoding Using Spatially-Selective RF Pulses	28
2.6	Magnetic Resonance Spectroscopic Imaging	28
2.6.1	MR Spectroscopy (MRS)	29
2.6.2	MR Spectroscopic Imaging (MRSI)	31
2.6.3	Echo-Planar Spectroscopic Imaging	34
2.7	Summary	35
3	SVD-Based Regularization of Parallel MRI Reconstruction	37

Contents

3.1	SENSE Reconstruction	38
3.2	Tikhonov Regularization	40
3.3	SSVD Regularization	41
3.3.1	Relation to Tikhonov Regularization	43
3.3.2	Tuning the Regularization Parameter	44
3.4	Simulations	44
3.4.1	1D acceleration of the noisy data	45
3.4.2	2D acceleration of the noisy data	46
3.4.3	2D acceleration of the noiseless data with innacurate coil sensitivity maps	47
3.5	Experiments	47
3.6	Discussion	49
3.7	Summary	50
4	Parallel MRI with Variable k-Space Sub-Sampling	51
4.1	Introduction	51
4.2	Parallel MRI Modeling and Reconstruction for Arbitrary k-Space Sub-Sampling	53
4.2.1	Forward Model	53
4.2.2	Inverse Reconstruction	54
4.3	Variable Density k-Space Sampling	57

Contents

4.4	Summary	60
5	Superresolution Parallel MRI Reconstruction	61
5.1	Introduction	62
5.2	Superresolution SENSE (SURE-SENSE)	64
5.2.1	Acquisition Model	66
5.2.2	Image Reconstruction	67
5.2.3	SNR and Spatial Resolution Analysis	68
5.3	Experimental Validation	69
5.3.1	Scanner and Array Coil	69
5.3.2	High Resolution Coil Sensitivity Maps	70
5.3.3	Data Processing and Error Quantification	70
5.3.4	Simulations	71
5.3.5	Experiments	74
5.4	Discussion	77
5.5	Summary	79
6	PEPSI at High-Field: SNR and Spectral Resolution Improvements	80
6.1	Introduction	81
6.2	Methods	82
6.2.1	Measurements	82

Contents

6.2.2	Reconstruction	85
6.2.3	Spectral Fitting	87
6.2.4	Comparisons across field strengths	89
6.3	Results	92
6.4	Discussion	97
6.5	Summary	101
7	Parallel 3D-PEPSI	102
7.1	Introduction	103
7.2	Accelerated PEPSI Encoding	105
7.3	SSVD-SENSE-PEPSI Reconstruction	107
7.3.1	2D-SENSE with SSVD Regularization	108
7.3.2	Coil Sensitivity Estimation	109
7.4	Low Spatial Resolution Effects	110
7.5	Experimental Validation	111
7.5.1	Data Acquisition	111
7.5.2	Spectral Fitting, Metabolite Images and Error Quantification	112
7.6	Results	113
7.6.1	g-Factor	113
7.6.2	Point Spread Function	114
7.6.3	Metabolite Maps and Spectra	116

Contents

7.7	Discussion	120
7.8	Summary	122
8	Superresolution Parallel PEPSI	123
8.1	Introduction	123
8.2	Methods	125
8.2.1	Data Acquisition	125
8.3	SURE-SENSE-PEPSI Reconstruction	125
8.4	Spectral Fitting and Metabolite Images	126
8.5	Results	126
8.6	Discussion	129
8.7	Summary	129
9	Conclusions and Future Work	130
	References	135

List of Figures

1.1	a) 32-channel soccer-ball array. b) 96-channel array with Carbon-240 bucky-ball geometry. c) SNR images and d) SNR profiles of the large-N arrays compared to the commercial 12-channel array coil. . .	4
2.1	a) Nuclear precession about the \mathbf{B}_0 axis. b) Net magnetization vector \mathbf{M} , aligned with the external field \mathbf{B}_0 . c) Tipping \mathbf{M} away from the \mathbf{B}_0 axis produces a transverse magnetization that precesses at $\omega_0 = \gamma B_0$	11
2.2	Pulse sequence diagram and k-space trajectory for a) Cartesian or Fourier MRI [1], b) echo-planar MRI [2] and c) spiral MRI [3]. The gradient G_z selects a slice along the z -dimension while G_y and G_x traverse a trajectory in the $k_y - k_x$ plane for 2D imaging. The Cartesian MRI approach only encodes one line per excitation, then the procedure needs to be performed N_y times and the acquisition time T_{ACQ} is given by $T_{ACQ} = N_y T_R$, where T_R is the interval between two consecutive RF excitations. Echo-planar and spiral MRI can traverse a complete 2D trajectory within a single excitation ($T_{ACQ} = T_R$). For 3D imaging, the process is repeated for each slice.	16

List of Figures

2.3 a) Circular array coil with 8 elements. b) Gradient encoding function for $k_x = 5/W_x$ and $k_y = 5/W_y$: pure plane waves in the image space and impulse function in k-space. c) Hybrid encoding functions for different elements in the array. The plane waves are weighted by the coil sensitivities in the image space resulting in a k-space distribution around the point (k_x, k_y) . The shape of the distribution is given by the spatial Fourier transform of the corresponding coil sensitivity. 19

2.4 SENSE reconstruction example. Multi-coil data was simulated multiplying a Shepp-Logan phantom with a) the coil sensitivity maps for the array shown in Fig. 2.3 and adding Gaussian noise. b) DFT reconstruction for different simulated uniform accelerations. The last acceleration was performed along the two spatial dimensions. c) SENSE reconstruction. d) g-factor maps. Note the g-factor and thus noise reduction when using 2D-acceleration for $R = 4$ 24

2.5 Schematic description of k-space reconstruction with $R_y = 2$. a) AUTO-SMASH: A single line from all coils is fit to a single ACS line in a composite k-space. b) GRAPPA: multiple lines from all coils are fit to one line in one coil (here coil 4). The procedure is repeated for every coil, resulting in single coil images. 26

2.6 ^1H -MRS water-suppressed time-domain signal and spectrum of human brain at 3 Tesla. Singlet resonances such as N-Acetyl Aspartate (NAA), Creatine (Cr) and Choline (Cho) as well as J-coupled metabolites such as Glutamate (Glu) and Inositol (Ins) are shown in the spectrum. 30

List of Figures

2.7	Gradient waveforms within a single excitation and corresponding k -space trajectories for a) Conventional CSI and b) Echo-planar CSI (PEPSI). Note that PEPSI traverses a complete $k_x - t$ trajectory while conventional CSI only a line along t which represents an acceleration factor of N_x	33
2.8	Trapezoidal readout gradient and resulting $x-t$ trajectory for a spectral width of 1250 Hz and a FOV along the x-dimension of 20 cm. The circles represents the Cartesian sampling grid resulting from re-gridding (black for positive echoes and gray for negative echoes). . .	34
3.1	a) Coil sensitivity maps for 4 coils from the 8-channel circular array coil. b) g-factor corresponding to uniform 2D acceleration factor of $R = 2 \times 2$	39
3.2	Effect of SSVD regularization on the set of singular values for: a) well-conditioned matrix and b) ill-conditioned matrix.	42
3.3	Reconstruction of the noisy data with 1D acceleration ($R = 4$) using standard SENSE and SENSE-SSVD for different c_0 values.	45
3.4	Reconstruction of the noisy data with 2D acceleration ($R = 2 \times 2$) using standard SENSE and SENSE-SSVD for different c_0 values. . .	46
3.5	Reconstruction of the noiseless data with 2D acceleration ($R = 2 \times 2$) and bias error in the coil sensitivity profiles ($\Delta \mathbf{E} = 0.05 \mathbf{E}$).	47
3.6	Reconstruction of the human brain data with high 2D acceleration ($R = 4 \times 4$) using standard SENSE and SENSE-SSVD ($c_0 = 35$). The error images are taken with respect to the fully-encoded reconstruction (DFT-SWC).	48

List of Figures

4.1	a) Effect of k-space sub-sampling with $R_y = 3$. Note that each point in the sub-encoded image (y-acc) is a combination of more than 3 points from the fully-encoded image (y-full). b) Standard SENSE reconstruction presents artifacts due to the modeling errors described in part a). c) SENSE reconstruction with the general model removes the artifacts.	55
4.2	a) k-space representation of the coil sensitivity maps. b) Piece-wise linear variable density sub-sampling (VS) and uniform sub-sampling (US) schemes for $R = 4$. The slope of the linear function varies according to the k-space density of the coil sensitivity maps. c) SENSE reconstruction with uniform sub-sampling (US) and SSVD regularization reduces noise at the expense of residual aliasing. Residual aliasing in the SSVD regularization is removed by the variable density k-space sub-sampling approach.	59
4.3	a) Map of the variable sub-sampling distance given by the 2D k-space density of the coil sensitivities. b) SENSE reconstruction with uniform sub-sampling. c) SENSE reconstruction with the variable sub-sampling given in a).	60
5.1	Superresolution parallel MRI idea. k-space representation, image and point spread function (PSF) for: a) high and b) low spatial resolution acquisitions. The high resolution data can be estimated from different low resolution acquisitions where the coil sensitivities are varying within the image voxel. Large-N arrays will provide improved performance due to stronger variation of the coil sensitivity maps and thus larger k-space coverage.	65

List of Figures

- 5.2 Coil sensitivity simulation using the Biot-Savart law [4] for coils with different diameters $d= 5$ and 10 cm respectively. a) Spatial domain and b) k-space representation. Note that the stronger decay in the spatial domain increases the k-space extent of the coil sensitivity. 66

- 5.3 Effect of reduced k-space sampling with $R=2$ in the spatial domain for a) standard SENSE and b) superresolution SENSE. For standard SENSE, R equidistant points from the fully encoded data are combined in each point of the data with reduced encoding. For superresolution SENSE, all the points in the fully encoded data are combined in each point of the reduced data with weights given by the PSF of the low spatial resolution acquisition. 67

- 5.4 Simulated phantom reconstruction using the 32-channel array. a) Conventional DFT with sensitivity-weighting (DFT-SW) reconstruction of the fully-encoded data (encoding matrix size: 128×128 , $R=1$). DFT-SW with zero-filling (DFT-SW-ZF) and SURE-SENSE reconstruction of the data with reduced encoding: b) encoding matrix size: 64×64 , $R=4$, c) encoding matrix size: 32×32 , $R = 16$ 72

- 5.5 Point spread function (PSF) reconstruction of the simulated phantom data with reduced encoding (encoding matrix size: 32×32 , reconstruction matrix size: 128×128) using DFT-SW-ZF and SURE-SENSE: a) full-width at half-maximum (FWHM) images, b) PSF in a voxel close to the periphery (r_1), and c) PSF of a central voxel (r_2). 73

List of Figures

5.6	Comparison of standard SENSE and SURE-SENSE reconstruction at low spatial resolution using the 32-channel array. The reconstruction of the fully encoded data is shown for comparison purposes. a) Absolute images. b) Point spread function along the x dimension. The PSF of conventional DFT reconstruction of the accelerated data are shown in gray lines: aliasing peaks for SENSE sub-sampling and broadening with increased side lobes for SURE-SENSE truncated sampling.	75
5.7	Human brain MRI reconstruction for a) 32-channel array and b) 96-channel array.	76
6.1	PEPSI pulse sequence with water suppression (WS), outer volume suppression (OVS), spin echo excitation and echo-planar readout. Data are collected in blocks during each of the cyclically inverted readout gradients (G_r).	83
6.2	Single coil reconstruction flow chart for PEPSI data. Odd and even echoes are separately processed and added to the end after phasing and frequency shift corrections. The water reference scan (NWS) is used for phase correction and frequency referencing.	85
6.3	Regions of interest to compute the averaged spectrum. a) R_1 : 3×3 rectangular ROI in the center of the FOV for the CP coil. b) R_2 : ring-shaped ROI centered within the FOV for the PA coil. r is the Euclidean distance from the center. 9 voxels are chosen from R_2 to match the noise power in R_1 . The positions of the outer volume saturation bands are shown as rectangles.	87

List of Figures

6.4	Simulated macromolecular spectra (left) and parameterization of the simulation (right) by fitting metabolite-nulled spectra with a combination of Lorentzian lines for: a) 1.5 Tesla, b) 3 Tesla, c) 4 Tesla and d) 7 Tesla.	88
6.5	Water-suppressed PEPSI spectra using the CP coil for a) 1.5 T, b) 3 T, c) 4 T, d) 7T (voxel size: 1 cc, and total acquisition time: 8.5 min). The spectral water image, spectral array from the region R_1 , corresponding averaged-spectrum $\bar{S}(\nu)$, fitted averaged-spectrum $\bar{S}_{fit}(\nu)$ and fitting residual $R(\nu)$ are shown for each magnetic field strength.	92
6.6	Comparison of PEPSI and PRESS-CSI spectra at 1.5 and 4 Tesla (CP coil, same subject at each B_0 , total acquisition time: 8.5 min). a) Averaged spectrum. b) SNR-peak for NAA, Cr and Cho as a function of B_0 for four measurements (two measurements at each B_0). c) Line width for NAA, Cr and Cho as a function of B_0	93
6.7	SNR-peak (peak-amplitude to noise) and SNR-area (concentration to noise) as a function of B_0 for NAA, Cho and Cr in measurements using the CP coil. a) SNR-peak with and without a matched-filter (MF) that is adjusted to the measured signal decay as a function of B_0 b) SNR-peak with relaxation correction. c) SNR-area for the reconstructed data without the matched-filter. SNR-peak with relaxation correction and SNR-area increase linearly with B_0	95

List of Figures

6.8 a) SNR-peak as a function of B_0 and position with respect to the center of the FOV (d: radius of the region R_2) for NAA, Cho and Cr in measurements using the 8-channel PA coil. SNR increases from the center towards the periphery of the brain (d=5 cm). The decay at the periphery (d=6 cm) is due to the OVS bands. b) SNR-peak dependence with B_0 for positions close to the center of the FOV (d = 1 cm) and at the edges (d = 5 cm). 96

6.9 Linewidth of NAA, Cr and Cho as a function of B_0 . Decomposition of the linewidth: T_2 -component and component due to line broadening (LB). a) The complete LW in Hz and the T_2 -component increase with B_0 . b) The component due to line broadening increases almost linearly with B_0 ($\alpha_2 \ll \alpha_1$). Since $\alpha_2 \approx 0$, the diffusion contribution to line broadening is negligible. c) The same line width decreases slightly with B_0 when it is measured in ppm. 98

6.10 Noise variance for different gradient waveforms and sampling schemes (dots) (r: ramp time, s: ADC ramp sampling delay, T: total gradient duration). a) Ideal rectangular gradient. b) Trapezoidal gradient with ramp sampling. c) Trapezoidal gradient without ramp sampling. In all cases T= 400 μ s to achieve the same spectral width, which corresponds to the parameters used in this work to encode a 32x32 spatial matrix. The noise variance for each case is normalized to the noise variance of the ideal rectangular gradient. 100

List of Figures

7.1 a) 3D-PEPSI pulse sequence with water suppression (WS), outer volume suppression (OVS), spin-echo RF excitation, phase encodes on G_y and G_z for y and z encoding and trapezoidal G_x gradient for simultaneous encoding of x and f . b) The resulting k-space trajectory is composed by parallel planes of zig-zag k_x - t trajectories. Δk_y and Δk_z determine the Cartesian sampling grid for k_y and k_z . The black lines represents the trajectory after sub-sampling k_y and k_z by a factor R_y and R_z respectively. 106

7.2 SENSE-PEPSI reconstruction diagram. Accelerated positive and negative echoes are reconstructed separately using 2D-SENSE reconstruction for each x - t point. Coil-by-coil PEPSI reconstruction is then performed where positive and negative echoes are combined after spectral phase correction. The final spectroscopic image $S(\mathbf{r}, f)$ data is obtained by sensitivity-weighted combination of the coil-by-coil reconstruction. 107

7.3 Average g-factor for simulated 1D and 2D accelerations using the estimated sensitivity maps. For SENSE-SSVD reconstruction, a threshold $c_0 = 25$ on the condition number of the encoding matrix was employed. 113

7.4 a) g-factor maps for slices 2-7 and b) reconstruction of the 1-st time-domain point of the NWS data from slice 5 for different accelerations. The threshold on CN was set using the reconstruction with $R = 4 \times 2$ ($c_0 = 25$). RMSE is the average RMS error with respect to the fully-encoded data ($R = 1 \times 1$). 114

List of Figures

7.5 PSF along y (a) and z (b) for different accelerations. The source point was located at the border of the brain, where there is a discontinuity of the reference signal to estimate the coil sensitivities. The top row shows the aliased PSF for SoS reconstruction of the accelerated data and the bottom row the unaliased PSF for SENSE reconstruction. Note that the reconstruction using SSVD presented better aliasing suppression. 115

7.6 Metabolite concentration maps of a) NAA, b) Creatine and c) Choline. 117

7.7 a) Glutamate concentration maps at different accelerations for slices 4-7. b) Raw absorption mode spectrum (black line) and corresponding LCMoel fit (red line) for a gray matter (GM) voxel and a white matter (WM) voxel (voxel locations are indicated in part a). The remaining baseline is given by the smooth black curve. The concentration of Glutamate is given in each case. 118

7.8 a) Lipid image from slice 5 for $R = 1 \times 1$ and $R = 4 \times 2$ using standard SENSE (STD) and SSVD reconstruction. b) Absorption mode spectrum from the voxel indicated in part a. Note the reduction in lipid contamination due to residual aliasing in areas with high g-factor seen in Fig. 7.4.b when using SSVD reconstruction as compared to standard SENSE reconstruction. 119

8.1 a) High spatial resolution MRSI: spectrum from a voxel inside the brain and at the periphery where lipids are located. b) Low spatial resolution MRSI: lipid contamination from conventional Fourier reconstruction due to Gibbs ringing. 124

List of Figures

8.2 Human brain MRSI reconstruction. Conventional DFT with sensitivity-weighting (DFT-SW) reconstruction of the fully-encoded data (spatial-encoding matrix size: 64×64), DFT-SW with zero-filling (DFT-SW-ZF) and superresolution SENSE (SURE-SENSE) reconstruction of the data with reduced spatial encoding (spatial-encoding matrix size: 32×32 , $R = 2 \times 2$) for a) water, b) lipids, c) N-Acetyl-Aspartate (NAA) and d) Creatine. 127

8.3 Raw absorption mode spectrum (thin black line) and corresponding LCModel fit (bold black line) for a central voxel. The remaining baseline is given by the smooth curve. More than 3-fold reduction in lipid contamination is obtained with SURE-SENSE in comparison to conventional Fourier reconstruction of the low resolution data. . . 128

List of Tables

6.1	Measurement parameters for PEPSI acquisitions. B_0 : magnetic field strength, SW: spectral width, T_E : echo time, FOV: field of view, Δz : slice thickness, T_A : acquisition time, V_r : voxel volume.	84
6.2	Literature values of T1 and T2 for NAA, Cr and Cho at different magnetic field strengths.	91
6.3	SNR-peak (with T_1 - T_2 relaxation correction and matched-filtering) and LW comparison for NAA, Cr and Cho of PEPSI and PRESS-CSI at 1.5 and 4 Tesla for four different subjects in experiments with the CP coil.	94
7.1	Average absolute concentrations and standard deviations.	116

Chapter 1

Introduction

This chapter presents an overview and motivation of the research developed and expose the goals and novel contributions of this dissertation.

1.1 Overview and Motivation

Magnetic Resonance Imaging (MRI) techniques can produce images of the structure, metabolism and function of the human or any biological system in a non-invasive way [4, 5]. The technique had a significant impact on clinical diagnosis due to the high quality obtained in anatomical images with different contrast mechanisms. As a result, MRI has become the preferred method for many diagnostic studies of the head, spine and joints [6]. However; imaging modalities with higher information content, such as metabolic and functional imaging, impose temporal and physical constraints that represent a challenge for conventional MRI due to low encoding speed. This factor is particularly dominant in experiments with three spatial dimensions (3D) and for imaging of moving structures such as the heart. Conventional MRI uses magnetic field gradients to produce a signal that represents the spatial frequency-domain (k -

Chapter 1. Introduction

space) of the object being imaged with a spatial resolution many times finer than the signal wavelength [7, 1]. However, gradient-encoding limits k-space sampling to one position at a time making k-space speed the crucial component for encoding time. Gradient performance improvement along with echo-planar encoding techniques [2] have reduced significantly the encoding time; but safety guidelines regarding magnetic field gradient switching and RF power deposition constraint further increases in k-space speed.

MR spectroscopic imaging (MRSI) [8, 9] provides spatial localization of metabolism by adding the spectral dimension to MRI. MRSI can identify biomarkers relevant to psychiatric and neurologic disease and there is growing interest in exploring its use in clinical research applications for the entire human body. The major limitation of MRSI is the long encoding time which is mainly due to the sequential encoding mechanism of conventional methods. As a consequence, MRSI is usually restricted to low spatial resolution and single slice acquisition in clinical practice. The development of fast MRSI methods that enable whole brain coverage with high spatial resolution remains a major challenge in MRSI research.

Functional MRI (fMRI) provides spatial localization of functional activation using the blood oxygenation as contrast agent [10, 11]. Using echo-planar imaging (EPI) with the current gradient performance, 1-2 sec of temporal resolution and 3-5 mm of spatial resolution can be achieved simultaneously for whole brain fMRI. Finer spatiotemporal resolutions are restricted due to the technical and physiological constraints mentioned earlier.

Parallel MRI [12, 13, 14, 15, 16, 17] has been proposed to accelerate gradient-encoding by using an array of receiver coils with spatially-varying sensitivities. The knowledge of coil sensitivities allows for reconstruction using a subset of the encoding functions required for conventional Fourier reconstruction, thus some of the Fourier encoding steps can be omitted in the acquisition to accelerate the process. The most

common approach for acceleration is uniform sub-sampling of k-space, where the density of k-space sampling is reduced by an integer factor of the Nyquist rate. The reconstruction for this case is well developed, e.g. SENSE [16] in the spatial-domain; SMASH[15] and GRAPPA [17] in k-space). Non-uniform sub-sampling schemes have demonstrated improved reconstruction for the same acceleration factor [18, 19]. However; optimal selection of k-space samples for parallel MRI still remains an open question.

High acceleration factors in parallel MRI are still challenging due to the SNR loss with respect to acceleration and the presence of residual aliasing artifacts. Recently, the design of large-N arrays, i.e. arrays with a large number of small elements, demonstrated higher acceleration capability due to the increased number of independent projections [20, 21] and higher sensitivity even at appreciable distance from the coils [22]. The use of large-N arrays also introduced new reconstruction algorithms such as inverse imaging [23] that can reduce the application of gradient encoding to a minimum by using an analogy to the reconstruction of magnetoencephalography (MEG) data, where all the spatial information is derived from the array geometry. Advanced reconstruction methods that make use of the higher information content provided by the large array coil still need to be investigated.

For human brain imaging, helmet-shaped arrays with a close-fitting design have demonstrated to be very efficient for parallel MRI providing a high increase in the baseline SNR and large acceleration capability along all the spatial dimensions [24]. For example, the 32-channel receiver array with soccer ball geometry [25] (Fig. 1.1) offers nearly three-fold higher peripheral SNR and 40-50% higher SNR in the center of the head than the commercial 12-channel circular array. The 96-channel array with a similar geometry (Carbon-240 bucky-ball) [26] presents nearly seven-fold SNR gain at the periphery and close 100% SNR gain in the center of the head when compared to the commercial 12-channel circular array. Both array coils were employed in this

Chapter 1. Introduction

dissertation for phantom and *in vivo* experiments. The idea behind using this type of array is to tradeoff the high increase in SNR for shorter acquisition times and/or higher spatial resolution.

Two areas of active research are also motivating the use of parallel MRI with high acceleration. First, the use of high magnetic field strength has been demonstrated to improve the performance of parallel imaging by increasing the baseline SNR and providing stronger modulations of the coil sensitivity profiles [27]. Second, very short encoding times are advantageous for applications using hyperpolarized contrast agents [28], allowing highly accelerated acquisition of large data volumes during the short duration of enhanced polarization.

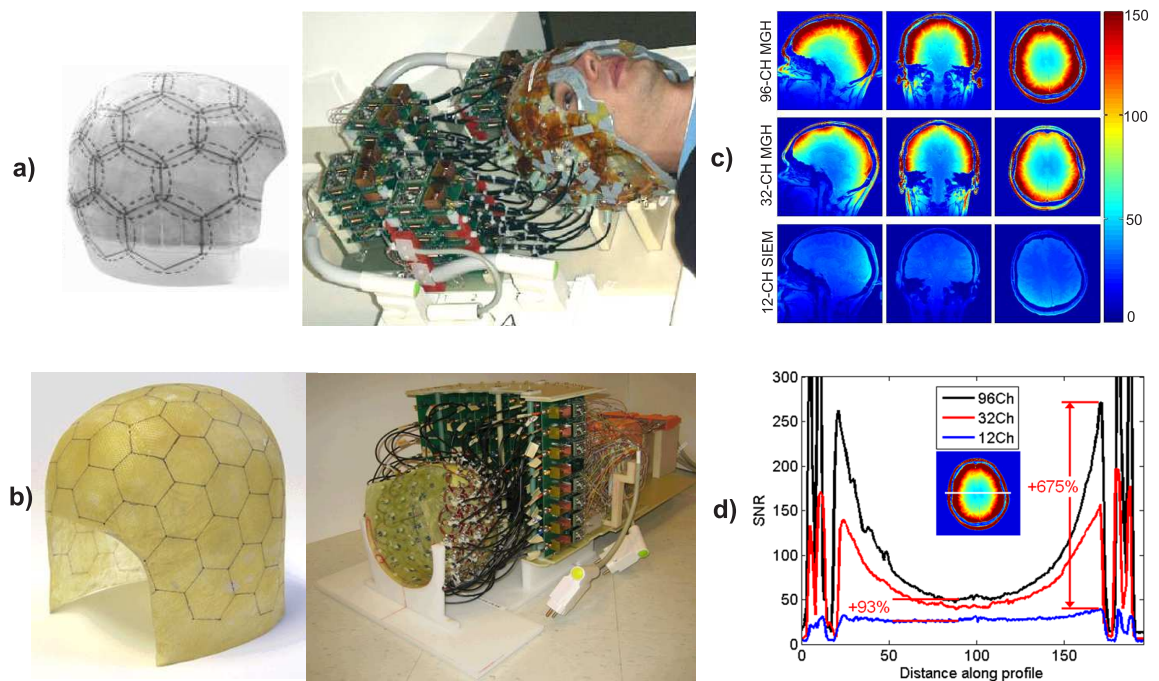


Figure 1.1: a) 32-channel soccer-ball array. b) 96-channel array with Carbon-240 bucky-ball geometry. c) SNR images and d) SNR profiles of the large-N arrays compared to the commercial 12-channel array coil.

1.2 Goals and Contributions.

This dissertation introduces novel encoding and reconstruction methods for parallel MRI in order to enhance the spatial and temporal resolution of current MRI techniques. The main goal is to improve the actual reconstruction methods for parallel MRI and to develop new approaches for massively parallel MRI systems that take advantage of the higher information content provided by the large number of small receivers. The specific contributions are presented below. The first three contributions are related to advanced parallel MRI reconstruction methods that have general application to any MRI modality. The last three contributions present applications for MR spectroscopic imaging. The contributions presented in this dissertation are expected to substantially enhance the utility of parallel MRI for clinical research and to offer a framework for fast MRSI of human brain.

1.2.1 SVD-Based Regularization of Parallel MRI Reconstruction

Parallel MRI reconstruction involves the inversion of the encoding matrix which is commonly computed using the Moore-Penrose pseudoinverse. Large amplification of noise and systematic errors in coil sensitivity estimation may occur when the encoding matrix becomes ill-conditioned. Regions with low-value and overlapped coil sensitivities produce an ill-conditioned encoding matrix since the information provided by each coil is similar. Regularization methods were proposed to desensitize the solution of the inverse problem to data noise and model errors. A novel method for regularization of the matrix inverse problem based on the SVD representation of the encoding matrix is presented for SENSE reconstruction as an efficient alternative to the commonly used Tikhonov regularization. The method is proven to improve SNR and reduce the effect of systematic errors in coil sensitivity estimation at the expense of loss in ideal reconstruction accuracy.

1.2.2 Parallel MRI with Variable k-Space Sub-Sampling

Uniform sub-sampling of k-space is not optimal for parallel MRI if the coil sensitivities overlap, which is the case in practice. Variable sub-sampling has been proposed to improve the reconstruction. For example, in the SPACE-RIP method [18] data is sampled at the Nyquist rate at the center of k-space and more sparsely as we move away from the center. This variable density sampling scheme is based on the property that most of the information content is concentrated within a small region at low k-space values whereas the edge information is distributed over a much broader region of higher k-space values. In this dissertation, k-space sampling positions are chosen according to the k-space representation of the coil sensitivities in order to achieve better reconstruction than uniform sub-sampling. Practical variable sub-sampling schemes and a general framework for parallel MRI with arbitrary k-space sub-sampling are described.

1.2.3 Superresolution Parallel MRI Reconstruction

Parallel MRI has been introduced as a method to accelerate the encoding process by sub-sampling k-space while maintaining the total extent. The rationale for this sub-encoding scheme is that the coil sensitivity maps are very smooth and retrieve k-space information only from the neighborhood of the actual gradient-encoding point. New array coil designs with a large number of small elements provide stronger variation of the coil sensitivities which may result in residual aliasing artifacts in conventional parallel MRI method due to sensitivity variation within the image pixel. In this dissertation, a novel parallel MRI method known as superresolution sensitivity encoding (SURE-SENSE) is proposed as an alternative to standard SENSE using coils with strongly varying coil sensitivities. Acceleration is performed by acquiring the low spatial resolution representation of the object being imaged and the coil sensitiv-

ity maps are acquired with higher target spatial resolution. The increase in spatial resolution will be determined by the degree of coil sensitivity variation within the low resolution voxel and the SNR in the low resolution object image. The technique is particularly applicable to intrinsically low spatial resolution modalities such as spectroscopic imaging where conventional parallel MRI methods are vulnerable to artifacts.

1.2.4 Proton Echo Planar Spectroscopic Imaging (PEPSI) at High-Field: SNR and Spectral Resolution Improvements

Proton Echo Planar Spectroscopic Imaging (PEPSI) [29] is a fast spatial-spectral encoding technique that uses a trapezoidal readout gradient for simultaneous encoding of one spatial dimension and the spectral dimension. Theoretical expectations for MRS show a linear increase in SNR and spectral resolution with respect to the magnetic field strength (B_0). However, no experimental validation has been performed for echo-planar MRSI. SNR per unit volume and unit time and line width of the three main metabolites N-Acetyl-Aspartate (NAA), Creatine (Cr) and Choline (Cho) were estimated from *in vivo* PEPSI acquisitions at 1.5, 3, 4 and 7 Tesla on scanners sharing a similar software and hardware platform, using single-channel and 8-channel head receiver coils. Data were corrected for ramp sampling and relaxation differences, processed with a time-domain matched filter and fitted to a parametric model adapted to each B_0 . The noise characteristics of the PEPSI encoding technique were evaluated and compared to the conventional phase-encoded MRSI.

1.2.5 Parallel 3D-PEPSI

3D-PEPSI is still very time consuming due to phase-encoding (sequential) along the third spatial dimension. In this dissertation, parallel imaging techniques are proposed

to accelerate the phase-encoding dimensions of PEPSI. Specifically, the combination of PEPSI with SENSE [16] is presented. The goal is to show 2D-MRSI and 3D-MRSI of human brain in clinically feasible acquisition times: less than 1 minute for 2D-PEPSI and within 1-2 minutes for 3D-PEPSI. SENSE reconstruction is applied to each spectral point to reconstruct the accelerated spatial dimensions, where the aliasing due to k-space sub-sampling is removed. Even though SENSE reconstruction involves only spatial dimensions, the spectral dimension can suffer from strong lipid contamination due to residual spatial aliasing in SENSE reconstruction. The following approaches are presented to optimize the implementation:

- 32-channel soccer-ball array coil: to increase the acceleration capability.
- Optimization of coil sensitivity estimation: smoothing of the raw sensitivity maps with extrapolation beyond the border of the brain using a 3-rd order polynomial model.
- SVD-based regularization of SENSE-PEPSI reconstruction: to reduce amplification of noise and coil sensitivity estimation errors in regions with low-value and overlapped coil sensitivities.

1.2.6 Superresolution Parallel PEPSI

MRSI is intrinsically constrained by low SNR, due to the relative low metabolite concentration. As a consequence, k-space coverage in acquisition is sacrificed to achieve an adequate SNR within a feasible acquisition time. The lack of high k-space information leads to blurred metabolite maps and strong lipid contamination due to Gibbs ringing when the Fourier transform is directly applied to reconstruct the image. The strong lipid signal arises from subcutaneous lipids in the scalp and the resulting resonance cover a large spectral region and overlap with the metabolite resonances. In this dissertation, the superresolution parallel MRI approach presented

in Chapter 5 is applied to PEPSI in order to to reduce lipid contamination and to enhance the spatial resolution of the metabolite maps.

1.3 Organization

The present chapter presented an overview and motivation of the research work; and exposed the goals and novel contributions of this doctoral dissertation. Chapter 2 presents background information about MRI and parallel MRI exposing the limits of actual techniques. The next three chapters present novel parallel imaging reconstruction methods. In Chapter 3, SVD-based solution and regularization for SENSE reconstruction is presented. Parallel MRI with variable sub-sampling of k-space is presented in Chapter 4. Chapter 5 presents the method of superresolution parallel MRI reconstruction. The next three chapters present applications for MRSI. SNR and spectral resolution improvements in PEPSI at high magnetic field are presented in Chapter 6. Parallel 3D-PEPSI using the 32-channel soccer-ball array is presented in Chapter 7 for fast volumetric metabolite mapping in human brain. Chapter 8 presents superresolution parallel PEPSI for high resolution 2D-MRSI of human brain. Chapter 9 concludes the dissertation and discusses future work.

Chapter 2

Background

This chapter is not intended to provide a comprehensive exposition of the physical and engineering principles of MRI and MRSI, which are well documented in many textbooks [4, 5]. Principles regarding to spatial encoding and image reconstruction techniques for conventional and parallel MRI are reviewed in order to provide a platform of discussion for the dissertation. Spatial-spectral encoding and reconstruction methods for spectroscopic imaging are also presented. Image reconstruction is formulated as a generalized linear inverse problem. Selected examples of parallel MRI reconstruction methods and the application of parallel MRI to spectroscopic imaging are discussed.

2.1 The MR Signal

The MR signal originates from the nuclear magnetic resonance (NMR) phenomenon discovered independently by Edward Purcell and Felix Bloch in 1945 [30, 31]. In atoms with an odd number of protons and/or odd number of neutrons, such as ^1H (hydrogen) and ^{31}P (phosphorus), the atomic magnetic moments (spins) do not add

Chapter 2. Background

up to zero, resulting in a net nuclear spin. When such atoms are exposed to an external magnetic field \mathbf{B}_0 each spin will experience a precession about the direction of the field (Fig. 2.1) with an angular frequency ω_0 given by:

$$\omega_0 = \gamma B_0, \quad (2.1)$$

where B_0 is the magnitude of \mathbf{B}_0 and γ is a physical constant known as the gyromagnetic ratio. For example, $\frac{\gamma}{2\pi} = 42.58 \text{ MHz/T}$ for ^1H . Note that the precession frequency can be forced to be spatially varying by using a spatially varying magnetic field $B(\mathbf{r})$. The main effect of the external magnetic field \mathbf{B}_0 is the creation of a macroscopic magnetization \mathbf{M} in the direction of the field (Fig. 2.1).

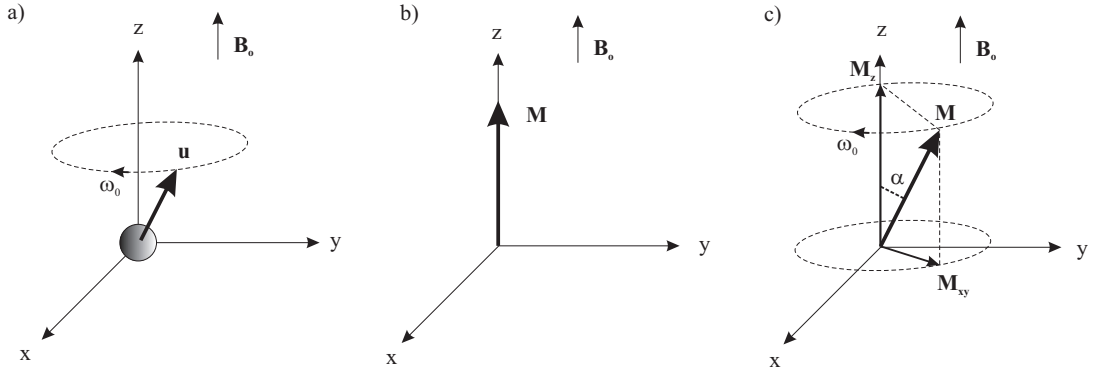


Figure 2.1: a) Nuclear precession about the \mathbf{B}_0 axis. b) Net magnetization vector \mathbf{M} , aligned with the external field \mathbf{B}_0 . c) Tipping \mathbf{M} away from the \mathbf{B}_0 axis produces a transverse magnetization that precesses at $\omega_0 = \gamma B_0$.

The magnetization vector can be rotated from the z axis by applying a radio frequency (RF) pulse that produces a magnetic field \mathbf{B}_1 in the transverse plane (x - y), resulting in a time varying magnetization $M_{xy}(t)$ (Fig. 2.1). The flip angle $\alpha(\mathbf{r})$ for the position \mathbf{r} can be expressed as:

$$\alpha(\mathbf{r}) = \int_0^{T_p} \gamma B_1(\mathbf{r}, t) dt. \quad (2.2)$$

where T_p is the duration of the RF pulse.

Chapter 2. Background

After the spins have been rotated into the x - y plane, they gradually return to equilibrium, which is in the z axis. This process, referred to as relaxation, has an exponential behavior characterized with two time constants, T_1 and T_2 . T_1 is associated with the exponential recovery of the longitudinal component of the magnetization $M_z(t)$ and T_2 with the exponential decay of the transverse component $M_{xy}(t)$. The relaxation process governs the magnetization behavior after the RF pulse is switched off. The behavior of the spins is described by a single equation, referred to as the Bloch equation:

$$\frac{d\mathbf{M}}{dt} = \mathbf{M} \times \gamma \mathbf{B} - \frac{M_x \hat{\mathbf{i}} + M_y \hat{\mathbf{j}}}{T_2} - \frac{(M_z - M_0) \hat{\mathbf{k}}}{T_1}, \quad (2.3)$$

where $\mathbf{M} = (M_x(t), M_y(t), M_z(t))$, and $\hat{\mathbf{i}}$, $\hat{\mathbf{j}}$, and $\hat{\mathbf{k}}$ are unit vectors along the x , y , and z dimensions respectively. For a RF pulse with $\alpha = 90^\circ$, the solution is given by:

$$M_z(t) = M_0(1 - e^{-t/T_1}), \quad (2.4)$$

$$M_{xy}(t) = M_0 e^{-t/T_2} e^{-j\omega_0 t}. \quad (2.5)$$

The oscillating magnetization vector produces a varying magnetic flux in the receiving coil and the voltage induced can be expressed in terms of a volume integral of M_{xy} :

$$v(t) \propto \int_{\mathbf{r}} c(\mathbf{r}) M_{xy}(\mathbf{r}) e^{j\omega(\mathbf{r})t} d\mathbf{r}, \quad (2.6)$$

where $c(\mathbf{r})$ is the RF coil reception sensitivity.

The voltage $v(t)$ is subsequently demodulated by $\cos(\omega_0 t)$ and $\sin(\omega_0 t)$ and observing that $M_{xy}(\mathbf{r}) = M_0(\mathbf{r}) \sin(\alpha(\mathbf{r}))$, the following MR signal is obtained:

$$y(t) = \int_{\mathbf{r}} c(\mathbf{r}) M_0(\mathbf{r}) \sin(\alpha(\mathbf{r})) e^{j(\omega(\mathbf{r}) - \omega_0)t} d\mathbf{r}. \quad (2.7)$$

2.2 Generalized Spatial Encoding and Image Reconstruction

MRI methods encode identifiable spatial information into the MR signal, and the image is reconstructed by properly decoding the spatially encoded MR signal. From Eq. (2.7), there are four spatially dependent functions: magnetization ($M_0(\mathbf{r})$), receiver pattern ($c(\mathbf{r})$), excitation pattern ($\alpha(\mathbf{r})$) and magnetic field (B). The magnetization is the goal of image reconstruction and thus unknown, but the other three functions can be used for spatial encoding representing mechanisms at different stages: at the beginning, the RF pulse provides an excitation pattern $\alpha(\mathbf{r})$; then the magnetic field $B(\mathbf{r})$ dictates the spin phase evolution; and at the end, the detected MR signal is weighted by the coil sensitivity $c(\mathbf{r})$.

In the general case where all the functions are employed, the spatial encoding kernel $\epsilon_i(\mathbf{r})$ may be defined as follows:

$$\epsilon_i(\mathbf{r}) = c(\mathbf{r}) \sin(\alpha(\mathbf{r})) e^{j\omega(\mathbf{r})t_i}. \quad (2.8)$$

Defining an image function $s(\mathbf{r})$ that accounts for the magnetization, relaxation and the constants terms, the observation $y_i = y(t = t_i)$ can be interpreted as a projection of $s(\mathbf{r})$ onto $\epsilon_i(\mathbf{r})$:

$$y_i = \langle \epsilon_i(\mathbf{r}), s(\mathbf{r}) \rangle, \quad (2.9)$$

where $\langle \cdot \rangle$ is the inner product operator. In theory, it would require an infinite number of projections to reconstruct $s(\mathbf{r})$, since it is a continuous function. In practice, appropriate discretization of the continuous position vector \mathbf{r} to n points provides the following encoding equation in matrix formulation:

$$\mathbf{y} = \mathbf{E}\mathbf{s}, \quad (2.10)$$

where \mathbf{y} is the observation vector ($m \times 1$), \mathbf{E} is the encoding matrix ($m \times n$) whose entries are given by the corresponding discretized basis functions $\epsilon_{i,k}$ and \mathbf{s} is the set

of pixels to be reconstructed ($n \times 1$). Using this model, image reconstruction in MRI is formulated as a generalized linear inverse problem. The reconstruction is given by the inverse of the encoding matrix:

$$\hat{\mathbf{s}} = \mathbf{E}^{-1}\mathbf{y}. \quad (2.11)$$

Note that \mathbf{s} can be uniquely reconstructed from n linearly independent projections ($m = n$). If $m \neq n$, a generalized inverse needs to be defined in order to solve the system.

The remaining sections will use this linear algebra framework to characterize the spatial encoding and reconstruction methods of conventional and parallel MRI.

2.3 Conventional MRI

2.3.1 Spatial Encoding Using Magnetic Field Gradients

Conventional MRI relies on the spatially varying magnetic field $B(\mathbf{r})$ for spatial encoding. Principles of spatial encoding using magnetic field gradients, originally called *zeugmatography*, were introduced by Paul Lauterbur in 1972 [7]. A spatially uniform RF excitation is employed to rotate the magnetization at a constant flip angle α . The coil sensitivity is combined with the object function to form the coil-weighted object function $s(\mathbf{r})$. The resulting MR signal equation is simplified to:

$$y(t) = \int_{\mathbf{r}} s(\mathbf{r}) e^{j\gamma(B(\mathbf{r}) - B_0)t} d\mathbf{r}, \quad (2.12)$$

where the constant term $\sin(\alpha)$ corresponding to the excitation pattern is now included in the object function. The gradient vector is given by:

$$\mathbf{G}(t) = G_x(t)\hat{\mathbf{i}} + G_y(t)\hat{\mathbf{j}} + G_z(t)\hat{\mathbf{k}}. \quad (2.13)$$

Chapter 2. Background

Each gradient causes a linear variation of the magnetic field along the gradient direction. The magnitude of the magnetic field is now represented by:

$$B(\mathbf{r}, t) = B_0 + \mathbf{G}(t) \cdot \mathbf{r} = B_0 + G_x(t)x + G_y(t)y + G_z(t)z. \quad (2.14)$$

The phase evolution over time can be expressed in terms of $\mathbf{k} \cdot \mathbf{r}$, where the vector \mathbf{k} is defined as the gradient moment vector:

$$\mathbf{k}(\mathbf{t}) = \frac{\gamma}{2\pi} \int_0^t \mathbf{G}(\tau) d\tau. \quad (2.15)$$

The MR signal equation is then expressed as:

$$y(t) = \int_{\mathbf{r}} s(\mathbf{r}) e^{j\mathbf{k}(\mathbf{t}) \cdot \mathbf{r}} d\mathbf{r}. \quad (2.16)$$

Note that \mathbf{k} defines a spatial-frequency space, commonly known as k-space, and that the acquired signal is the spatial Fourier transform of the object function. The spatial encoding functions are given by:

$$\epsilon_i(\mathbf{r}) = e^{j\mathbf{k}(\mathbf{t}_i) \cdot \mathbf{r}}, \quad (2.17)$$

which corresponds to the Fourier basis functions.

The MRI dataset is acquired by traversing k-space using a specific trajectory and the image is reconstructed by applying an inverse Fourier transformation. In this case, the reconstruction is accomplished without the need of computing the inverse of the encoding matrix \mathbf{E} explicitly. The most common acquisition trajectory is the Cartesian grid (Fig. 2.2), where the image can be reconstructed by a direct inverse Fast Fourier Transform (FFT) [1]. However, the encoding process for the Cartesian grid is slow requiring repetitions for each line in k-space. Faster encoding may be accomplished using time-varying gradients, e.g. echo-planar and spiral MRI methods (Fig. 2.2), where a complete 2D set of k-space points can be acquired within a single excitation (single-shot techniques). However, the reconstruction process becomes more complicated since the k-space trajectory does not fall into a Cartesian

grid and the acquired dataset needs to be regridded in order to use the FFT for reconstruction [32]. Another possibility is to use a non-uniform FFT approach for direct reconstruction of the non-Cartesian data [33].

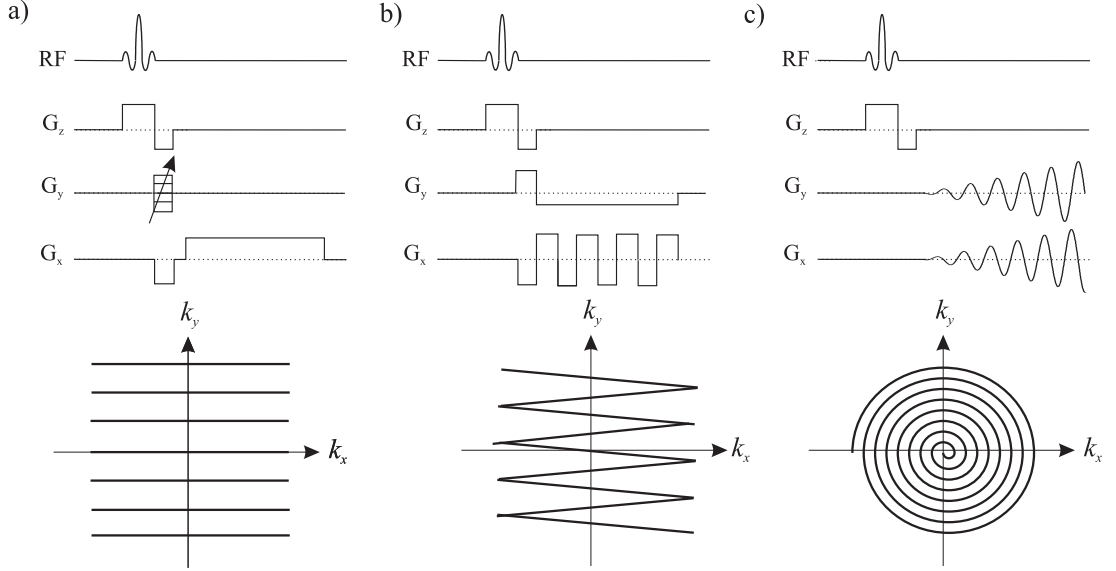


Figure 2.2: Pulse sequence diagram and k-space trajectory for a) Cartesian or Fourier MRI [1], b) echo-planar MRI [2] and c) spiral MRI [3]. The gradient G_z selects a slice along the z -dimension while G_y and G_x traverse a trajectory in the $k_y - k_x$ plane for 2D imaging. The Cartesian MRI approach only encodes one line per excitation, then the procedure needs to be performed N_y times and the acquisition time T_{ACQ} is given by $T_{ACQ} = N_y T_R$, where T_R is the interval between two consecutive RF excitations. Echo-planar and spiral MRI can traverse a complete 2D trajectory within a single excitation ($T_{ACQ} = T_R$). For 3D imaging, the process is repeated for each slice.

2.3.2 Fourier Reconstruction, Spatial Resolution and SNR

The problem of reconstructing the object function $s(\mathbf{r})$ from its Fourier transform samples $S(\mathbf{k}_n)$ acquired onto the k-space grid D can be expressed using the following formulation:

$$\text{Given } S(\mathbf{k}_n) = \int_{\mathbf{r}} s(\mathbf{r}) e^{j2\pi \mathbf{k}_n \cdot \mathbf{r}} d\mathbf{r}, \mathbf{k}_n \in D; \quad \text{determine } s(\mathbf{r}). \quad (2.18)$$

Chapter 2. Background

In theory, the object function can be recovered unambiguously for infinite k-space sampling using the Discrete Fourier Transform (DFT). In practice, reconstruction from finite k-space data is represented as the convolution of the true object function $s(\mathbf{r})$ and the point spread function (PSF) $h(\mathbf{r})$:

$$\hat{s}(\mathbf{r}) = s(\mathbf{r}) * h(\mathbf{r}). \quad (2.19)$$

For the case of the DFT, the PSF is given by a sinc function. The spatial resolution is limited to the effective width of the PSF, e.g. the width of the main lobe, which corresponds to the maximum value of k-space. The spatial resolution for the spatial dimension r is given by:

$$\Delta r = \frac{1}{k_{max}} = \frac{1}{N_r \Delta k}, \quad (2.20)$$

where N_r is the number of points acquired along the dimension r and Δk is the k-space sampling interval determined by the sampling theorem. The Nyquist sampling interval for the spatial dimension r is given by $\Delta k = 1/W_r$, where W_r is the Field of View (FOV) along r . Any attempt to decrease Δr by sampling at a slower rate will lead to aliasing. In addition to limited resolution, the convolution with the PSF results in Gibbs ringing due to the oscillatory nature of the PSF. One way to reduce ringing is to use a window in k-space before applying the DFT reconstruction at the expense of loss in spatial resolution, e.g. the Hamming window attenuates the side lobes by roughly 30 dB but increases the width of the main lobe by a factor of 1.6. One of the goals of this dissertation is to study superresolution reconstruction, this is to estimate high k-space components from limited k-space acquisitions using prior information and therefore achieve both reduction of the main lobe width and attenuation of the side lobes of the PSF.

The signal-to-noise ratio (SNR) in MRI is proportional to the square root of the acquisition time (T_a) and to the voxel volume (V_r) which determines the spatial resolution:

$$\text{SNR} \propto \sqrt{T_a} V_r. \quad (2.21)$$

This fundamental equation establishes the limits for spatial and temporal resolution as a SNR constrain. A reduction of acquisition time with the same voxel volume or viceversa, results in SNR loss. Conventional MRI methods require a trade-off between spatial resolution and acquisition time according to the available SNR.

2.3.3 Limitations on Conventional MRI Speed

The imaging speed of conventional MRI is basically limited by the sequential data acquisition scheme where k-space data is acquired one point at a time making k-space speed the crucial component for encoding time. To accelerate data acquisition for the same k-space coverage, conventional MRI requires stronger field gradients, faster gradient switching rates and more frequently applied RF pulses (higher RF power deposition). Unfortunately, these techniques increase the risk of damaging the underlying biological tissues which constrains further increases in k-space speed.

2.4 Parallel MRI

2.4.1 Spatial Encoding Using RF Coil Sensitivities

Parallel MRI [34, 35, 36] uses an array of receiver RF coils with spatially-varying sensitivities to acquire multiple signals of distinct spatial information content simultaneously. Each receiver coil provides different spatial information due of its different spatial reception profile. The signal acquired by each coil can be expressed as:

$$Y_l(\mathbf{k}) = \int_{\mathbf{r}} s(\mathbf{r})c_l(\mathbf{r})e^{j2\pi\mathbf{k}\cdot\mathbf{r}} d\mathbf{r}, \quad l = 1, 2, \dots, N_c; \quad (2.22)$$

where $c_l(\mathbf{r})$ is the complex-valued spatially-varying sensitivity for the l -th coil and N_c is the number of receiver coils. Note that the encoding functions are given by the

Chapter 2. Background

gradient (Fourier) encoding functions weighted by the coil sensitivities:

$$\epsilon_{l,n}(\mathbf{r}) = c_l(\mathbf{r})e^{j\mathbf{k}_n \cdot \mathbf{r}}. \quad (2.23)$$

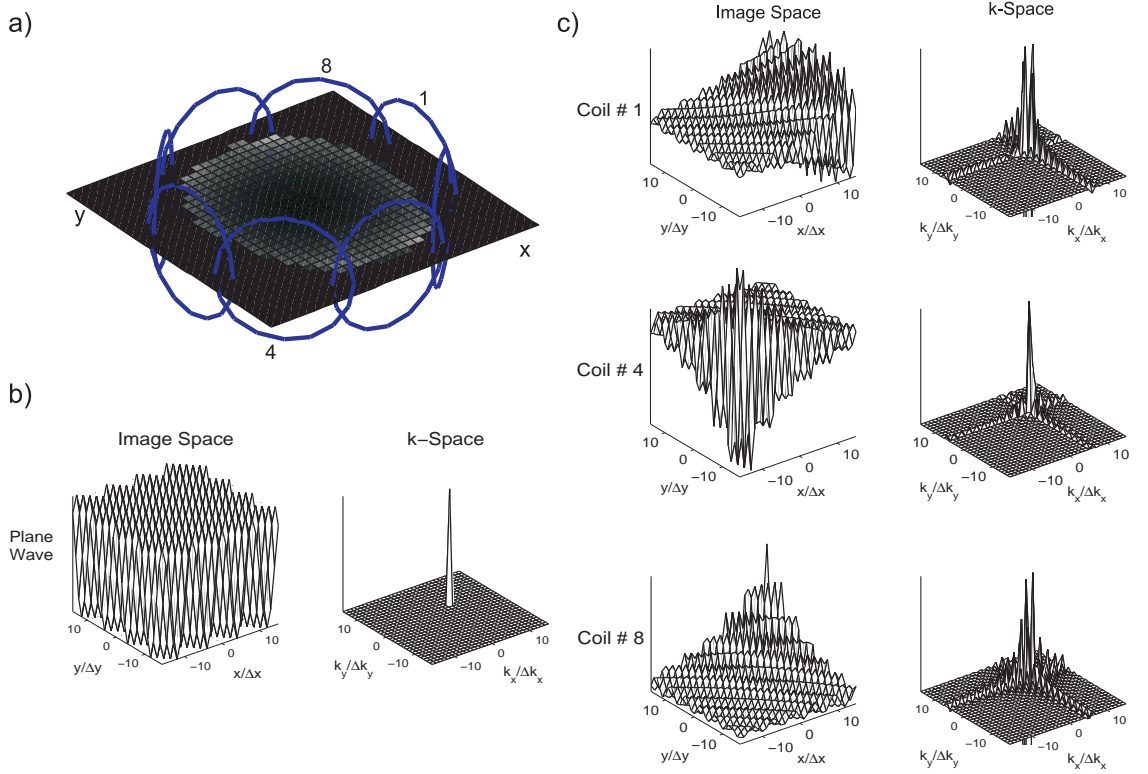


Figure 2.3: a) Circular array coil with 8 elements. b) Gradient encoding function for $k_x = 5/W_x$ and $k_y = 5/W_y$: pure plane waves in the image space and impulse function in k-space. c) Hybrid encoding functions for different elements in the array. The plane waves are weighted by the coil sensitivities in the image space resulting in a k-space distribution around the point (k_x, k_y) . The shape of the distribution is given by the spatial Fourier transform of the corresponding coil sensitivity.

The gradient encoding functions correspond to pure spatial plane waves with a k-space representation given by an impulse function at the \mathbf{k}_n value specified by the gradients (Fig. 2.3). Therefore only one position in k-space can be sampled at a time. However, the hybrid encoding functions correspond to weighted spatial plane

waves with a k-space representation given by the spatial Fourier transform of the coil sensitivity centered at \mathbf{k}_n . Therefore a distribution in k-space with a different shape and extent is sampled at a time for each coil (Fig. 2.3). In other words, the use of multiple receiver coils with different spatial sensitivities allows for performing different conventional gradient encoding steps at a time.

2.4.2 Conventional MRI Acceleration

Simultaneous encoding by different coil sensitivities can be used to complement gradient encoding and thus to reduce the number of gradient encoding functions necessary to reconstruct the image. Acceleration is performed by k-space sub-sampling, this is using a k-space sampling rate below the Nyquist rate. The working hypothesis is that the hybrid encoding functions contain k-space information from the neighborhood of the point defined by the gradients that will cover the non sampled region (Fig. 2.3). In the framework of the generalized linear inverse problem, the number of equations is increased by a factor of N_c (number of coils) while the number of unknowns remains the same. The matrix system is overdetermined and the redundancy is exploited to allow acceleration of the conventional encoding process.

The most common approach for acceleration is to reduce the density of k-space sampling by an integer factor while the extent is maintained to achieve the same spatial resolution (uniform sub-sampling). However; uniform sub-sampling of k-space is optimal only for the theoretical case of coils with non-overlapped sensitivities. One of the goals of this dissertation is to study sub-sampling schemes that take into account the k-space extent of the coil sensitivities and the partial overlap between coil sensitivities (Chapter 4).

2.4.3 Parallel MRI Reconstruction

Since the encoding functions in parallel MRI no longer form a Fourier basis, reconstruction cannot be achieved by just applying a Fourier transform. Instead, the encoding matrix \mathbf{E} and its inverse need to be computed explicitly. The signal acquired by each receiver coil can be expressed as:

$$Y_l(\mathbf{k}) = \int_{\mathbf{r}} s(\mathbf{r}) \epsilon_{l,n}(\mathbf{r}) d\mathbf{r}, \quad l = 1, 2, \dots, N_c; \quad (2.24)$$

where $\epsilon_{l,n}(\mathbf{r})$ corresponds to the hybrid encoding function given in Eq. (2.23). After discretization of the object function to N_r points and considering the acquisition of N_k k-space points, the system can be expressed using the generalized linear inverse model $\mathbf{y} = \mathbf{E} \mathbf{s}$ given by Eq. (2.9), \mathbf{y} is the observation vector ($N_c N_k \times 1$), \mathbf{E} is the encoding matrix ($N_c N_k \times N_r$) and \mathbf{s} is the set of points to be reconstructed ($N_r \times 1$). In general, the solution of this system can be formulated as a minimization of the mean square error (MSE):

$$\arg \min_{\mathbf{s}} \|\mathbf{y} - \mathbf{E} \mathbf{s}\|_2^2, \quad (2.25)$$

where $\|\cdot\|_2$ is the L_2 -norm. If the system is overdetermined, this is $N_c N_k \geq N_r$, the solution is given by the Moore-Penrose pseudoinverse of \mathbf{E} [16]:

$$\hat{\mathbf{s}} = (\mathbf{E}^H \mathbf{\Phi}^{-1} \mathbf{E})^{-1} \mathbf{E}^H \mathbf{\Phi}^{-1} \mathbf{y}, \quad (2.26)$$

where $\mathbf{\Phi}$ is the noise covariance matrix, which can be computed using an average sample estimate from data acquired in the absence of MR signal, e.g. without RF excitation:

$$\hat{\mathbf{\Phi}} = \frac{1}{N_n} \sum_{i=1}^{N_n} \mathbf{n}_i \mathbf{n}_i^H, \quad (2.27)$$

where $\mathbf{n} = [n_1, n_2, \dots, n_{N_c}]$ is the array noise vector and N_n is the number of points acquired. Note that this reconstruction is general and can be performed in the image space or k-space, but it might be numerically unstable and computationally intensive. Practical methods for parallel MRI reconstruction exploit simplifications based on the sampling pattern or perform iterative reconstruction.

Image Space Reconstruction

Image space reconstruction methods first produce aliased images from the sub-sampled k-space data for each coil by direct DFT reconstruction and then remove the aliasing using coil sensitivity information. This type of reconstruction is referred to as Sensitivity Encoding (SENSE) [16]. In its simplest form, SENSE is applicable to uniformly sub-sampled Cartesian data, where the extent of k-space is kept the same, maintaining the image resolution, but the distance between adjacent k-space lines is increased by a factor R . Therefore, the signals from R locations, equally spaced along the sub-sampled dimension (r), overlap in the image. Provided that the coil sensitivity is not the same at those different locations, the weight given by each coil to the signal components will be different. The aliased image for the l -th coil is given by:

$$y_l(r) = \sum_{m=0}^{R-1} s(r - m\hat{W}_r)c_l(r - m\hat{W}_r), \quad (2.28)$$

where $\hat{W}_r = W_r/R$ is the reduced FOV. This equation can be formulated in the same format of Eq. (2.9) for each point in the aliased image using:

$$\mathbf{y} = \begin{bmatrix} y_1(r) \\ y_2(r) \\ \vdots \\ y_{N_c}(r) \end{bmatrix}, \quad \mathbf{s} = \begin{bmatrix} s(r) \\ s(r - \hat{W}) \\ \vdots \\ s(r - (R-1)\hat{W}) \end{bmatrix},$$

$$\text{and } \mathbf{E} = \begin{bmatrix} c_1(r) & c_1(r - \hat{W}) & \dots & c_1(r - (R-1)\hat{W}) \\ c_2(r) & c_2(r - \hat{W}) & \dots & c_2(r - (R-1)\hat{W}) \\ \vdots & \vdots & \ddots & \vdots \\ c_{N_c}(r) & c_{N_c}(r - \hat{W}) & \dots & c_{N_c}(r - (R-1)\hat{W}) \end{bmatrix}.$$

Note that uniform sub-sampling allows to break down the general reconstruction into a series of small equations solved separately for each set of aliased points. The

Chapter 2. Background

solution comes from the inversion of small matrices. For a reduction factor of R , it would be necessary to invert $N_r/R N_c \times R$ -sized matrices.

In the general case of arbitrary sub-sampling, every spatial point can potentially alias with all the others and the whole encoding matrix needs to be inverted. Given the very large size of this matrix, the memory requirements and the time needed to solve this problem would be impractical. Iterative methods such as the Conjugate Gradient can be used to solve the normal equations of parallel MRI reconstruction:

$$(\mathbf{E}^H \Phi^{-1} \mathbf{E})\mathbf{s} = \mathbf{E}^H \Phi^{-1} \mathbf{y}, \quad (2.29)$$

provided that the matrix \mathbf{E} is positive definite. In Chapter 4, a general reconstruction for parallel MRI with arbitrary sub-sampling is presented.

Reducing the number of encoding points leads in itself to a reduction in SNR of \sqrt{R} due to reduced DFT averaging. Also the SNR at each point in the reconstructed image will depend on how easily the matrix inversion can be performed, i.e. on how different the coil sensitivities are at the aliased pixels. The geometry factor or g-factor, which is dependent on the particular geometry of the array coil, describes the error amplification due to numerical instabilities and has become a standard method to describe the performance of a parallel MRI method. In general, noise and errors due to inaccurate coil sensitivity estimation will be amplified. For SENSE-like reconstruction algorithms, the g-factor at position r is given by [16]:

$$g(r) = \sqrt{\left[(\mathbf{E}^H \Phi^{-1} \mathbf{E})^{-1} \right]_r \left[\mathbf{E}^H \Phi^{-1} \mathbf{E} \right]_r} \geq 1. \quad (2.30)$$

The spatially varying SNR in parallel MRI reconstruction can be expressed as:

$$\text{SNR}_{acc}(r) = \frac{\text{SNR}_{full}(r)}{g(r)\sqrt{R}}, \quad (2.31)$$

where $\text{SNR}_{full}(r)$ is the SNR for full encoding. One of the goals of this dissertation is to investigate methods to reduce the g-factor to improve image reconstruction quality at high acceleration factors by performing regularization of the inverse problem.

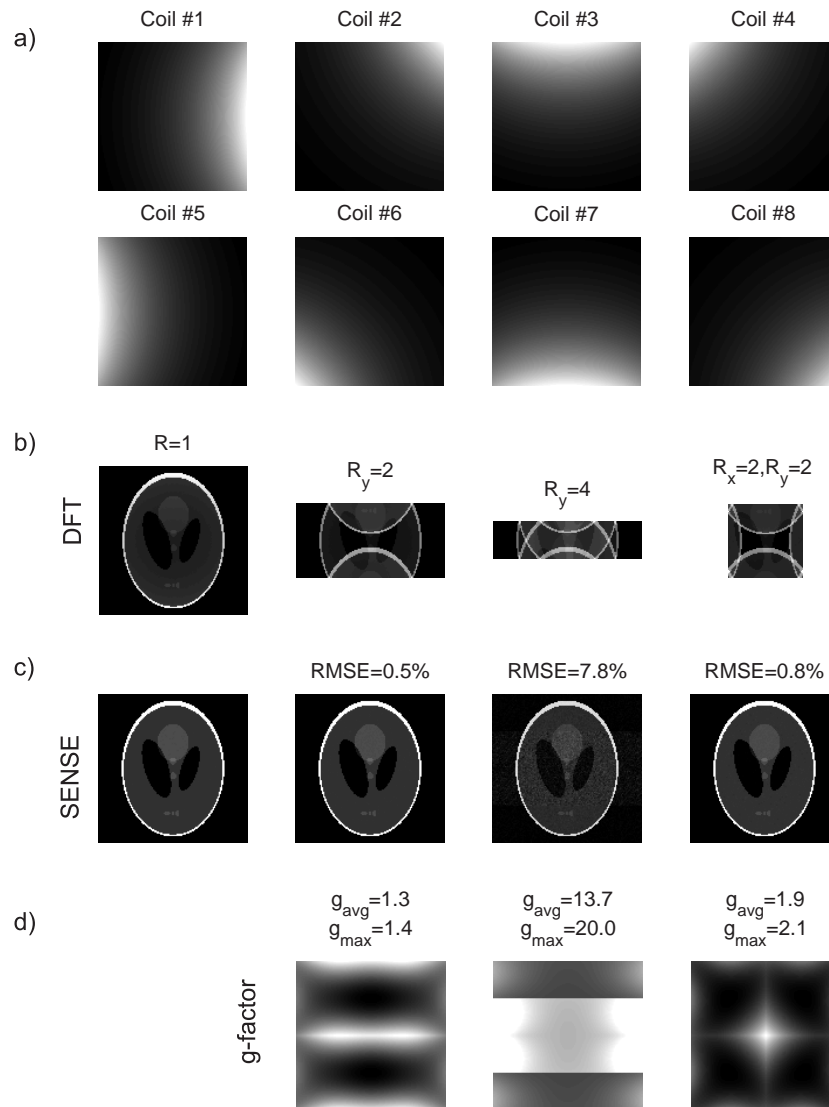


Figure 2.4: SENSE reconstruction example. Multi-coil data was simulated multiplying a Shepp-Logan phantom with a) the coil sensitivity maps for the array shown in Fig. 2.3 and adding Gaussian noise. b) DFT reconstruction for different simulated uniform accelerations. The last acceleration was performed along the two spatial dimensions. c) SENSE reconstruction. d) g-factor maps. Note the g-factor and thus noise reduction when using 2D-acceleration for $R = 4$.

k-Space Reconstruction

k-space reconstruction techniques computes directly in k-space the missing data due to sub-sampling using the multiple information proportioned by the array coil. DFT reconstruction is then applied to get the final image. Note that in k-space the object function is convolved with the coil sensitivities.

The basic concept of SMASH (Simultaneous Acquisition of Spatial Harmonics)[15] is that a linear combination of the sub-sampled k-space data provided by the array coil can directly generate the missing k-space information. The weights are given by the coil sensitivities. The SMASH estimate of the missing k-space information is given by:

$$\hat{S}(\mathbf{k} - m\Delta\mathbf{k}) = \sum_{l=1}^{N_c} w_l^{(m)} Y_l(\mathbf{k}), \quad (2.32)$$

where $Y_l(\mathbf{k})$ is the sub-sampled k-space data acquired by the l -th coil and the weights $w_l^{(m)}$ are calculated to fit the m -th harmonic:

$$\sum_{l=1}^{N_c} w_l^{(m)} c_l(\mathbf{r}) = e^{jm\Delta\mathbf{k}\cdot\mathbf{r}}. \quad (2.33)$$

However, SMASH is strongly restricted to coil configurations that are able to generate the desired spatial harmonics. In contrast to the use of specific coil sensitivities, AUTO-SMASH [37] introduced the concept of autocalibration, where a small number of additionally acquired Auto Calibration Signal (ACS) points are used to represent the coil sensitivities. The weights are computed fitting a point in the reduced data set to the ACS point, which is given by:

$$\sum_{l=1}^{N_c} w_l^{(m)} Y_l(\mathbf{k}) = \sum_{l=1}^{N_c} Y_l^{ACS}(\mathbf{k} - m\Delta\mathbf{k}), \quad (2.34)$$

where $Y_l^{ACS}(\mathbf{k} - m\Delta\mathbf{k})$ is the ACS point for the l -th coil corresponding to an offset $m\Delta\mathbf{k}$. The weights are used to get a estimate of the missing point in the same way as the SMASH technique (Eq. (2.32)).

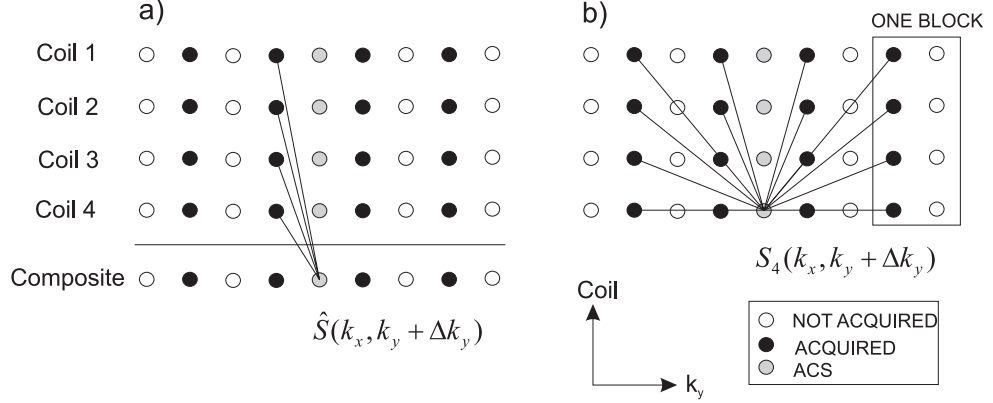


Figure 2.5: Schematic description of k-space reconstruction with $R_y = 2$. a) AUTO-SMASH: A single line from all coils is fit to a single ACS line in a composite k-space. b) GRAPPA: multiple lines from all coils are fit to one line in one coil (here coil 4). The procedure is repeated for every coil, resulting in single coil images.

GRAPPA (Generalized Auto Calibrating Partially Parallel Acquisition)[17] represents a more generalized implementation of the SMASH-type methods, where coil-by-coil reconstruction is performed by applying multiple blockwise reconstructions. The weights are computed fitting a point in the reduced data set to the ACS point of each coil, which is given by:

$$\sum_{l=1}^{N_c} w_l^{(m)} Y_l(\mathbf{k}) = Y_l^{ACS}(\mathbf{k} - m\Delta\mathbf{k}). \quad (2.35)$$

The process of reconstructing data in coil k at the position $(\mathbf{k} - m\Delta\mathbf{k})$ from the sub-sampled data using a blockwise reconstruction is represented by:

$$\hat{S}_k(\mathbf{k} - m\Delta\mathbf{k}) = \sum_{l=1}^{N_c} \sum_{b=1}^{N_b} w(k, b, l, m) Y_l(\mathbf{k} - bR\Delta\mathbf{k}), \quad (2.36)$$

where R is the acceleration factor, N_b is the number of blocks. A block is defined as a single acquired line and $R - 1$ missing lines (Fig. 2.5). By using more blocks of data to fit each point, GRAPPA improves the reconstruction in comparison to the previously described k-space methods.

2.4.4 Coil Sensitivity Estimation

Parallel MRI reconstruction methods require accurate coil sensitivity information to reconstruct properly the image from sub-sampled k-space data. The sensitivities depend not only on the array coil geometry, but are strongly influenced by the sample and therefore experimental estimation of sensitivity information using reference data is necessary. Reference data can be acquired as a separate acquisition (pre-scan) or as an integral part of the acquisition (auto-calibration).

The auto-calibration method does not require to compute explicitly the coil sensitivity maps and has the advantage that the reference data and the target data are locked together in time more closely, so that the reconstruction is less susceptible to temporal changes, e.g. motion. On the other hand, the reconstruction is not perfect since it does not follow exactly the encoding equation.

The pre-scan method require to compute explicitly the complex coil sensitivity maps. The reference signal for the l -th coil can be represented as:

$$y_{ref,l}(\mathbf{r}) = c_l(\mathbf{r})s_{ref}(\mathbf{r}), \quad (2.37)$$

where $c_l(\mathbf{r})$ is the sensitivity function to be estimated, $s_{ref}(\mathbf{r})$ is the object function for the reference acquisition. The object function can be estimated using a method for array coil signal combination, such as Sum of Squares (SoS) reconstruction:

$$\hat{s}_{ref}(\mathbf{r}) = \frac{1}{N_c} \sqrt{\sum_{l=1}^{N_c} |y_{ref,l}(\mathbf{r})|^2}. \quad (2.38)$$

A raw sensitivity map is created by dividing the image from each coil by $\hat{s}_{ref}(\mathbf{r})$:

$$\hat{c}_l(\mathbf{r}) = \frac{s_{ref,l}(\mathbf{r})}{\hat{s}_{ref}(\mathbf{r})}. \quad (2.39)$$

The raw sensitivity maps are impaired by noise. Refinement of the sensitivity maps can be accomplished using smoothing, such as polynomial fitting [16].

2.5 Parallel Transmission

2.5.1 Spatial Encoding Using Spatially-Selective RF Pulses

The remaining spatially-varying term in the MR signal equation is the flip angle $\alpha(\mathbf{r})$, which does not provide by itself an immediate benefit of accelerating image acquisition. Even though this dissertation assumes spatially uniform RF excitations, the potential of using RF pulses to perform additional spatial encoding is presented. Spatially-selective RF pulses are commonly used to provide uniform excitation within a region of the object function. Complex excitation patterns can be achieved by using appropriate combinations of RF and gradient waveforms at the expense of longer duration of RF pulses and/or increase in the RF power deposition which constrained the application of spatially-selective RF pulses. In analogy to the use of multiple receiver coils to reduce the image acquisition time, parallel transmission using multiple transmitter coils can be performed to reduce the duration of the spatially-selective RF pulse and/or reduce the RF power deposition. Katscher *et al.* introduced the method using the SENSE algorithm to synthesize the desired excitation profile with shorter RF pulses [38].

2.6 Magnetic Resonance Spectroscopic Imaging

The goal of magnetic resonance spectroscopy (MRS) is to make quantitative measurements of the concentrations of chemical components by encoding the spectral dimension of the MR signal. In spectroscopic imaging, concentration maps are generated using a combination of spatial encoding techniques from MRI and spectral encoding techniques from MRS (spatial-spectral encoding).

2.6.1 MR Spectroscopy (MRS)

Nuclei do not only experience the external magnetic field, but they are also very sensitive to their chemical environment. This causes a small displacement of the precession frequency during the MR experiment, referred to as chemical shift, due to shielding created by the orbital motion of the surrounding electrons in response to the main field [39, 40]. Therefore, the MR signal contains components with different chemical shifts that can be measured by collecting the time-domain response of the systems to produce a MR spectrum. Chemical shift is not expressed in units of Hertz, since this would make it dependent on the magnetic field strength. Therefore, it is expressed in terms of dimensionless parts per million (*ppm*):

$$\nu = 10^6 \frac{f - f_{\text{r}}}{f_{\text{r}}}, \quad (2.40)$$

where f_{r} is a reference frequency that depends on the nucleus being used. Feasible nuclei for *in vivo* measurements are hydrogen (^1H), phosphorus-31 (^{31}P) and carbon-13 (^{13}C). ^1H is the preferred nucleus for MRS due to its high abundance and therefore high sensitivity. The typical proton spectrum of the human brain is a superposition of signals arising from approximately 20 different low molecular weight metabolites (Fig. 2.6). Metabolites are present as single and multiplet resonances. Multiplets are produced by spin-spin coupling of the metabolites (J-coupling). ^1H -MRS techniques require water suppression, due to the $\sim 10^4$ higher concentration of water in comparison to the metabolites, which is accomplished by a spectral filter that saturates the water resonance during the acquisition [41, 42].

Spectral encoding is performed by collecting the time-domain signal resulting from exciting a selected voxel (volume element). Single voxel excitation is performed by a combination of slice-selective excitations along the three spatial dimensions, where each excitation selects a slice and the intersection of the three slices defines the volume. The time-domain signal represents the impulse response of the voxel

Chapter 2. Background

within a limited spectral width given by $\text{SW} = 1/\Delta t$ where Δt is the temporal sampling interval (dwell time in the MR literature). The signal acquired from a single resonance f_i can be represented as a complex-valued exponentially-decaying sinusoid:

$$s_i(t) = s_{i,0} e^{j2\pi f_i t} e^{-\frac{t}{T_{2,i}}}, \quad (2.41)$$

where $s_{i,0}$ is the signal amplitude at $t = 0$, and $T_{2,i}$ is the effective transverse-relaxation time-constant. The complete spectrum is modeled as a superposition of single resonances.

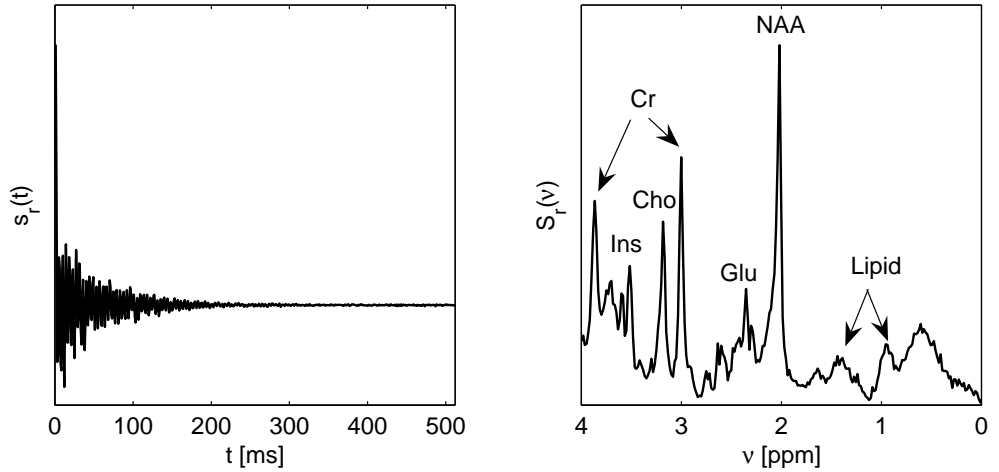


Figure 2.6: ^1H -MRS water-suppressed time-domain signal and spectrum of human brain at 3 Tesla. Singlet resonances such as N-Acetyl Aspartate (NAA), Creatine (Cr) and Choline (Cho) as well as J-coupled metabolites such as Glutamate (Glu) and Inositol (Ins) are shown in the spectrum.

Spectral quantification is performed by fitting the acquired spectrum to a mathematical model, which provides the information required for metabolite concentration estimation. *In vivo* spectra present complicated patterns due to spectral overlapping and distortions due to magnetic field inhomogeneities, e.g. linebroadening. Moreover, broad spectral contributions from sources other than the metabolites of interest,

such as macromolecules and residual water, form a baseline difficult to model [43]. A better spectral fitting can be obtained using a model based on a linear combination of basis spectra (basis sets). The basis spectra can be measured from phantoms with known metabolite concentrations or they can be simulated according with the metabolite physical model and acquisition parameters. The acquired spectra are then fitted by finding the linear combination of the basis sets which best describes the data. LCMModel spectral fitting [44], an implementation of this method, is used in this dissertation for spectral quantification.

2.6.2 MR Spectroscopic Imaging (MRSI)

MRSI encodes the chemical shift and spatial distribution of metabolites simultaneously using a combination of MRI and MRS techniques. Metabolite concentration images are obtained using spectral fitting in each voxel. The signal equation for MRSI using gradient-encoding can be represented as:

$$Y(\mathbf{k}, t) = \int_{\mathbf{r}, f} s(\mathbf{r}, f) e^{j2\pi(\mathbf{k}\cdot\mathbf{r}+ft)} d\mathbf{r}df, \quad (2.42)$$

where $s(\mathbf{r}, f)$ is the spatial-spectral object function. For 3D-MRSI, the signal traverse a path in four dimensions (k_x, k_y, k_z, t) , which is the Fourier space corresponding to (x, y, z, f) .

The conventional method, originally called Chemical Shift Imaging (CSI) [8], applies sequential phase-encoding to the spatial dimensions and then acquires a time-domain signal in the absence of gradients to preserve the spectroscopic information (Fig. 2.7). The procedure is repeated for each point in k-space defined by the gradients. The spectroscopic image is then obtained by direct DFT reconstruction. This sequential method is very time consuming with an acquisition time given by $T_{ACQ} = N_x N_y N_z T_R$, where N_x , N_y and N_z are the number of points acquired along the x , y and z dimensions respectively and T_R is the repetition time.

Chapter 2. Background

The major limitation of MRSI is the long acquisition time which is dictated by the intrinsic low sensitivity of MRS as well as the slow encoding speed of conventional methods. MRSI presents an intrinsically low SNR due to the relative low concentrations of the metabolites which might require signal averaging to achieve an acceptable spectral quality for an accurate quantification. As a consequence, MRSI is usually restricted to low spatial resolution and single slice acquisition in clinical practice, e.g. 2-4 cc. Moreover, low spatial resolution MRSI is susceptible to spectral contamination from regions with strong non-metabolite signals due to the increased ringing in a poorly defined PSF. For example, in ^1H -MRSI of the human brain, strong lipid signals from extracranial fat can contaminate the metabolite spectra within the brain. In this dissertation, methods to increase the available SNR in MRSI such as higher magnetic field strength and array coils with a large number of elements are presented and evaluated quantitatively.

The development of fast MRSI methods that enable whole brain coverage with high spatial-spectral resolution remains a major challenge in MRSI research. Many methods have been developed to provide faster spatial-spectral encoding [45], such as echo-planar techniques that allow for simultaneous spatial-spectral encoding using time-varying gradients [46]. The encoding of spectral information is a relatively slow process due to the small spectral bandwidth. For example the typical sampling period of ^1H -MRS at 3 Tesla is about 1 ms. Spatial information can be encoded much faster, e.g. sampling period in order of microseconds. Therefore it is possible to simultaneously encode spectral and spatial information in an interleaved fashion using a series of inverted readout gradients. Each gradient encodes a 1D spatial projection and the progression of gradients encodes spectral information as shown in Fig. 2.7. Proton-Echo-Planar-Spectroscopic-Imaging (PEPSI) [29] is an implementation of this technique with a trapezoidal readout gradient for simultaneous encoding of one spatial dimension (x) and the spectral dimension (f) providing a net acceleration of N_x over the conventional phase-encoding method with comparable signal-to-noise

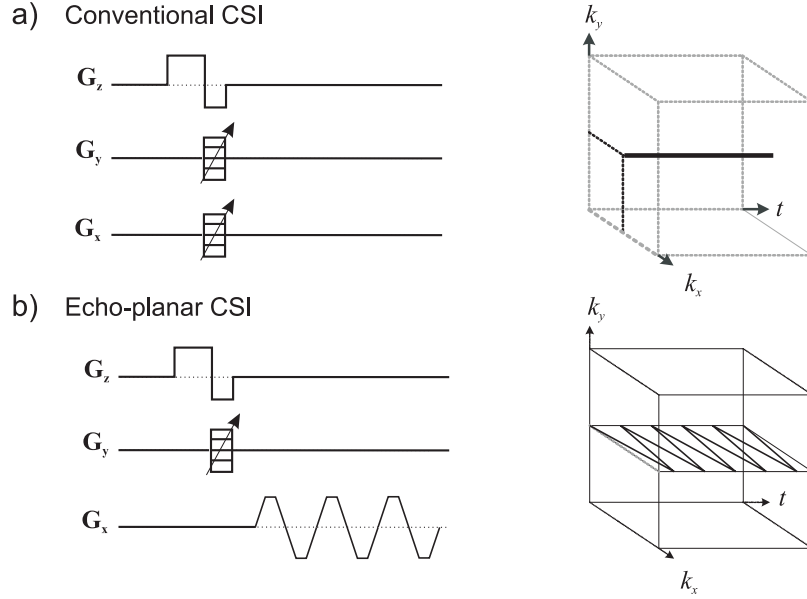


Figure 2.7: Gradient waveforms within a single excitation and corresponding k-space trajectories for a) Conventional CSI and b) Echo-planar CSI (PEPSI). Note that PEPSI traverses a complete $k_x - t$ trajectory while conventional CSI only a line along t which represents an acceleration factor of N_x .

ratio (SNR) per unit time and unit volume. Simultaneous spatial and spectral encoding can be also achieved using spiral trajectories in k-space. Each spiral encodes a 2D image and the progression of spirals encodes spectral information [47].

Accelerated spatial encoding for MRSI can be accomplished using parallel imaging techniques. Even though parallel MRI reconstruction can be applied in the same way as in MRI for each spectral point of the MRSI data, the low resolution characteristics of the MRSI acquisition can produce residual aliasing artifacts if the coil sensitivities vary within the voxel and/or the coil sensitivities present discontinuities. Moreover, MRSI data requires reconstruction of the spectral dimension for coherent combination of the signals from the multiple receiver coils, e.g. spectral-phase correction and frequency alignment. In this dissertation, the reconstruction of accelerated parallel PEPSI data is presented for fast 3D-MRSI of human brain (Chapter 7).

2.6.3 Echo-Planar Spectroscopic Imaging

The main component of the PEPSI technique is the echo-planar readout which allows for simultaneous spatial-spectral encoding (Fig. 2.7). k_x and t are sampled simultaneously during the readout interval on a zig-zag trajectory defined by a periodic trapezoidal gradient (Fig. 2.8):

$$k_x(t) = \gamma \int_0^t G_x(\tau) d\tau, \quad (2.43)$$

where γ is the gyromagnetic ratio and $G_x(t)$ is the magnetic field gradient along the x direction. Simultaneous $k_x - t$ encoding is possible since the sampling period for t is much longer than the sampling period for x and then we can sample a complete line of k_x for each t .

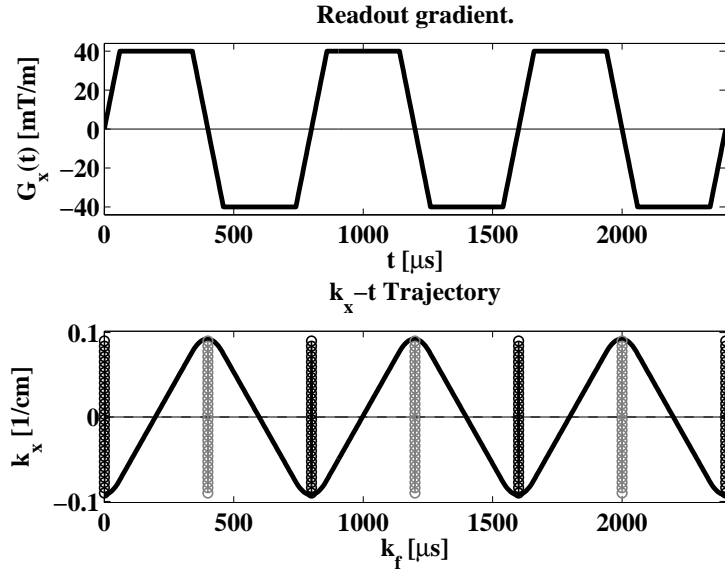


Figure 2.8: Trapezoidal readout gradient and resulting $x-t$ trajectory for a spectral width of 1250 Hz and a FOV along the x -dimension of 20 cm. The circles represents the Cartesian sampling grid resulting from regridding (black for positive echoes and gray for negative echoes).

Data regridding is required to resample the data acquired with the zig-zag trajectory onto a Cartesian grid in order to reconstruct the data using the Fast Fourier Transform (FFT). Convolutional regridding methods [32] present an improved performance when compared to conventional interpolation methods. The non-Cartesian data can be described by:

$$M_s(\mathbf{k}) = M(\mathbf{k}) \cdot S(\mathbf{k}), \quad (2.44)$$

where $M(\mathbf{k})$ is the spatial Fourier transform of the object function and $S(\mathbf{k})$ represents the non-Cartesian sampling trajectory as a set of impulse functions. To resample this data onto a Cartesian grid, $M_s(\mathbf{k})$ is weighted by the density of the sampling trajectory $\rho(\mathbf{k})$, then convolved with a kernel $C(\mathbf{k})$ and finally resampled onto a regularly spaced grid:

$$M_c(\mathbf{k}) = \left[\frac{M_s(\mathbf{k})}{\rho(\mathbf{k})} * C(\mathbf{k}) \right] \cdot \Pi(\mathbf{k}), \quad (2.45)$$

where $\Pi(\mathbf{k})$ is the set of uniformly spaced impulses, i.e. the Cartesian grid. The regridding procedure is applied to data acquired with positive and negative gradients separately (Fig. 2.8). Positive and negative echo data are added after time reversal of the data acquired with negative gradients.

2.7 Summary

Spatial encoding and image reconstruction in MRI can be represented as a generalized linear inverse problem. The forward model is built using the physical model of the acquired MR signal which presents three functions for spatial encoding: excitation pattern, magnetic field (gradients) and reception pattern. Moreover, prior information can be easily incorporated in the forward model to reduce errors in the reconstructed image, e.g. magnetic field inhomogeneity. Parallel MRI can accelerate conventional gradient encoding at the expense of SNR loss due to the reduced

Chapter 2. Background

number of samples and ill-conditioning of the inverse problem. In Chapter 3, regularization of the inverse problem is presented in order to reduce the second effect. Acceleration in parallel MRI is achieved by k-space subsampling which is commonly performed by decreasing the sampling density uniformly. In Chapter 4, methods to optimize the sub-sampling pattern are presented. The major limitation of MRSI is the long acquisition time which constrains the spatial resolution and coverage of the method. Chapter 7 presents the development of parallel PEPSI for fast 3D-MRSI of the human brain and Chapter 7 shows the feasibility of single-shot 2D-MRSI using a modification of parallel PEPSI. Moreover, the intrinsically low SNR of MRSI further limits the spatial resolution. Chapter 5 presents superresolution parallel MRI reconstruction for spatial resolution enhancement of intrinsically low spatial resolution MRI modalities such as MRSI. The method offers an alternative to conventional parallel MRI reconstruction for low spatial resolution modalities.

Chapter 3

SVD-Based Regularization of Parallel MRI Reconstruction

¹ Parallel MRI techniques allow for reconstruction of sub-sampled (accelerated) MRI acquisitions at the expense of SNR loss in the reconstructed image. Part of this SNR loss results from the numerical instabilities in the matrix inversion due to ill-conditioning of the encoding matrix. Moreover, parallel MRI reconstruction is sensitive to errors in coil sensitivity estimation especially when the encoding matrix is ill-conditioned. Regularization methods were proposed to desensitize the solution of the inverse problem to data noise and model errors. A novel method for regularization of the matrix inverse problem based on the SVD representation of the encoding matrix is presented for SENSE reconstruction as an efficient alternative to the commonly used Tikhonov regularization.

¹The work in this chapter was published as part of: R. Otazo, S-Y. Tsai, F-H. Lin and S. Posse. “Accelerated Short-TE 3D Proton-Echo-Planar-Spectroscopic-Imaging using 2D-SENSE with a 32-Channel Array Coil”. *Magn Reson Med*. In Press. Presented at the 15th ISMRM Meeting, Berlin, Germany, 2007, pp. 46.

3.1 SENSE Reconstruction

SENSE reconstruction [16] in its simplest form is applicable to uniformly sub-sampled Cartesian k-space data, where the extent of k-space is kept the same to maintain image resolution, but the distance between adjacent k-space points is increased by a factor R . Therefore, the signals from R locations, equally spaced along the sub-sampled dimension (r), overlap in the aliased image. For each point in the aliased images we have the following encoding equation:

$$\mathbf{y} = \mathbf{E} \mathbf{s}, \quad (3.1)$$

where \mathbf{y} is the vector of aliased points ($N_c \times 1$), \mathbf{E} is the encoding equation ($N_c \times R$) and \mathbf{s} is the vector of points to be reconstructed ($N_c \times 1$). Note that uniform sub-sampling allows to break down the complete system into a series of small systems. For a reduction factor of R , it would be necessary to invert N_r/R $N_c \times R$ -sized matrices, where N_r is the number of points in the reconstructed image.

Correlation between coils can be removed by pre-whitening the acquired data and the estimated coil sensitivity functions [48]. The benefit of this operation is that the noise covariance matrix becomes equal to identity and hence can be omitted later in the reconstruction. Pre-whitening is performed by:

$$\begin{aligned} \mathbf{y} &= \hat{\Phi}^{-\frac{1}{2}} \mathbf{y}_0, \\ \mathbf{E} &= \hat{\Phi}^{-\frac{1}{2}} \mathbf{E}_0, \end{aligned} \quad (3.2)$$

where $\hat{\Phi}$ is the noise covariance matrix estimate. Φ can be estimated using a sample average estimate from a time-series chosen from a position outside the object that contains only noise or from an extra acquisition without RF excitation \mathbf{n}_t ($N_c \times 1$):

$$\hat{\Phi} = \frac{1}{N_t} \sum_{t=1}^{N_t} (\mathbf{n}_t - \bar{\mathbf{n}}) (\mathbf{n}_t - \bar{\mathbf{n}})^H, \quad (3.3)$$

where N_t is the number of time points and $\bar{\mathbf{n}}$ is the mean of \mathbf{n}_t . $\hat{\Phi}^{-\frac{1}{2}}$ can be obtained

using the Singular Value Decomposition (SVD) of $\hat{\Phi}$:

$$\begin{aligned}\hat{\Phi} &= \mathbf{U}_{\hat{\Phi}} \Sigma_{\hat{\Phi}} \mathbf{U}_{\hat{\Phi}}^H, \\ \hat{\Phi}^{-\frac{1}{2}} &= \Sigma_{\hat{\Phi}}^{-\frac{1}{2}} \mathbf{U}_{\hat{\Phi}}^H.\end{aligned}\tag{3.4}$$

From this point onwards, we consider that the observation vector and encoding matrix were pre-whitened thus creating a set of virtual channels that are uncorrelated. The standard SENSE solution $\hat{\mathbf{s}}$ is given by the Moore-Penrose pseudoinverse of the encoding matrix \mathbf{E} :

$$\hat{\mathbf{s}} = \mathbf{E}^\dagger \mathbf{y} = (\mathbf{E}^H \mathbf{E})^{-1} \mathbf{E}^H \mathbf{y}.\tag{3.5}$$

Noise amplification due to ill-conditioning of the encoding matrix is computed by the g-factor [16]:

$$g(r) = \sqrt{\left[(\mathbf{E}^H \mathbf{E})^{-1} \right]_r \left[\mathbf{E}^H \mathbf{E} \right]_r} \geq 1.\tag{3.6}$$

g-factor is particularly high in regions with low-value or overlapped coil sensitivities where the spatial information provided by the different coils is similar and the encoding matrix becomes close to singular, e.g. the central region for a circular array coil (Fig. 3.1).

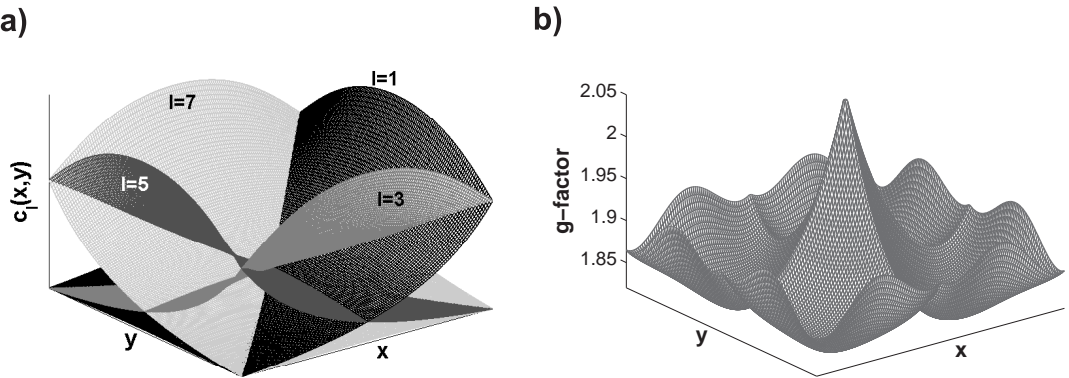


Figure 3.1: a) Coil sensitivity maps for 4 coils from the 8-channel circular array coil. b) g-factor corresponding to uniform 2D acceleration factor of $R = 2 \times 2$.

SENSE reconstruction is also very sensitive to errors in coil sensitivity estimation, especially when \mathbf{E} is ill-conditioned. To desensitize the solution of the inverse problem to data noise and model errors, regularization methods are often used [49]. The idea of using regularization of the inverse problem is to tradeoff matrix conditioning (SNR) with ideal reconstruction accuracy to reduce noise and model error amplification.

3.2 Tikhonov Regularization

Tikhonov regularization [50] is the most common regularization scheme for SENSE reconstruction, in which we form a weighted sum of the data mismatch $\|\mathbf{E}\mathbf{s} - \mathbf{y}\|_2^2$ and a regularization term $\|(\mathbf{s} - \mathbf{s}_0)\|_2^2$ using a weighting factor λ^2 and find the solution that minimizes the sum:

$$\hat{\mathbf{s}}_t = \arg \min_{\mathbf{s}} \|\mathbf{E}\mathbf{s} - \mathbf{y}\|_2^2 + \lambda^2 \|(\mathbf{s} - \mathbf{s}_0)\|_2^2, \quad (3.7)$$

where λ is referred to as the regularization parameter and \mathbf{s}_0 is a regularization image, i.e. prior information about the final solution. A closed-form solution exists for the L_2 -norm and it is given by:

$$\hat{\mathbf{s}}_t = \mathbf{s}_0 + (\mathbf{E}^H \mathbf{E} + \lambda^2 \mathbf{I})^{-1} \mathbf{E}^H (\mathbf{y} - \mathbf{E}\mathbf{s}_0). \quad (3.8)$$

Selecting appropriate values for λ and \mathbf{s}_0 is essential for the regularized reconstruction method. For the regularization image, there are two options: (a) set $\mathbf{s}_0 = 0$ or (b) collect an image that contains prior information about the final solution. The performance of the last scheme is limited by inconsistencies between the reference and the actual image. For the regularization parameter, the simplest form is to use a constant value of λ over the complete image [51]. However, this method is not effective because the condition of \mathbf{E} varies at different regions. A more elaborate way is to select λ adaptively using methods such as the L-curve [48] or modeling λ as a linear function of the condition number of \mathbf{E} [52].

3.3 SSVD Regularization

In this Chapter, a novel regularization technique for SENSE reconstruction based on the Singular Value Decomposition (SVD) of the encoding matrix is proposed. The SVD of \mathbf{E} is given by $\mathbf{U}_{\mathbf{E}}\mathbf{\Sigma}_{\mathbf{E}}\mathbf{V}_{\mathbf{E}}^H$, where $\mathbf{U}_{\mathbf{E}}$ ($N_c \times N_c$) and $\mathbf{V}_{\mathbf{E}}$ ($R \times R$) are unitary matrices containing the singular vectors \mathbf{u}_i and \mathbf{v}_i in their columns. $\mathbf{\Sigma}_{\mathbf{E}}$ is a diagonal matrix ($N_c \times R$) containing the singular values of \mathbf{E} (σ_i 's). The SVD-based pseudoinverse of \mathbf{E} is then given by $\mathbf{E}^\dagger = \mathbf{V}_{\mathbf{E}}\mathbf{\Sigma}_{\mathbf{E}}^{-1}\mathbf{U}_{\mathbf{E}}^H$ and the SENSE-SVD solution is represented as:

$$\hat{\mathbf{s}}_{\text{SVD}} = \mathbf{V}_{\mathbf{E}}\mathbf{\Sigma}_{\mathbf{E}}^{-1}\mathbf{U}_{\mathbf{E}}^H\mathbf{y} = \sum_{i=1}^R \frac{\mathbf{u}_i^H\mathbf{y}}{\sigma_i}\mathbf{v}_i. \quad (3.9)$$

The SVD and the standard SENSE solution are mathematically equivalent. Note that small values of σ_i represent potential numerical instabilities in the reconstruction. Since small singular values will be inverted to large values, either noise or errors in sensitivity estimation affecting the singular vectors associated with these small singular values will be amplified in the reconstruction resulting in a decreased SNR and residual aliasing artifacts. This situation is particularly evident in regions with overlapped and/or low-value coil sensitivities where the coils are not able to provide distinct information and the encoding matrix becomes close to singular. If the number of singular values is high, the truncated SVD solution [53] could be used to eliminate the components responsible for noise and error propagation by setting a minimum singular value threshold. However; for SENSE we have only R singular values, commonly $R < 10$, therefore it is not possible to separate those components.

Instead of truncating the SVD, the set of singular values can be shifted away from zero using a shift value given by a small portion of the largest singular value, then the solution components for large singular values will remain similar to the non-shifted SVD while the components corresponding to small singular values will be attenuated. The shifted-SVD (SSVD) approach proposed in this work shifts the

set of singular values away from zero using a minimum singular value shift based on an upper bound on the condition number (CN) of \mathbf{E} (c_0). The shifted singular values are given by:

$$\sigma_i^s = \sigma_i + \Delta\sigma = \sigma_i + \frac{\sigma_{max}}{c_0}, \quad (3.10)$$

where σ_{max} is the largest singular value. The condition number (CN) is the ratio of the maximum to the minimum singular value. In this way, the set of singular values will be shifted away from zero by adding a minimum singular value to improve the conditioning of \mathbf{E} . The shifted SVD (SSVD) of \mathbf{E} is then $\mathbf{E}_S = \mathbf{U}_E \mathbf{\Sigma}_E^s \mathbf{V}_E^H$, where $\mathbf{\Sigma}_E^s$ is a diagonal matrix with the shifted singular values. Note that \mathbf{E}_S is a shifted version of \mathbf{E} . Since we have a large CN for an ill-conditioned matrix, e.g. $CN > 1000$, and c_0 is chosen in the range of a well-conditioned matrix, e.g. $10 < c_0 < 100$, the shift is very small for large singular values but it is significant for small singular values which are responsible for numerical instabilities. If the encoding matrix is well-conditioned, e.g. $CN=5$, \mathbf{E}_S remains very close to \mathbf{E} (Fig. 3.2)

The SENSE-SSVD solution is given by:

$$\hat{\mathbf{s}}_{SSVD} = \mathbf{V}_E \mathbf{\Sigma}_E^s{}^{-1} \mathbf{U}_E^H \mathbf{y} = \sum_{i=1}^R \frac{\mathbf{u}_i^H \mathbf{y}}{\sigma_i + \Delta\sigma} \mathbf{v}_i. \quad (3.11)$$

Note that the method acts like a filter, attenuating more the effect of small singular values. For example, assuming that $c_0 = 50$, then $\Delta\sigma = 0.02 \sigma_{max}$. For components with $\sigma_i > 0.2 \sigma_{max}$, the difference will be less than 10%. Components with $\sigma_i \approx$

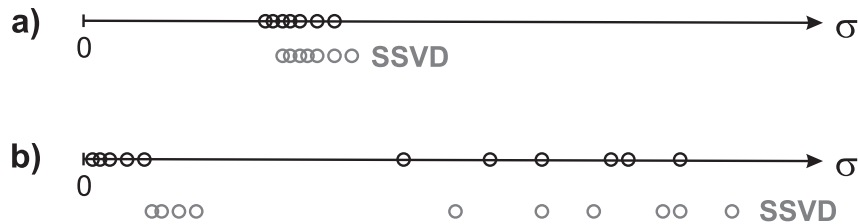


Figure 3.2: Effect of SSVD regularization on the set of singular values for: a) well-conditioned matrix and b) ill-conditioned matrix.

$\Delta\sigma$ will be attenuated by a factor of 2. Since small singular values correspond to more oscillatory singular vectors, the method is attenuating fine details in the reconstructed image. Therefore, with SSVD regularization, we are improving the SNR and reducing the effect of model errors at the expense of blurring in regions susceptible to numerical instability.

The difference between the SVD and the SSVD solution is given by:

$$\hat{\mathbf{s}}_{\text{SVD}} - \hat{\mathbf{s}}_{\text{SSVD}} = \sum_{i=1}^R \frac{\Delta\sigma}{\sigma_i} \frac{\mathbf{u}_i^H \mathbf{y}}{\sigma_i + \Delta\sigma} \mathbf{v}_i. \quad (3.12)$$

Note that for components with large singular values and therefore small $\Delta\sigma/\sigma_i$, the difference is very small.

The regularization procedure will reduce g-factor since it improves the conditioning of the matrix \mathbf{E} and consequently of $\mathbf{E}^H \mathbf{E}$ at the expense that certain features will be omitted in the reconstructed image, e.g. blurring in positions with strongly overlapped coil sensitivities. Therefore it allows a tunable tradeoff between ideal accuracy and practical image quality.

3.3.1 Relation to Tikhonov Regularization

Setting $\mathbf{s}_0 = 0$, the SENSE-Tikhonov solution is given by:

$$\hat{\mathbf{s}}_t = \left(\mathbf{E}^H \mathbf{E} + \lambda^2 \mathbf{I} \right)^{-1} \mathbf{E}^H \mathbf{y}. \quad (3.13)$$

This solution can be represented using the SVD formulation in the following way:

$$\hat{\mathbf{s}}_t = \sum_{i=1}^R \frac{\sigma_i^2}{\sigma_i^2 + \lambda^2} \frac{\mathbf{u}_i^H \mathbf{y}}{\sigma_i} \mathbf{v}_i = \sum_{i=1}^R \frac{\mathbf{u}_i^H \mathbf{y}}{\sigma_i + \frac{\lambda^2}{\sigma_i}} \mathbf{v}_i. \quad (3.14)$$

Tikhonov regularization can be thought as the SSVD solution with $\Delta\sigma = \lambda^2/\sigma_i$.

3.3.2 Tuning the Regularization Parameter

The regularization parameter c_0 can be selected from the reconstruction of the reference data to estimate the sensitivity maps which is always acquired in accelerated parallel MRI. For example, reconstructing for different values of c_0 between 10 and 100 with steps of 5 and choosing the value of c_0 that provides the smallest root mean square error (RMSE). For optimal results, c_0 needs to be re-optimized for each geometry/subject, which does not represent an increase in acquisition time, only extra processing time.

3.4 Simulations

Coil sensitivity maps were simulated using the Biot-Savart law and the circular array geometry with 8 elements shown in Fig. 2.3. Multiple receiver coil data were created by multiplying a Shepp-Logan phantom with the coil sensitivity maps. Two simulations were performed: (a) noiseless data and (b) noisy data: adding Gaussian noise to have a SNR=50. The first data set will be used to assess the performance with respect to errors in the sensitivity maps and the second for noise amplification in the reconstruction. Accelerated data were simulated by decimating the k-space data from each coil uniformly according to the given acceleration factor (R). Fully-encoded data were reconstructed by applying the Fourier transform to each channel and sensitivity-weighted combination (DFT-SWC), i.e. SENSE with $R = 1$. To visualize the degree of aliasing, the accelerated image was conventionally reconstructed by DFT to each channel and sum-of-squares (DFT-SOS) combination. SNR in the reconstructed image was computed by the ratio of the mean value and the standard deviation of a region outside the object.

3.4.1 1D acceleration of the noisy data

The standard SENSE reconstruction presented a high SNR loss especially in the central region where g-factor is higher (Fig. 3.3). The average SNR loss was 25.7 which is in agreement with the theoretical value of $\bar{g}\sqrt{R} = 24.6$. SENSE-SSVD provided lower g-factors and thus increased SNR in the reconstructed image at the expense of residual aliasing. The optimal point for the tradeoff between SNR and residual aliasing was found at $c_0 = 50$ where the average g-factor was 3.6 and the computed SNR loss was 9.2 ($\bar{g}\sqrt{R} = 7.2$).

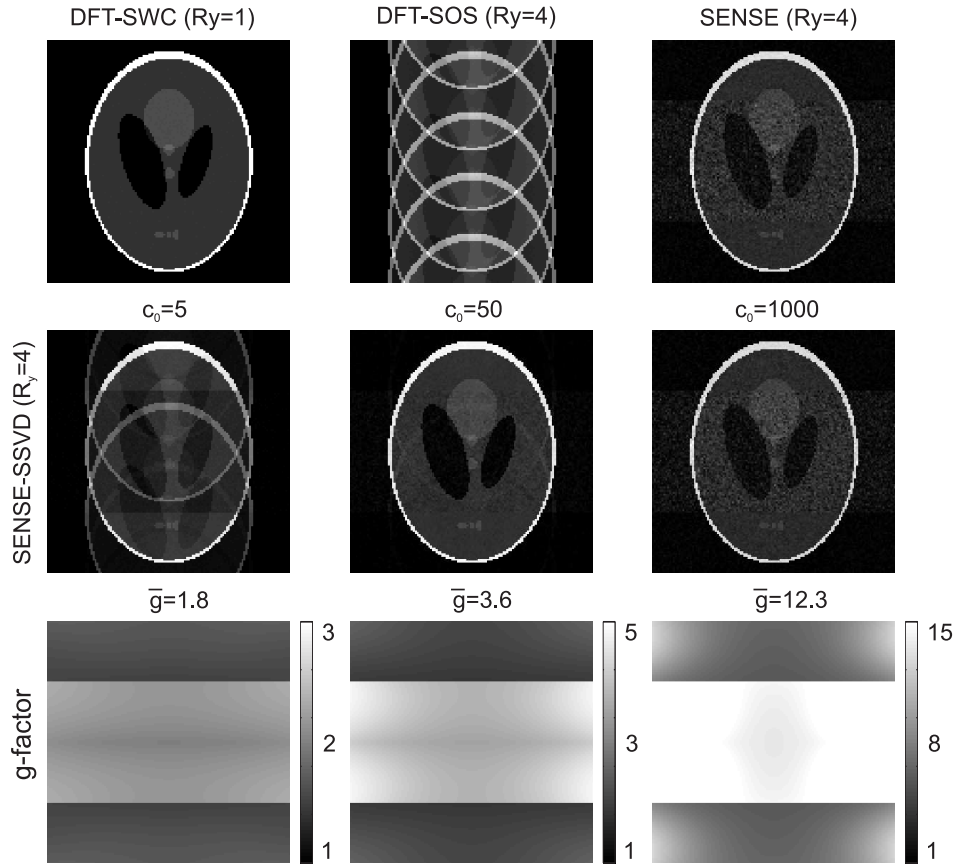


Figure 3.3: Reconstruction of the noisy data with 1D acceleration ($R = 4$) using standard SENSE and SENSE-SSVD for different c_0 values.

3.4.2 2D acceleration of the noisy data

2D acceleration presented lower and more uniform g-factor than 1D acceleration for the same overall R (Fig. 3.4). The optimal regularization parameter for the tradeoff between SNR and residual aliasing was found at $c_0 = 25$ where the average g-factor was 1.3 and the computed SNR loss was 3.1 ($\bar{g}\sqrt{R} = 2.6$). SSVD regularization presented an improved performance for 2D acceleration than for 1D acceleration since g-factor is lower and more uniform.

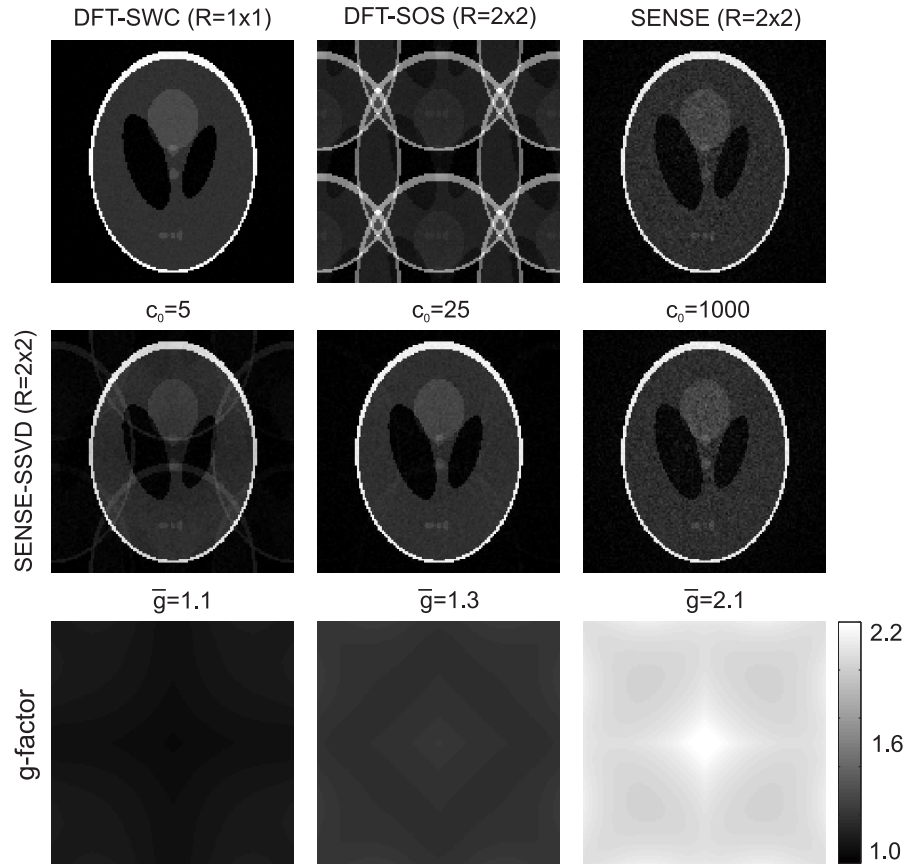


Figure 3.4: Reconstruction of the noisy data with 2D acceleration ($R = 2 \times 2$) using standard SENSE and SENSE-SSVD for different c_0 values.

3.4.3 2D acceleration of the noiseless data with inaccurate coil sensitivity maps

Reconstruction with inaccurate coil sensitivity information was simulated with biased coil sensitivity maps. The biased sensitivity map for the l -th coil is given by $c'_l(\mathbf{r}) = c_l(\mathbf{r}) + 0.05c_l^{\max}$. Standard SENSE reconstruction produced artifacts due to amplified model errors ($\bar{g} = 2.4$). SENSE-SSVD reduced the effect of inaccurate sensitivity function due to a better conditioning of the encoding matrix ($\bar{g} = 1.6$).

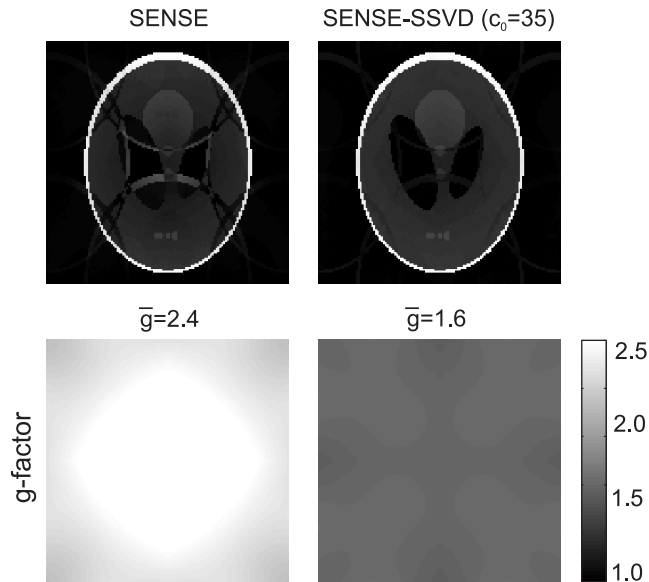


Figure 3.5: Reconstruction of the noiseless data with 2D acceleration ($R = 2 \times 2$) and bias error in the coil sensitivity profiles ($\Delta \mathbf{E} = 0.05 \mathbf{E}$).

3.5 Experiments

Human brain data were acquired using a 3 Tesla MR scanner equipped with the 32-channel soccer-ball array [25]. A gradient-echo sequence was employed with 256×256

spatial matrix and FOV of $256 \times 256 \text{ mm}^2$. Coil sensitivity maps were estimated following the procedure indicated in section 2.2.4. Fully-encoded data was reconstructed using the DFT-SWC method. A high 2D acceleration with $R = 4 \times 4$ was simulated by decimating the k-space data from each coil uniformly. Reconstruction results are presented in Fig. 3.6. Standard SENSE reconstruction has noticeable errors specially in the central region due to the combined effect of noise and model error amplification ($\bar{g} = 2.9$). SENSE-SSVD reduced this amplification ($\bar{g} = 1.6$) providing a higher quality reconstruction (RMSE=13.4%).

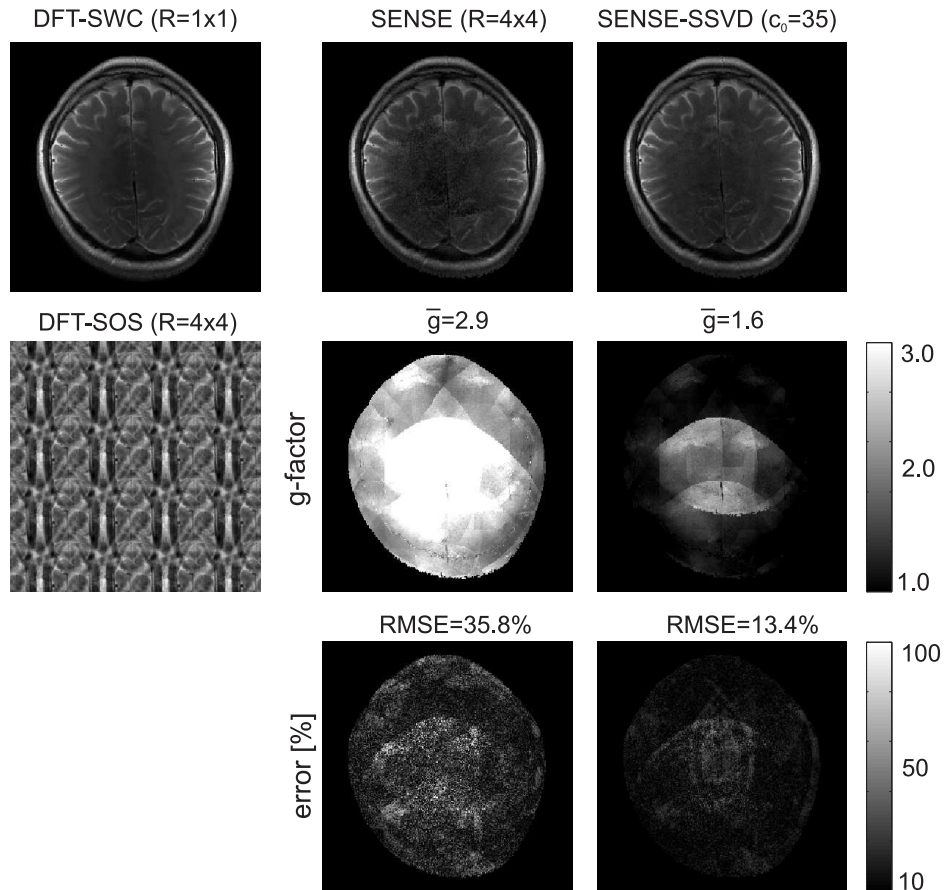


Figure 3.6: Reconstruction of the human brain data with high 2D acceleration ($R = 4 \times 4$) using standard SENSE and SENSE-SSVD ($c_0 = 35$). The error images are taken with respect to the fully-encoded reconstruction (DFT-SWC).

3.6 Discussion

The regularization approach presented in this Chapter was intended to reduce noise and model error amplification by constraining the matrix inversion at the expense of reducing the ideal reconstruction accuracy. For example, for the case of noisy data, SNR was increased at the expense of residual aliasing. For most of the applications, the increase in SNR compensates for the small residual aliasing offering a reconstructed image with higher quality.

Regularization of the encoding matrix inversion can be performed by constraining the SVD solution of the inverse problem. One possible strategy is to truncate the singular values which are lower than a certain threshold. This solution, known as truncated SVD, can be applied when the encoding matrix is sufficiently large so that the fraction of eigenvalues retained still provides a reasonable approximation to the true solution [49]. For SENSE, a small encoding matrix is used for each position in the aliased images, therefore the number of singular values is very small and truncated SVD is not an adequate approach. In this work, we proposed the SSVD solution, which consists of shifting the set of singular values of the encoding matrix away from zero based upon a threshold on the condition number. The method proved to work adequately for SENSE to improve the conditioning of the encoding matrix in positions with low-value and overlapped coil sensitivities at the expense of reduction in ideal reconstruction accuracy.

In SSVD regularization, the degree of regularization is adapted automatically to each spatial region, since the shifting value ($\Delta\sigma = \sigma_{max}/c_0$) depends on the maximum singular value of the encoding matrix being employed. Therefore, it is more robust than the conventional Tikhonov regularization where the regularization parameter is a constant over the image. Moreover, the tuning of the regularization parameter is simpler than with Tikhonov regularization methods that use prior images, e.g.

L-curve. Since the reference image is only used to tune the optimal value to shift the set of singular values, inconsistencies between the reference and the acquisition will not be reflected in the final reconstruction.

In conclusion, SSVD regularization presents an effective tradeoff between ideal reconstruction accuracy and practical image quality for parallel MRI applications. The method is ideally suited for high accelerations where a significant SNR loss is produced due to ill-conditioning of the encoding matrix.

3.7 Summary

A novel regularization method of the inverse problem based on the SVD representation of the encoding matrix was presented for SENSE-like parallel MRI reconstruction. The method improves the SNR and reduce the effect of systematic errors in coil sensitivity estimation at the expense of loss in ideal reconstruction accuracy. SSVD regularization offers an efficient alternative to the commonly used Tikhonov regularization with a simpler tuning of the regularization parameter. The degree of regularization is automatically adapted to each spatial region in order to regularize only where it is required. The method is expected to work adequately for different array geometries and k-space sampling strategies.

Chapter 4

Parallel MRI with Variable k-Space Sub-Sampling

Uniform sub-sampling of k-space is not optimal for parallel MRI if the coil sensitivities overlap, which is the case in practice. Variable density k-space sub-sampling schemes that reduce the mean square error of the reconstruction with uniform k-space sub-sampling are investigated in this Chapter. A general framework for parallel MRI with arbitrary k-space sub-sampling is also presented.

4.1 Introduction

Parallel MRI methods make use of multiple receiver coils with different spatially-varying sensitivities to simultaneously acquire a region in k-space at a time instead of a single k-space point. The extent of that region is given by the shape of the spatial Fourier transform of the coil sensitivities. This reduces the effective field of view (FOV) for each coil and thus relaxes the k-space Nyquist sampling rate requirement. For example, to obtain a reconstruction free of aliasing with a single receiver coil, the

distance between k-space samples cannot exceed the Nyquist sampling interval $\Delta k = 1/W$, where W is the FOV. For two receiver coils with non-overlapping sensitivities the required sample spacing is doubled to $2/W$ since the FOV for each coil is half of the total FOV and therefore the acquisition process can be accelerated by a factor of 2. However, this analysis is not appropriate for coil sensitivities with partial overlap which is the case in practice. The effect of overlapped coil sensitivities can be reduced in part by the pre-whitening procedure presented in Chapter 3, which minimizes the correlation between coils. In general, the k-space sampling positions should be selected according to the partial overlap between coil sensitivities. For example, in the SPACE-RIP method [18] data is sampled at the Nyquist rate at the center of k-space and more sparsely as we move away from the center. This variable density sampling scheme is based on the property that most of the information content is concentrated within a small region at low k-space values whereas the edge information is distributed over a much broader region of higher k-space values. Aggarwal *et al.* [19] presented a more rigorous approach where the sampling positions were chosen considering the object and noise spatial statistics. The object was modeled as a stationary Gaussian random process and the optimal sampling scheme was derived by minimizing the mean squared error (MSE).

Parallel MRI reconstruction with arbitrary sub-sampling of k-space requires inversion of the complete encoding matrix since each spatial point can potentially alias with all the others. For the case of variable sub-sampling along one spatial dimension, the inversion can be performed separately for each point in the other dimensions. For variable sub-sampling along two spatial dimensions, the size of the encoding matrix makes impractical a straightforward inversion. Iterative methods such as the Conjugate Gradient can be used to solve the inverse problem [54].

This Chapter presents a general model and reconstruction method for parallel MRI with arbitrary k-space sub-sampling schemes and a method for selection of

k-space samples under partial overlap between coil sensitivities. Selection of by reducing the mean square error (MSE) of the reconstruction with respect to the fully-sampled reconstruction. In contrast to [19], the approach only make use of the sensitivity maps and thus is object independent. Variable density sub-sampling schemes that reduce the mean square error of the reconstruction with uniform sub-sampling are presented.

4.2 Parallel MRI Modeling and Reconstruction for Arbitrary k-Space Sub-Sampling

The general approach for parallel MRI reconstruction is to first build the forward model that relates the sub-sampled k-space data with the fully-sampled k-space representation of the image to be reconstructed. This relationship is given by the encoding matrix which represents the combined effect of gradient and sensitivity encoding. The reconstructed image is then computed by the inverse of the encoding matrix. In this Section a general forward model in the spatial domain is presented for parallel MRI with arbitrary k-space sub-sampling as well as practical reconstruction algorithms to efficiently invert the encoding matrix.

4.2.1 Forward Model

Considering the discretization of the object function to N_r points (reconstruction grid), and the acquisition of N_k k-space points (acquisition grid), a discretized version of the signal acquired by each coil in k-space can be represented as:

$$Y_{l,n} = \sum_{l=1}^{N_c} s[\mathbf{r}_m] c_l[\mathbf{r}_m] e^{j2\pi\mathbf{k}_n \cdot \mathbf{r}_m}, \quad (4.1)$$

where $n = 1, 2, \dots, N_k$ is the sampling index, $m = 1, 2, \dots, N_r$ is the reconstruction index and $l = 1, 2, \dots, N_c$ is the coil index. This equation can be also represented as:

$$\mathbf{F}_{N_k} \mathbf{y}_l = \mathbf{F}_{N_r} \mathbf{C}_l \mathbf{s}, \quad (4.2)$$

where F_N ($N \times N$) is the discrete spatial Fourier transform matrix, \mathbf{y}_l ($N_k N_c \times 1$) is the aliased observation vector in the spatial domain, \mathbf{C}_l ($N_r \times N_r$) is a diagonal matrix with the l -th coil sensitivity values and \mathbf{s} ($N_r \times 1$) is the image to be reconstructed. After applying a spatial inverse Fourier transform, the encoding equation for the l -th coil in the spatial domain can be expressed as:

$$\mathbf{y}_l = \mathbf{F}_{N_k}^{-1} \mathbf{S} \mathbf{F}_{N_r} \mathbf{C}_l \mathbf{s} = \mathbf{E}_l \mathbf{s}, \quad (4.3)$$

where \mathbf{S} ($N_k \times N_r$) is the sampling matrix relating the reduced and full sampling schemes. The element $S(i, j) = 1$ if the k-space position with index j is sampled and equal to 0 otherwise. After concatenating the encoding equations from all coils, we obtain the complete encoding equation:

$$\mathbf{y} = \mathbf{E} \mathbf{s}, \mathbf{y} = \begin{bmatrix} \mathbf{y}_1 \\ \mathbf{y}_2 \\ \vdots \\ \mathbf{y}_{N_c} \end{bmatrix}, \mathbf{E} = \begin{bmatrix} \mathbf{E}_1 \\ \mathbf{E}_2 \\ \vdots \\ \mathbf{E}_{N_c} \end{bmatrix} \quad (4.4)$$

Note that the encoding equation provides a general forward model for arbitrary sub-sampling over a Cartesian grid.

4.2.2 Inverse Reconstruction

Parallel MRI reconstruction with arbitrary sub-sampling of k-space requires inversion of the complete encoding matrix since each spatial point can potentially alias with all the others. For the case of variable sub-sampling along one spatial dimension,

the inversion can be performed separately for each point in the other dimensions. For example, in 2D MRI acceleration is only practical along the phase-encoding dimension (y). Therefore, the complete inversion can be performed separately for each point along the x dimension using the conventional pseudo-inverse approach. Using the general model and reconstruction, artifacts in SENSE reconstruction with odd uniform acceleration factors can be removed (Fig. 4.1).

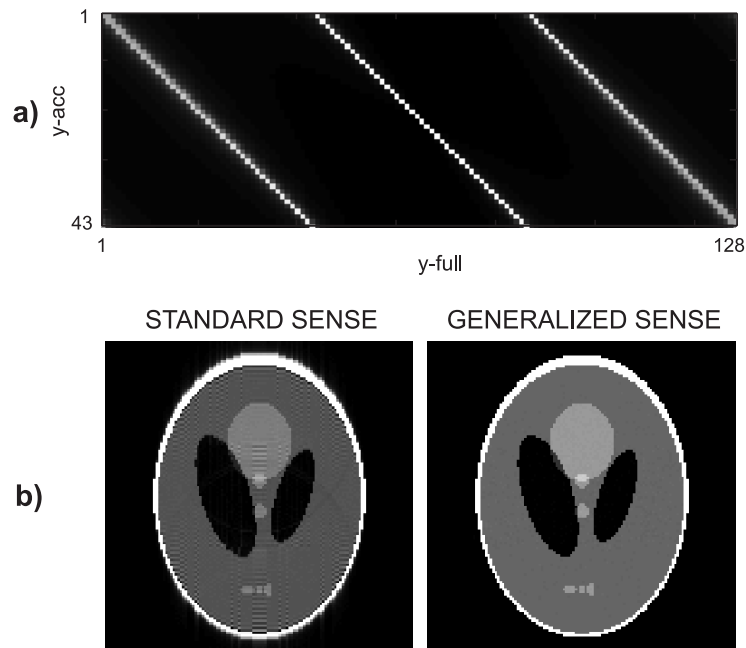


Figure 4.1: a) Effect of k -space sub-sampling with $R_y = 3$. Note that each point in the sub-encoded image (y -acc) is a combination of more than 3 points from the fully-encoded image (y -full). b) Standard SENSE reconstruction presents artifacts due to the modeling errors described in part a). c) SENSE reconstruction with the general model removes the artifacts.

For 3D MRI, acceleration can be performed along the two phase encoding dimensions (y and z). Conventional inversion of the complete encoding matrix is impractical due to computational requirements. The solution of the inverse problem

in parallel MRI leads to the following normal equations:

$$\mathbf{E}^H \mathbf{E} \mathbf{s} = \mathbf{E}^H \mathbf{y}. \quad (4.5)$$

The system can be solved iteratively using the Conjugate Gradient (CG) algorithm since it is conjugate symmetric and the encoding matrix is positive definite as it was described by Pruessmann *et al.* for the case of SENSE reconstruction with non-Cartesian trajectories [54]. In this work, we are using the same approach but for the case of Cartesian sampling of k-space where density correction and regridding are not required.

The rate of convergence of the conjugate gradient algorithm depends on the conditioning of the encoding matrix \mathbf{E} . If the singular values cluster around a fixed point, e.g. well-conditioned matrix, the solution will be stable and convergence will be fast. Pre-conditioning can be used to achieve faster convergence. The idea behind pre-conditioning is to transform the original system to improve the conditioning of the encoding matrix [55]. Pre-conditioning can be also thought as a regularization method since the condition of the encoding matrix is improved (see Chapter 5 for more details). Consider a symmetric, positive-definite matrix \mathbf{M} that approximates $\mathbf{E}^H \mathbf{E}$, but is easier to invert. We can solve the original normal equations by solving $\mathbf{M}^{-1} \mathbf{E}^H \mathbf{E} \mathbf{s} = \mathbf{M}^{-1} \mathbf{E}^H \mathbf{y}$ instead. Now, this transformed system may not be positive definite. In order to force this property, the following decomposition of the matrix \mathbf{M} can be used: $\mathbf{M}^{-1} = \mathbf{C} \mathbf{C}^H$. Since the matrices $\mathbf{M}^{-1} \mathbf{E}^H \mathbf{E}$ and $\mathbf{C} \mathbf{E}^H \mathbf{E} \mathbf{C}^H$ have the same singular values, the original normal equations can be transformed into the following positive definite system [55]:

$$\left(\mathbf{C} \mathbf{E}^H \mathbf{E} \mathbf{C}^H \right) \left(\mathbf{C}^{-H} \mathbf{s} \right) = \mathbf{C} \mathbf{E}^H \mathbf{y}, \quad (4.6)$$

which can be solved iteratively using the CG algorithm. For \mathbf{M} we can use the matrix $\mathbf{E}^H \mathbf{E}$ for the case of fully-encoding where we have a diagonal matrix with entries given by the sum of coil sensitivity squares, i.e. $m_{i,i} = \sum_{l=1}^{N_c} |c_l(\mathbf{r}_i)|^2$. Note that this matrix

is symmetric and positive definite. Therefore, the matrix \mathbf{C} ($N_r \times N_r$) will be also diagonal with entries:

$$c_{i,i} = \frac{1}{\sqrt{\sum_{l=1}^{N_c} |c_l(\mathbf{r}_i)|^2}}, \quad (4.7)$$

and the pre-conditioned normal equations are given by:

$$(\mathbf{C}\mathbf{E}^H\mathbf{E}\mathbf{C}) (\mathbf{C}^{-1}\mathbf{s}) = \mathbf{C}\mathbf{E}^H\mathbf{y}. \quad (4.8)$$

The proposed iterative image reconstruction consists basically of the following steps:

- Compute the right side of the pre-conditioned normal equations: $\mathbf{a} = \mathbf{C}\mathbf{E}^H\mathbf{y}$.
- The i -th CG iteration determines the solution $\hat{\mathbf{b}}_i$ of $(\mathbf{C}\mathbf{E}^H\mathbf{E}\mathbf{C}) \mathbf{b}_i = \mathbf{a}$.
- The approximate solution for the i -th iteration is given by: $\hat{\mathbf{s}}_i = \mathbf{C}\mathbf{b}_i$.

Each iteration provides a refined approximation $\hat{\mathbf{s}}_i$ of the exact solution until the norm of the residual $\|\mathbf{E}^H\mathbf{E}\mathbf{s} - \mathbf{E}^H\mathbf{y}\|$ converges to a minimum. The stopping point was established when the norm of the residual falls below a small fraction ϵ of the initial residual. Since the exact solution is not known, the accuracy of the current approximation can be estimated using the relative error in the second step of the iterative reconstruction:

$$\delta_i = \frac{\|\mathbf{C}\mathbf{E}^H\mathbf{E}\mathbf{C}\hat{\mathbf{b}}_i - \mathbf{a}\|}{\|\mathbf{a}\|}. \quad (4.9)$$

When $\delta_i < \epsilon$, the CG iterations will stop and the corresponding $\hat{\mathbf{s}}_i$ is set as the final solution.

4.3 Variable Density k-Space Sampling

Optimal selection of k-space samples for parallel MRI under the presence of partial overlap between coil sensitivities can be performed by choosing N_k points out of

N_r points that gives the minimum mean square error (MSE) reconstruction ($R = N_r/N_k$). Considering the pre-whitened encoding equation for parallel MRI acquisition $\mathbf{y} = \mathbf{E}\mathbf{s}$ and the least-squares solution $\hat{\mathbf{s}} = (\mathbf{E}^H\mathbf{E})^{-1}\mathbf{E}^H\mathbf{y}$, the MSE of the reconstructed image is given by:

$$\text{MSE} = E [\|\mathbf{s} - \hat{\mathbf{s}}\|^2] = \text{trace} \left\{ (\mathbf{E}^H\mathbf{E})^{-1} \right\}, \quad (4.10)$$

where E is the expectation operator. The exhaustive search for the N_k best k-space points is a combinatorial optimization problem and thus is impractical for parallel MRI applications.

In this Chapter, a variable density sampling scheme is developed based on the k-space representation of the coil sensitivity maps. The idea is to increase the sampling distance as we move away from the center of k-space, as in the SPACE-RIP method [18], but using the density of the coil sensitivities in k-space. The sub-sampling method reduces the MSE of the reconstruction using uniform sub-sampling at the expense of g-factor amplification due to increased distance between samples especially at high k-space values. Therefore, regularization must be used with variable density sub-sampling to achieve an appropriate SNR in the reconstructed image.

SSVD regularization (see Chapter 3) was employed with the variable density sub-sampling scheme for acceleration along one spatial dimension. The regularization parameter was adjusted in order to minimize the MSE error described above. Fig. 8.2 shows an example using the simulated 8-channel circular array and acceleration along the y dimension. The k-space representation of the coil sensitivity maps were fitted to a piece-wise linear function in order to select 32 points out of 128 ($R = 4$). The slope of the piece-wise linear function increased from 1 (k-space center) up to 9 (k-space periphery). SENSE with uniform sub-sampling (SENSE-US) presented low SNR in the reconstruction. SENSE with variable sub-sampling (SENSE-VS) outperforms SENSE-US when using regularization presenting a reconstruction free of residual aliasing artifacts with appropriate SNR.

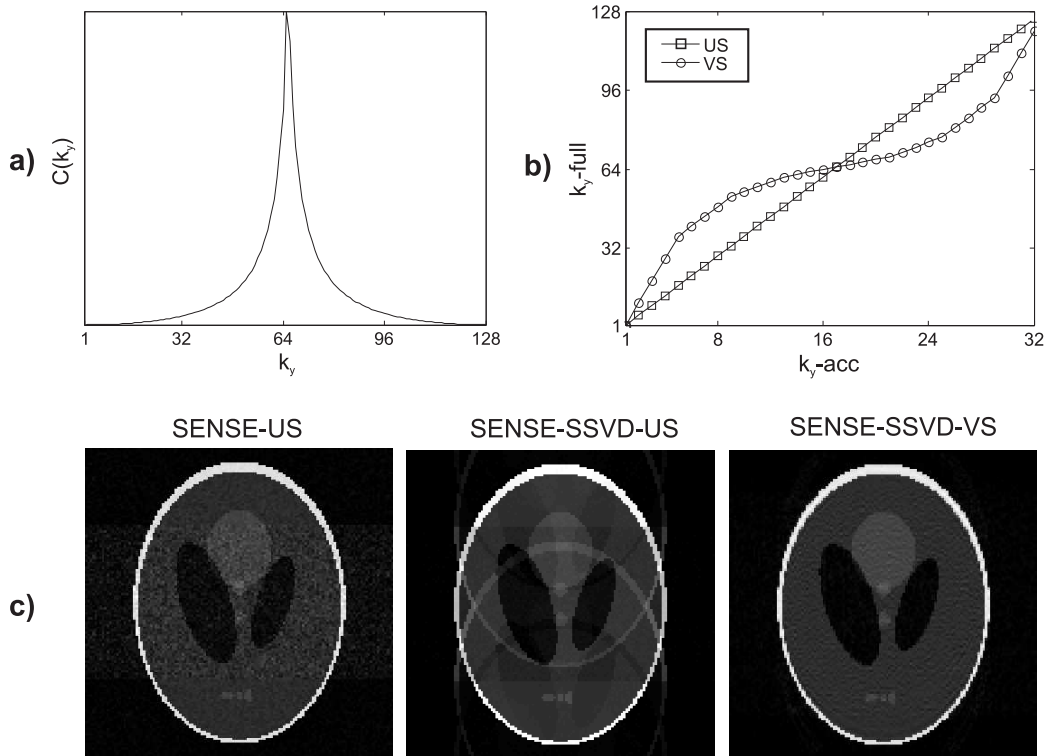


Figure 4.2: a) k -space representation of the coil sensitivity maps. b) Piece-wise linear variable density sub-sampling (VS) and uniform sub-sampling (US) schemes for $R = 4$. The slope of the linear function varies according to the k -space density of the coil sensitivity maps. c) SENSE reconstruction with uniform sub-sampling (US) and SSVD regularization reduces noise at the expense of residual aliasing. Residual aliasing in the SSVD regularization is removed by the variable density k -space sub-sampling approach.

The conjugate gradient algorithm with pre-conditioning and variable density sub-sampling scheme was employed for acceleration along two spatial dimensions. Fig. 8.3 shows an simulation example using the 32-channel soccer-ball array and acceleration along x and y dimension. The k -space representation of the coil sensitivity maps was fitted to a 2D piece-wise linear function in order to select 32×32 points out of 128×128 ($R = 4 \times 4$). The residual aliasing in SENSE with uniform sub-sampling was highly reduced for the variable sub-sampling scheme.

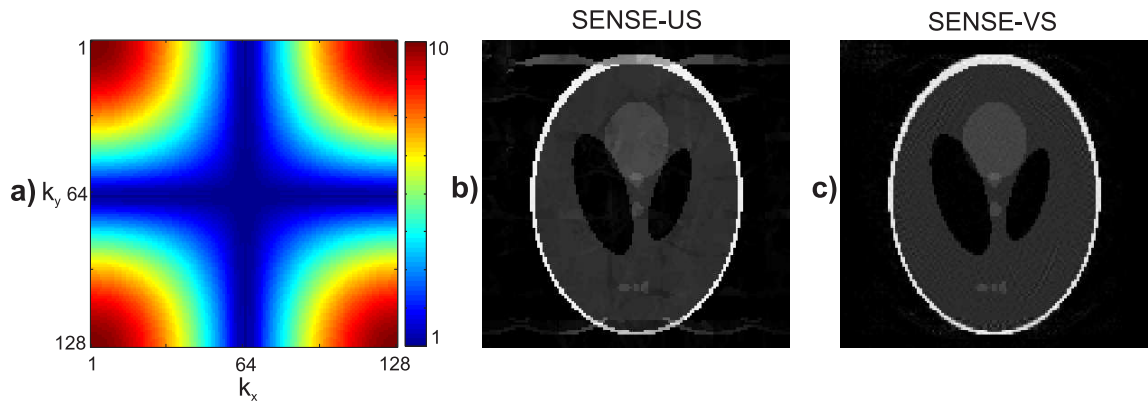


Figure 4.3: a) Map of the variable sub-sampling distance given by the 2D k -space density of the coil sensitivities. b) SENSE reconstruction with uniform sub-sampling. c) SENSE reconstruction with the variable sub-sampling given in a).

4.4 Summary

This Chapter presented a general framework for parallel MRI with arbitrary k -space sub-sampling. A practical variable density k -space sub-sampling using the k -space density of the coil sensitivity maps was presented. The approach reduces the mean square error of reconstruction with uniform k -space sub-sampling and it is advantageous for cases where regularization is used.

Chapter 5

Superresolution Parallel MRI Reconstruction

³ Parallel MRI reconstruction is formulated as a superresolution problem where acceleration is performed by acquiring the low spatial resolution representation of the object being imaged and receiver coil sensitivity maps are acquired with higher target spatial resolution. The increase in spatial resolution will be determined by the degree of coil sensitivity variation within the low resolution image voxel. The method is applicable to receiver arrays with a large number of small elements which provide strong spatial variation of the coil sensitivity maps. Superresolution Sensitivity-Encoding (SURE-SENSE) represents an alternative approach to standard SENSE for the same acceleration factor and it is advantageous for low spatial resolution imaging which present stronger variation of the coil sensitivities within the image voxel.

³The work in this chapter was published as: R. Otazo, R. Jordan, F-H. Lin and S. Posse. “Superresolution Parallel MRI”. Proceedings of the 14th IEEE International Conference on Image Processing (ICIP), San Antonio, USA, 2007, pp. III-153-156. Submitted as a full paper to Magnetic Resonance in Medicine.

5.1 Introduction

MRI methods involve imaging objects with high k-space content in a limited amount of time. However, due to SNR and time constraints, information over only a limited k-space range is usually acquired in practice. For example, in MRSI which is constrained by low SNR and slow encoding methods, k-space coverage is sacrificed to achieve an adequate SNR within a feasible acquisition time. In functional MRI (fMRI), where a time-series of images is acquired, k-space coverage is traded off for increased temporal resolution.

The lack of high k-space information leads to limited spatial resolution and Gibbs ringing when the Fourier transform is directly applied to reconstruct the image. Constrained image reconstruction techniques using prior information [56] have been proposed to achieve superresolution image reconstruction, i.e to estimate high k-space values without actually measuring them. For example, the finite spatial support of an image can be used to perform extrapolation of k-space at expense of SNR loss. However, this method performs well only at positions close to the periphery defined by the spatial support [57]. For experiments with temporal repetitions such as MRSI and fMRI; k-space substitution[58], also known as key-hole method, was proposed to fill the missing high k-space values of the series of low resolution acquisitions using a high resolution reference. However, this method is vulnerable to artifacts due to inconsistencies between the reference and the actual acquisition. An improvement of this approach, known as generalized series reconstruction [59, 60], forms a parametric model using the high resolution reference to fit the series of low resolution acquisitions and thus reduce the effect of data replacement inconsistencies. Alternatively, superresolution reconstruction can be performed by combination of several low resolution images acquired with sub-pixel differences [61, 62]. This method is well developed for picture and video applications and was employed before in MRI by applying a sub-pixel spatial shift to each of the low resolution acquisitions [63, 64, 65].

However, this method is very limited since a spatial shift is equivalent to a linear phase modulation in k-space which does not represent new information to increase the k-space coverage of the acquisition.

Parallel MRI [15, 16] has been introduced as a method to accelerate the sequential gradient-encoding process by acquiring fewer k-space points using multiple receivers with different spatially-varying sensitivities. The standard strategy for accelerated encoding is to reduce the density of k-space sampling while maintaining the extent in order to have the same spatial resolution of the fully encoded acquisition. The rationale for this sub-sampling scheme is that the coil sensitivities are very smooth and retrieve k-space information only from the neighborhood of the actual gradient-encoding point. This acceleration could be used to increase k-space coverage in order to obtain a reconstructed image with higher spatial resolution. However, a larger coverage of k-space in the acquisition will produce a SNR loss that can be prohibitive for certain MRI modalities such as MRSI. In the other hand, standard SENSE reconstruction strictly removes aliasing only at the voxel center. Strong aliasing artifacts may occur for low spatial resolution imaging where the coil sensitivities are varying within the image voxel [66, 67]. Standard SENSE reconstruction with coil sensitivity information acquired with higher spatial resolution than the actual image along with minimum norm reconstruction were proposed to reduce this effect at the expense of g-factor amplification [67].

Parallel MRI using large-N arrays [21] provides higher sensitivity encoding capability due to stronger variation of the coil sensitivities in the spatial domain and thus extended k-space coverage. Extreme accelerated encoding with only one gradient-encoding point was presented using large-N arrays where all the spatial information was derived from the coil reception profiles. For example, a 64-channel planar array was employed in the Single Echo Acquisition (SEA) technique [68]. However, the in-plane resolution of this technique decreases rapidly with increasing depth, in ac-

cordance with the RF coil sensitivity profiles. In the Inverse Imaging (InI) technique [23], a 90-channel array and MEG-like inverse reconstruction were proposed for functional MRI of human brain with temporal resolution of only 20 ms. However, the price to pay for this extreme acceleration is reconstruction with low spatial resolution which is determined by the degree of variation of the coil sensitivity maps.

This Chapter presents a novel method for parallel MRI where acceleration is performed by acquiring only the central region of k-space instead of increasing the sampling distance over the complete k-space matrix. The proposed method, known as Superresolution SENSE (SURE-SENSE), increases the spatial resolution of the acquisition using coil sensitivities acquired with the target spatial resolution. The attainable increase in spatial resolution is determined by the degree of variation of the coil sensitivities within the acquired image voxel. The method is proposed for large-N arrays, which provide stronger variation of the coil sensitivity maps. Superresolution parallel MRI is intrinsically poor conditioned since the variation of coil sensitivities within the image voxel is lower than at larger distances. To overcome conditioning problems, a conjugate gradient algorithm with pre-conditioning is employed to solve the inverse problem. Comparison to standard SENSE reconstruction is presented at low spatial resolution in terms of residual aliasing artifacts and point spread function reconstruction. Application to MRSI of human brain is presented in Chapter 7 as a method to reduce lipid contamination and to enhance the spatial resolution of the metabolite maps.

5.2 Superresolution SENSE (SURE-SENSE)

The goal of superresolution image reconstruction is to combine information from different low resolution images that contain sub-pixel differences [61, 62]. For the case of parallel MRI, each receiver coil provides a different view of the same object

function according to the array geometry, e.g. in a circular array each coil provides a view from a different direction. Since the image acquired by each coil is weighted by the corresponding spatial sensitivity of the coil, superresolution is possible if the sensitivities are varying within the low resolution image pixel or different coils have a distinct sensitivity profile across the low resolution image pixels. Superresolution SENSE increases the spatial resolution of the acquisition using coil sensitivity maps acquired with the target spatial resolution (Fig. 5.1).

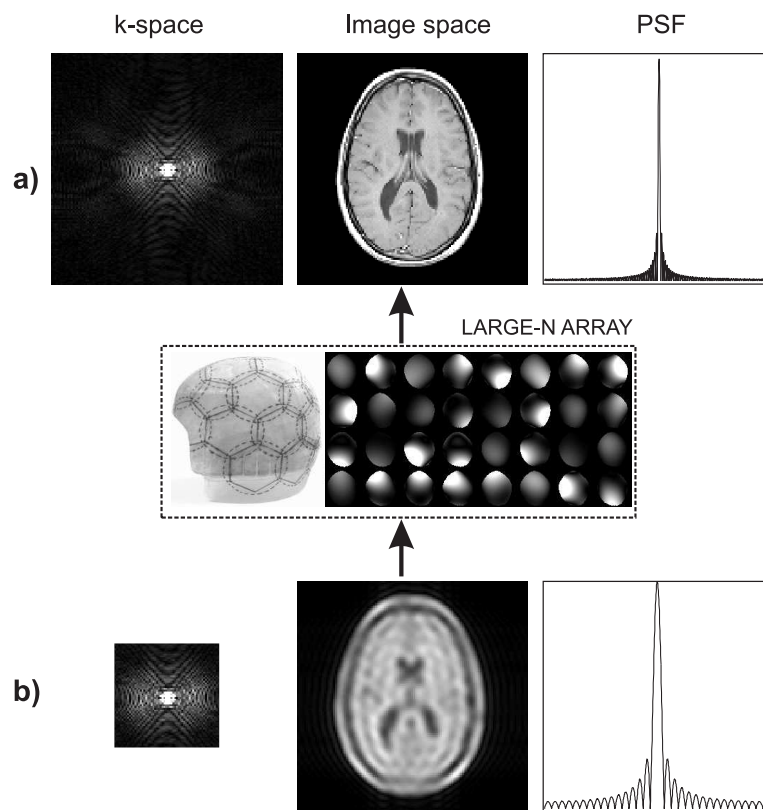


Figure 5.1: Superresolution parallel MRI idea. k-space representation, image and point spread function (PSF) for: a) high and b) low spatial resolution acquisitions. The high resolution data can be estimated from different low resolution acquisitions where the coil sensitivities are varying within the image voxel. Large-N arrays will provide improved performance due to stronger variation of the coil sensitivity maps and thus larger k-space coverage.

The working hypothesis of the first factor is that the coil sensitivities will provide extended k-space information. Even though this provides only limited k-space expansion for commercially available arrays with a small number of elements and therefore very smooth sensitivity functions, recently developed array designs with a large number of small elements will provide very localized information in the spatial domain that will increase k-space coverage of the sensitivity function [24] (Fig. 5.2).

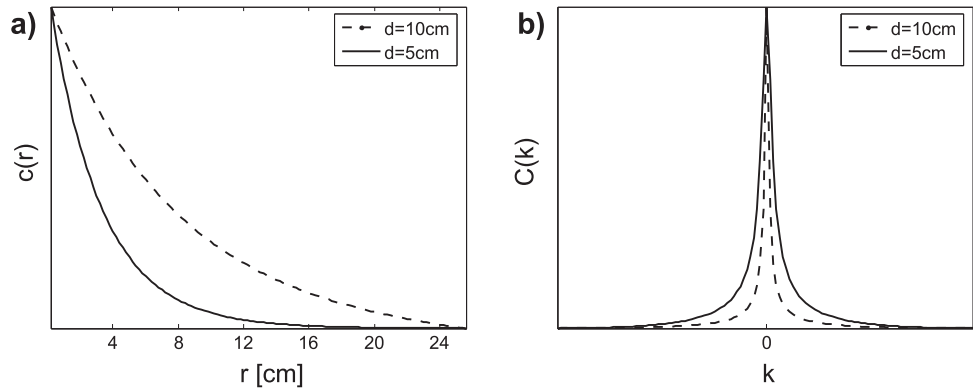


Figure 5.2: Coil sensitivity simulation using the Biot-Savart law [4] for coils with different diameters $d=5$ and 10 cm respectively. a) Spatial domain and b) k-space representation. Note that the stronger decay in the spatial domain increases the k-space extent of the coil sensitivity.

5.2.1 Acquisition Model

The forward model in matrix form $\mathbf{y} = \mathbf{E}\mathbf{s}$ is generated using the generalized model for parallel MRI with arbitrary k-space sampling presented in Section 4.3.1. For super-resolution parallel MRI, accelerated data is acquired from the central k-space region and coil sensitivity data is acquired from an extended k-space region determined by the target spatial resolution (Fig. 5.1). Both data sets are acquired at the Nyquist rate. The forward model describes the relationship between the acquired low resolution images (N_k -grid) and the high resolution sensitivity maps (N_r -grid). Comparison of

the effect of reduced k-space sampling in the spatial domain for standard (k-space sub-sampling) and superresolution SENSE (k-space truncation) is shown in Fig. 5.3. In superresolution SENSE, even though all the points from the fully encoded data are contributing to each point in the reduced data, most of the interaction is limited within the low resolution voxel.

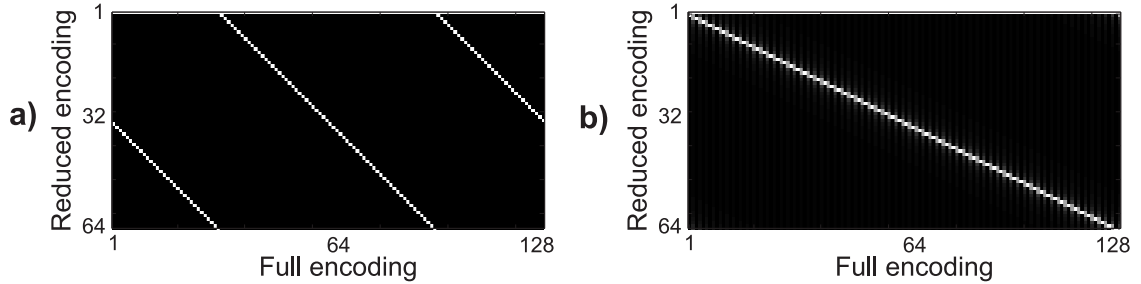


Figure 5.3: Effect of reduced k-space sampling with $R=2$ in the spatial domain for a) standard SENSE and b) superresolution SENSE. For standard SENSE, R equidistant points from the fully encoded data are combined in each point of the data with reduced encoding. For superresolution SENSE, all the points in the fully encoded data are combined in each point of the reduced data with weights given by the PSF of the low spatial resolution acquisition.

5.2.2 Image Reconstruction

Superresolution SENSE reconstruction is performed using the pre-conditioned conjugate algorithm presented in Section 4.3.2 for reconstruction of parallel MRI data acquired with arbitrary k-space sampling. Note that superresolution parallel MRI is intrinsically an ill-conditioned inverse problem. The encoding matrix in this case is more susceptible to become singular than in standard parallel MRI since the variation of coil sensitivities is lower within the low resolution voxel than at larger distances which is case for sub-sampled acquisitions. The idea behind pre-conditioning is to transform the original system to improve the conditioning of the transformed en-

coding matrix, which represents a regularization method by itself. Following the procedure indicated in Section 4.3.2, the original normal equations $\mathbf{E}^H \mathbf{E} \mathbf{s} = \mathbf{E}^H \mathbf{y}$ can be transformed to $\mathbf{M}^{-1} \mathbf{E}^H \mathbf{E} \mathbf{s} = \mathbf{M}^{-1} \mathbf{E}^H \mathbf{y}$, where \mathbf{M} is a symmetric, positive-definite matrix \mathbf{M} that approximates $\mathbf{E}^H \mathbf{E}$, but is easier to invert. In order to have a positive definite transformed system, the following decomposition of the matrix \mathbf{M} can be used: $\mathbf{M}^{-1} = \mathbf{C} \mathbf{C}^H$. Since the matrices $\mathbf{M}^{-1} \mathbf{E}^H \mathbf{E}$ and $\mathbf{C} \mathbf{E}^H \mathbf{E} \mathbf{C}^H$ have the same singular values, the original normal equations can be transformed into the following positive definite system [55]:

$$\left(\mathbf{C} \mathbf{E}^H \mathbf{E} \mathbf{C}^H \right) \left(\mathbf{C}^{-H} \mathbf{s} \right) = \mathbf{C} \mathbf{E}^H \mathbf{y}, \quad (5.1)$$

which can be solved iteratively using the CG algorithm (see Section 4.3.2 for more details). Note that the transformed system is well-conditioned since the singular values of the transformed matrix $\mathbf{C} \mathbf{E}^H \mathbf{E} \mathbf{C}^H$ will be clustered around 1. For \mathbf{M} we can use the matrix $\mathbf{E}^H \mathbf{E}$ for the case of fully-encoding where we have a diagonal matrix with entries given by the sum of coil sensitivity squares, i.e. $m_{i,i} = \sum_{l=1}^{N_c} |c_l(\mathbf{r}_i)|^2$. Therefore, the matrix \mathbf{C} ($N_r \times N_r$) will be also diagonal with entries:

$$c_{i,i} = \frac{1}{\sqrt{\sum_{l=1}^{N_c} |c_l(\mathbf{r}_i)|^2}}, \quad (5.2)$$

5.2.3 SNR and Spatial Resolution Analysis

The enhancement in spatial resolution comes at the expense of SNR loss dictated by the reduction in acquisition time and noise amplification in the reconstruction due to ill-conditioning of the encoding matrix (g-factor) [16]. The spatially-varying SNR loss is the same as in standard parallel imaging and it is given by:

$$\text{SNR}_{loss}(\mathbf{r}) = \frac{\text{SNR}_1}{\text{SNR}_R} = \sqrt{R} g(\mathbf{r}), \quad (5.3)$$

where SNR_1 corresponds to the fully-encoded reconstruction and SNR_R to the reduced-encoded reconstruction with a sampling reduction factor of $R = N_r/N_k$. The regu-

larization procedure presented before will enforce low values of g-factor which represents SNR gain at the expense of attenuating high spatial frequencies in the solution. Therefore, the maximum gain in spatial resolution is limited by the original g-factor that needs to be reduced by regularization in order to obtain an appropriate SNR which is in agreement with the fact that stronger sensitivity variations will result in higher acceleration factors.

5.3 Experimental Validation

Simulations and experiments were performed focusing on human brain imaging.

5.3.1 Scanner and Array Coil

Phantom and human brain data were acquired using a 3 Tesla MR scanner (Tim Trio, Siemens Medical Solutions, Erlangen, Germany). Head array coils with 32 [25] and 96 [26] receiver elements were used for RF reception, while RF transmission was performed with a quadrature body coil. The array coils were built with close-fitting helmet design and circular elements arranged in patterns of hexagonal and pentagonal symmetry similar to a soccer-ball for the 32-channel array and to a C240 bucky-ball for the 96-channel array (see Fig. 1.1). The 32-channel array offers nearly three-fold higher peripheral SNR and 20-30% higher SNR in the center of the head than the commercial 12-channel circular array. The 96-channel array presents a two-fold SNR gain in the periphery and close to 50% SNR gain in the center of the head when compared to the 32-channel array. Besides the high increase in sensitivity, the large number of small elements provide strong variation of the coil sensitivities in the spatial domain which translates to larger coverage in k-space and thus higher acceleration capability for superresolution SENSE.

5.3.2 High Resolution Coil Sensitivity Maps

Coil sensitivity maps were estimated at the high spatial resolution of the corresponding acquisition. Raw sensitivity maps were obtained dividing the image from each coil by the sum-of-squares combination of the multi-coil data to remove anatomical features. Refinement of the raw sensitivity maps was performed by a 4-th order polynomial fitting and spatial extrapolation beyond the borders of the object following the polynomial model as described in Section 2.4.4. The 4-th order polynomial was employed to accommodate stronger variations in the coil sensitivity model as required in SURE-SENSE.

5.3.3 Data Processing and Error Quantification

Low resolution data was obtained from the central k-space matrix. SURE-SENSE reconstruction was applied to the low resolution data using the high resolution coil sensitivity maps. For error quantification purposes, the high resolution acquisition was reconstructed by applying DFT reconstruction to each coil and sensitivity-weighted combination of the individual coil images (DFT-SW), i.e. standard SENSE reconstruction for the fully encoded data. For comparison purposes, the low resolution acquisition was conventionally reconstructed using the DFT-SW procedure with low resolution coil sensitivity maps and the result was interpolated to the high resolution spatial grid by zero-filling the k-space data. The interpolated conventional reconstruction will be referred to as DFT-SW-ZF reconstruction. The quality of the reconstruction was estimated using the root mean square error (RMSE) with respect to the fully-encoded reconstruction.

The point spread function (PSF) or impulse response was computed by reconstructing the data from a source point, e.g. $s(\mathbf{r}_0) = \delta(\mathbf{r}_0)$ where δ is the Dirac function and \mathbf{r}_0 is the position of the source point. Spatial resolution will be de-

terminated using the full width at half maximum (FWHM) of the main lobe of the resulting PSF.

5.3.4 Simulations

Simulated 32-channel array data were created using the sensitivity maps estimated from a phantom acquisition. The phantom consisted of a uniform sphere with saline composition. Data was acquired with the 32-channel array coil using a gradient-echo sequence with a 128×128 spatial matrix and a field of view (FOV) of 256×256 mm², resulting in in-plane spatial resolution of 4.0 mm².

Structural MRI

Structural MRI data was simulated using a modified Shepp-Logan head phantom as object function. Multi-coil data was generated by multiplying the numerical phantom with the sensitivity maps and adding Gaussian noise corresponding to SNR=100.

Fig. 5.4 shows the reconstruction of the simulated phantom data. SURE-SENSE reconstruction reduced the spatial ringing and increased the spatial resolution of the conventional DFT reconstruction with k-space zero-filling. Very low average g-factors of 1.07 were obtained as expected from the pre-conditioning procedure.

Fig. 5.5 shows the PSF reconstruction for the data with reduced encoding factor $R = 4 \times 4$ (encoding matrix size: 32×32). The average FWHM of the PSF for DFT-SW-ZF reconstruction is 16.4 points while for SURE-SENSE is only 1.84 point which represents an average gain of 8.9 in spatial resolution.

Note that the average FWHM for SURE-SENSE is larger than the theoretical limit, which corresponds to one pixel width. This indicates that the method could not get the maximum spatial resolution given by the fully-encoded data and it is limited

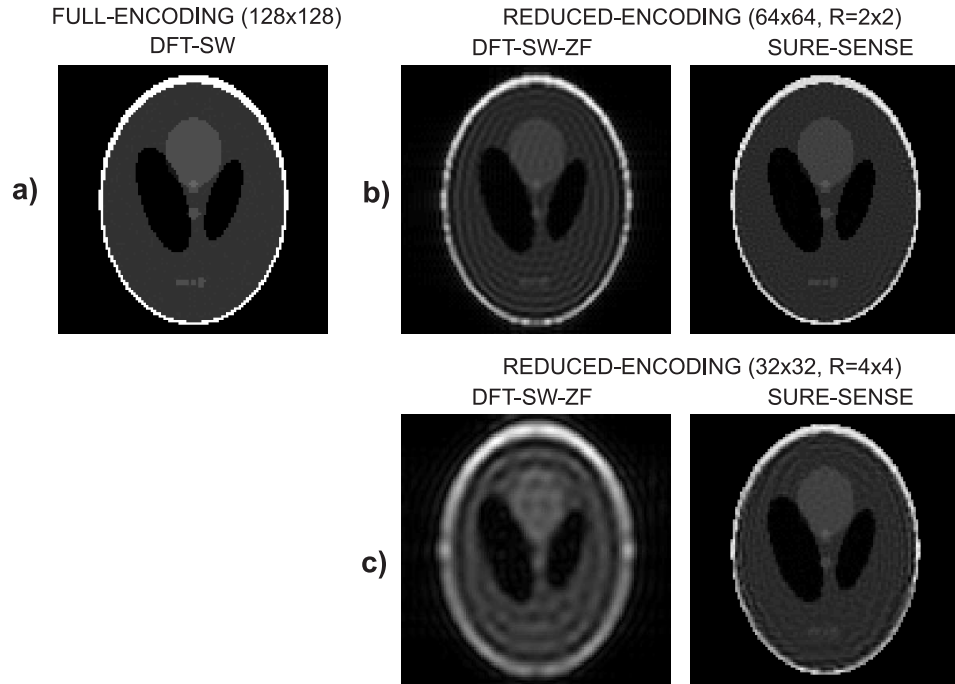


Figure 5.4: Simulated phantom reconstruction using the 32-channel array. a) Conventional DFT with sensitivity-weighting (DFT-SW) reconstruction of the fully-encoded data (encoding matrix size: 128×128 , $R=1$). DFT-SW with zero-filling (DFT-SW-ZF) and SURE-SENSE reconstruction of the data with reduced encoding: b) encoding matrix size: 64×64 , $R=4$, c) encoding matrix size: 32×32 , $R = 16$.

by the coil sensitivity variation within the low resolution voxel which determines the conditioning of the original encoding matrix.

The spatial resolution of SURE-SENSE reconstruction is spatially-varying as expected and provides better defined PSF in regions with stronger spatial variation of the coil sensitivity maps.

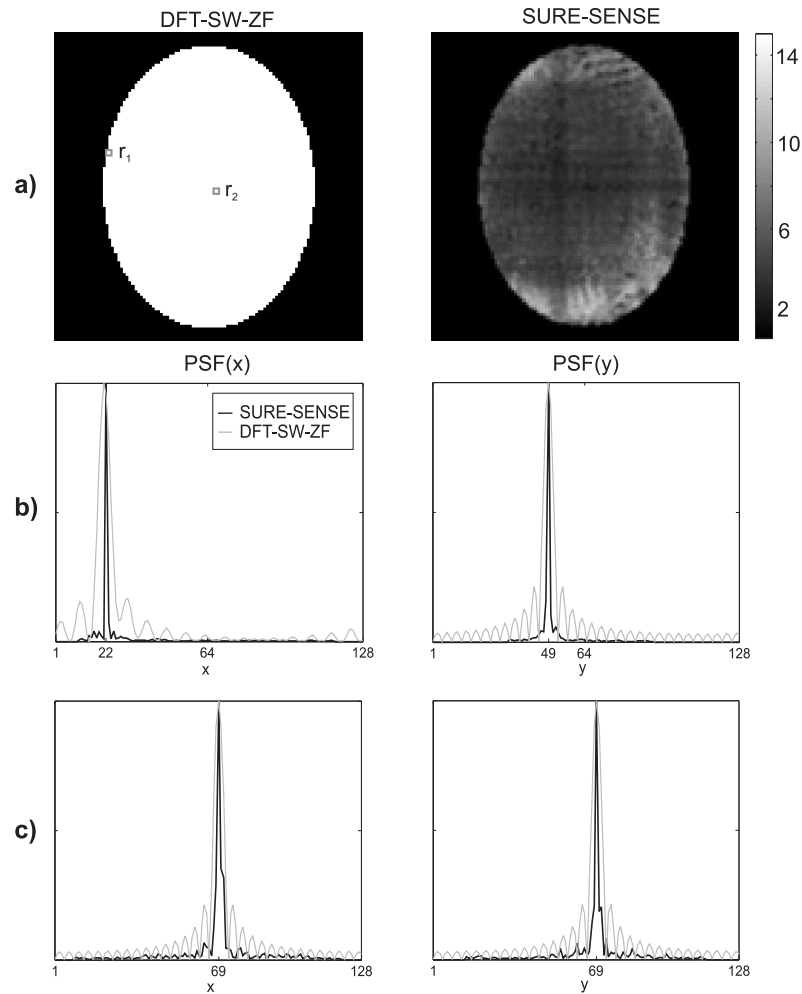


Figure 5.5: Point spread function (PSF) reconstruction of the simulated phantom data with reduced encoding (encoding matrix size: 32×32 , reconstruction matrix size: 128×128) using DFT-SW-ZF and SURE-SENSE: a) full-width at half-maximum (FWHM) images, b) PSF in a voxel close to the periphery (r_1), and c) PSF of a central voxel (r_2).

Comparison to standard SENSE

Reconstruction with low target spatial resolution was simulated to compare the performance of standard SENSE and SURE-SENSE at the low spatial resolution regime.

Fully-encoded low resolution data was obtained from the central 64×64 k-space matrix. Coil sensitivity maps were estimated from the fully-encoded low resolution data. Sub-sampled low resolution data was obtained by decimating the fully-encoded low resolution data along two-dimensions by a factor $R = 4 \times 4$. Standard SENSE reconstruction was applied to the sub-sampled low resolution data. Truncated low resolution data was obtained from the central 16×16 k-space matrix, which represent the same acceleration factor of SENSE. Superresolution SENSE reconstruction was applied to the truncated low resolution data. The reconstruction results were interpolated to a 256×256 matrix by using zero-filling in k-space.

Standard SENSE reconstruction presented residual aliasing artifacts due to coil sensitivity variation within the low spatial resolution target voxel (Fig. 5.6). This effect is particularly evident at the periphery where sensitivity variation is stronger. For example, the PSF of the point close to the periphery shows poor suppression of the aliasing peaks. The RMSE for standard SENSE was 13.7% and for SURE-SENSE was 4.2%. Superresolution SENSE is free of residual aliasing artifacts since the reconstruction paradigm is different. The accelerated data for SURE-SENSE presents a PSF with broad main lobe and significant side lobes. The reconstruction improves the PSF using sensitivity maps that vary within the lobes of the PSF to reduce the width of the main lobe and the power of the side lobes. Since the extent of the side lobes is larger than the extent of the main lobe and the variation of the coil sensitivities is higher for larger distances, side-lobe suppression presented better performance than reduction of the main-lobe width.

5.3.5 Experiments

Human brain data were acquired using a gradient-echo sequence with a 256×256 spatial matrix and a FOV of 256×256 mm², resulting in in-plane spatial resolution

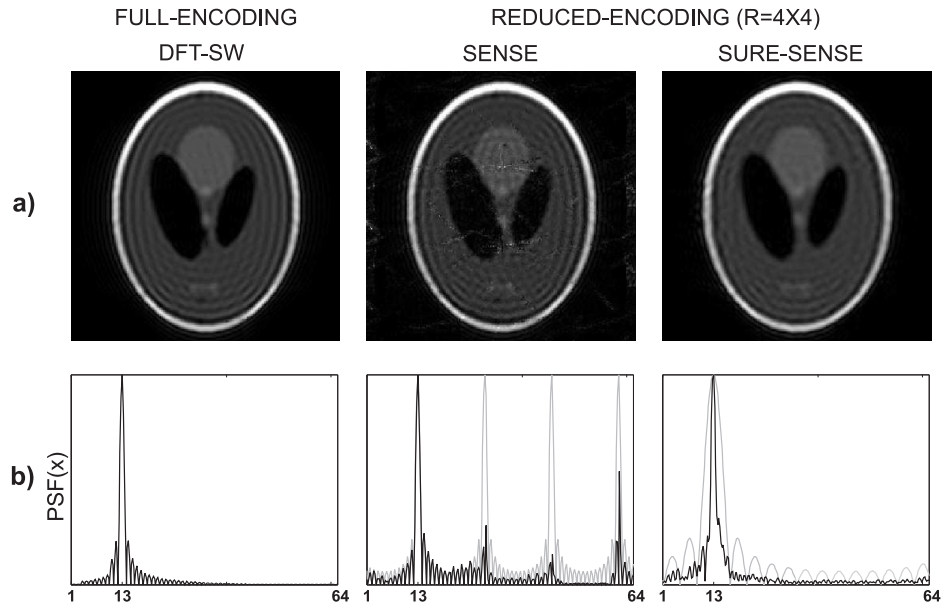


Figure 5.6: Comparison of standard SENSE and SURE-SENSE reconstruction at low spatial resolution using the 32-channel array. The reconstruction of the fully encoded data is shown for comparison purposes. a) Absolute images. b) Point spread function along the x dimension. The PSF of conventional DFT reconstruction of the accelerated data are shown in gray lines: aliasing peaks for SENSE sub-sampling and broadening with increased side lobes for SURE-SENSE truncated sampling.

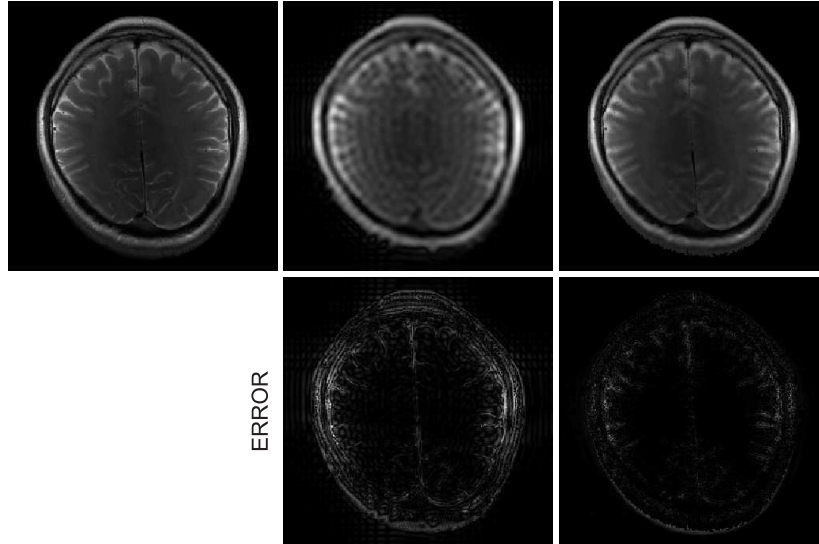
of 1 mm^2 . Two acquisitions were performed on different subjects using the 32- and 96-channel arrays respectively. Fig. 5.7.a shows the reconstruction using the 32-channel array with a high acceleration factor of 28.4. The RMSE with respect to the fully-encoded reconstruction for conventional DFT reconstruction was 35.5% and for SURE-SENSE was only 9.6%. Fig. 5.7.b shows the reconstruction of a different human brain MRI data using the 96-channel array with a higher acceleration factor of 64. The RMSE with respect to the fully-encoded reconstruction for conventional DFT reconstruction was 71.1% and for SURE-SENSE was only 10.9%. Note that the reconstruction using the 96-channel array is recovering more spatial features as suggested by the error image, which is due to the stronger variation of the coil sensitivities.

a) 32-CHANNEL ARRAY

FULL-ENCODING (256x256)
DFT-SW

REDUCED-ENCODING (48x48, R=5.3x5.3)
DFT-SW-ZF

SURE-SENSE



b) 96-CHANNEL ARRAY

FULL-ENCODING (256x256)
DFT-SW

REDUCED-ENCODING (32x32, R=8x8)
DFT-SW-ZF

SURE-SENSE

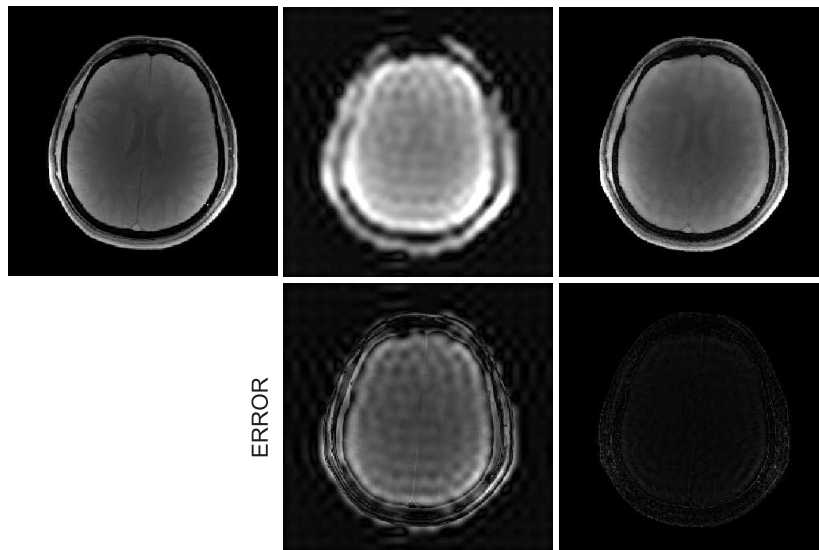


Figure 5.7: Human brain MRI reconstruction for a) 32-channel array and b) 96-channel array.

5.4 Discussion

In this Chapter, a novel reconstruction technique is proposed for parallel MRI using large scale array coils with strongly varying coil sensitivity maps. In analogy to superresolution image reconstruction from picture and video processing, where multiple low resolution images with sub-pixel differences are combined, parallel MRI reconstruction was formulated as a superresolution problem. Acceleration is performed by acquiring only the central region of k-space instead of increasing the sampling distance over the complete k-space matrix, which represents the low spatial resolution representation of the object being imaged. Single coil sensitivity variation and different sensitivity profiles within the acquired low resolution pixels are employed to perform intra-pixel reconstruction.

The proposed method offers an alternative approach to standard parallel MRI methods for the same acquisition time which is particularly suitable to large-N array coils that present much stronger spatial variation of the coil sensitivity profiles than the commercially available receiver arrays with 8 and 12 elements. While strong variation in the coil sensitivity maps represents a cause of artifacts in standard SENSE or GRAPPA parallel MRI methods due to the intra-pixel sensitivity variation or equivalently increased k-space extent of the coil sensitivity maps [66], SURE-SENSE is taking advantage of the stronger sensitivity variation to perform intra-pixel reconstruction with improved performance. Moreover, the reconstruction error for standard SENSE is distributed in bands across the entire image while for SURE-SENSE is limited to the extent of the low resolution PSF. This reflects the difference in k-space sampling with the two techniques: localized errors in k-space when reconstructing missing k-space samples in SENSE lead to distributed artifacts in the spatial-domain, whereas errors in reconstructing extrapolated k-space in SURE-SENSE lead to localized errors in the reconstructed image.

SURE-SENSE is particularly advantageous for application of parallel imaging to intrinsically low spatial resolution data such as spectroscopic imaging, since it does not present residual aliasing artifacts as in standard SENSE reconstruction for cases where the coil sensitivities are varying within the image voxel.

The reconstruction of accelerated data in parallel MRI comes at the expense of SNR loss dictated by the reduced number of encoding points and noise amplification in the reconstruction due to ill-conditioning of the encoding matrix (g-factor). Pre-conditioning reduces the g-factor for SURE-SENSE reconstruction close to one at the expense of slight spatial resolution reduction in the reconstructed image due to the attenuation of small singular values, which are related to high spatial frequencies. As we have shown in our results, this tradeoff is quite acceptable when the data is acquired with large-scale array coils that provide strongly modulated coil sensitivity profiles and high SNR. Alternatively, regularization methods using prior information about the final image could be used to improve the tradeoff between SNR and spatial resolution [48].

The maximum gain in spatial resolution is given by the degree of variation of the coil sensitivities within the image voxel. Stronger variations in the spatial domain correspond to a larger extent in k-space. We expect that the performance of SURE-SENSE reconstruction for human brain imaging will improve with the number of receiver coils using array geometries similar to the soccer-ball, as we have shown in the results for the 96-channel array. In central regions of the brain further away from the top of the soccer-ball shaped array the coil sensitivity profiles are varying less strongly, which will limit resolution enhancement. We are in the process of implementing the technique using similar arrays at 7 Tesla which will provide higher sensitivity and stronger spatial modulation of the sensitivity functions [27].

5.5 Summary

The Superresolution SENSE method introduced in this Chapter represents a novel parallel imaging method that compares favorably the performance of standard SENSE reconstruction for low spatial resolution imaging and large-scale RF arrays with strong spatial sensitivity variation of the coil profiles. However, superresolution SENSE is not limited to low resolution MRI as we have shown and future work will characterize the optimal operating regimes of superresolution SENSE. The technique is particularly applicable to intrinsically low spatial resolution modalities such as spectroscopic and functional imaging and provides flexible tradeoff between spatial and temporal resolution for accelerating scans in clinical studies.

Chapter 6

PEPSI at High-Field: SNR and Spectral Resolution Improvements

⁴ This chapter analyzes quantitatively the advantages of using high magnetic field strength (B_0) in Proton Echo Planar Spectroscopic Imaging (PEPSI). Theoretical expectations for MRS show a linear increase in SNR and spectral resolution with respect to B_0 . However, no experimental validation was performed for echo-planar MRSI. SNR per unit volume and unit time and spectral line width of the main metabolites N-Acetyl-Aspartate (NAA), Creatine (Cr) and Choline (Cho) were estimated from *in vivo* PEPSI acquisitions at 1.5, 3, 4 and 7 Tesla on scanners sharing a similar software and hardware platform. Data were corrected for relaxation differences and fitted to a parametric model adapted to each B_0 .

⁴The work in this chapter was published as: R. Otazo, B. Mueller, K. Ugurbil, L. Wald and S. Posse. “Signal-to-Noise Ratio and Spectral Line Width Improvements between 1.5 and 7 Tesla in Proton-Echo-Planar-Spectroscopic-Imaging (PEPSI)”. *Magn Reson Med* 2006; 56(6):1200-1210.

Presented in part at the 13th Annual Meeting of the International Society of Magnetic Resonance in Medicine (ISMRM), Miami, FL, USA, 2005, pp. 2521.

6.1 Introduction

The main advantage of using high field strength (B_0) in all magnetic resonance experiments is a significant improvement in signal-to-noise ratio (SNR). For in vivo applications using the ^1H nucleus, a linear gain of SNR with respect to B_0 was theoretically predicted provided that relaxation times do not change, experimental parameters are the same, sample losses dominate the noise source and RF penetration effects are not significant [69, 70, 71]. For high fields, SNR becomes rather complex due to B_1 field inhomogeneity and it has to be treated as a function of the position, but on average the theoretical limit remains the same [72]. Experimentally, for imaging it was found that SNR increases at least linearly with the field strength in a range from 0.5 Tesla to 7 Tesla [73, 74]. For single voxel spectroscopy gains less than linear (23-28%) were found in 3 T vs. 1.5 T experiments [75]. For conventional Chemical Shift Imaging (CSI) 23-46% gains were found in 3 T vs. 1.5 T comparisons [76]. Many factors that may reduce the expected SNR improvement at higher field have been reported such as longer T_1 relaxation times that lead to saturation related signal losses at short TR [73], line broadening due to magnetic susceptibility effects [75, 76], shorter T_2 at higher fields [77], limited RF power and limitations in the design of homogeneous RF coils [78]. MRS at high-field benefits from improved spectral resolution due to increased chemical shift dispersion and reduced higher-order coupling effects [73, 78]. Using short echo-time single voxel spectroscopy coupled metabolites in the human brain (like glutamate and glutamine) were more easily resolved at 4T compared to 1.5T [79]. Additionally, the spectral linewidth (LW) in ppm decreased. Increased SNR and spectral resolution in MRS translate to improved metabolite quantification precision or may be traded for a higher spatial resolution which still maintains adequate SNR for reliable quantification. Comparisons of quantification precision across field strengths have shown a considerable decrease in the Cramer-Rao lower bound with increasing B_0 for all the metabolites [80].

An experimental comparison and analysis of sensitivity and spectral resolution as a function of the magnetic field strength has not been reported yet for fast spectroscopic imaging techniques. The aim of this work was to study the advantages of increasing the magnetic field strength in Proton-Echo-Planar-Spectroscopic-Imaging (PEPSI) where time-varying gradients are used to encode simultaneously spectral-spatial information [29]. We present a comparison of SNR and spectral line width of the main singlet metabolites (N-Acetyl-Aspartate (NAA), Creatine (Cr) and Choline (Cho)) at 1.5, 3, 4 and 7 Tesla in a supra-ventricular para-axial slice location using PEPSI with short echo times in scanners sharing same hardware and software platforms with circularly polarized (CP) head coil and 8-channel phased-array (PA) head coils to quantitatively evaluate gains across field strengths. Spectral fitting using metabolite and macromolecule basis sets for each magnetic field strength is employed to estimate the SNR and spectral linewidth of NAA, Cr and Cho. The effects of gradient configuration and sampling scheme on SNR are analyzed by evaluating the noise characteristics as a function of the degree of ramp sampling. The dependence of spectral line width on transverse relaxation time T₂, line broadening due to microscopic susceptibility and diffusion effects on local susceptibility gradients is analyzed across field strengths.

6.2 Methods

6.2.1 Measurements

Scanners with clinical interface sharing the same Siemens Syngo hardware and software platform were employed: Siemens Sonata Maestro 1.5 Tesla, Siemens Trio 3 Tesla, Bruker MedSpec 4 Tesla and Siemens 7 Tesla scanner. Trio and MedSpec scanners were equipped with Sonata gradients (maximum amplitude: 40 mT/m,

slew rate: 200 mT/m/ms). The 7 Tesla scanner was equipped with a head gradient insert (80 mT/m, 600 mT/m/ms). All scanners were equipped with CP head coils and 8-channel head PA coils. The 8-channel array coils at 1.5 and 3 Tesla were receive-only in circular configuration. Transmission was performed with a quadrature body RF coil. At 4 and 7 Tesla the PA head coil consisted of a quadrature birdcage head coil for transmission and an integrated circular 8-channel surface coil array for reception.

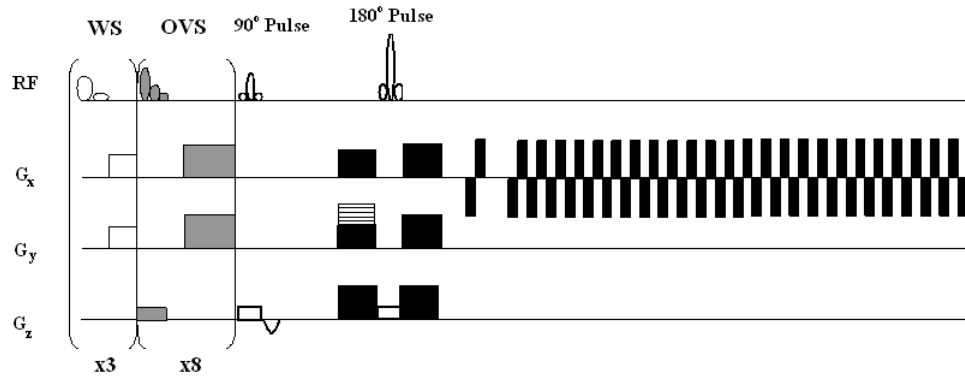


Figure 6.1: PEPSI pulse sequence with water suppression (WS), outer volume suppression (OVS), spin echo excitation and echo-planar readout. Data are collected in blocks during each of the cyclically inverted readout gradients (G_r).

Measurements with the PEPSI technique were performed in a supraventricular para-axial slice location on 24 healthy volunteers (18 males and six females, age range: 20-35 years, mean age: 26 years). Twenty subjects were scanned with the CP coil, and four were scanned with the PA coil at 1.5T, 3T, 4T, and 7T. The measurement parameters are listed in Table 1. Spatial and spectral encoding was performed with the PEPSI method [29] using a train of 1024 alternating positive and negative readout gradients along the x-direction (Fig. 6.1). Data were collected with twofold oversampling for each readout gradient separately using a ramp sampling delay of 8 μ s to limit chemical shift artifacts. The gradient waveform was tuned for

B_0 [T]	Coil	SW[Hz]	T_E [ms]	FOV[mm]	Δz [mm]	T_A [min]	V_r [cc]
1.5	CP(3)	780	30	320	15	8:32	1.5
	CP(3)	1080	15	260	15	8:32	1
	PA(1)	1080	15	260	15	8:32	1
3	CP(6)	1080	15	260	15	8:32	1
	PA(1)	1080	15	260	15	8:32	1
4	CP(6)	1080	15	320	10	8:32	1
	PA(1)	1080	15	320	10	8:32	1
7	CP(1)	1380	15	320	10	1:04	1
	CP(1)	1380	15	320	10	8:32	1
	PA(1)	1080	15	320	10	8:32	1

Table 6.1: Measurement parameters for PEPSI acquisitions. B_0 : magnetic field strength, SW: spectral width, T_E : echo time, FOV: field of view, Δz : slice thickness, T_A : acquisition time, V_r : voxel volume.

each of the scanners to encompass the entire spectral range from 0 to 4.7 ppm (Table 6.1). Phase encoding was performed along the y-direction. Data were collected at TR: 2 s using a 32×32 spatial matrix. Complete eight-slice outer volume suppression (OVS) was applied along the perimeter of the brain. The complete data acquisition included water-suppressed (WS) and non-WS (NWS) scans. Online regridding was implemented as a Functor in the ICE reconstruction software environment (Siemens Medical Solutions, Erlangen, Germany) to correct for ramp sampling distortion of the k-space trajectory. After regridding, the twofold oversampling was removed.

Four additional measurements were performed at 1.5 and 4 Tesla using conventional phase-encoded CSI (two measurements at each field-strength on the same subject). Water-suppressed and non-water suppressed reference data sets were collected with conventional PRESS CSI sequence provided by the manufacturer using a CP head coil. The following parameters were the same for all the acquisitions: TR: 2 s, TE: 30 ms, 16×16 spatial matrix, rectangular sampling, voxel volume: 4 cc, scan time: 8.5 min.

6.2.2 Reconstruction

Reconstruction was performed using an automated data processing routine (Fig. 6.2) developed in IDL. Odd and even echoes were sorted into separate arrays performing time reversal and phase inversion of odd echo data relative to even echo data, producing four separate $k_x - k_y - t$ data arrays with CSI format (WS-ODD, WS-EVEN, NWS-ODD, NWS-EVEN). A sine bell k-space filter is then applied to reduce contamination due to ringing in the Fourier reconstruction.

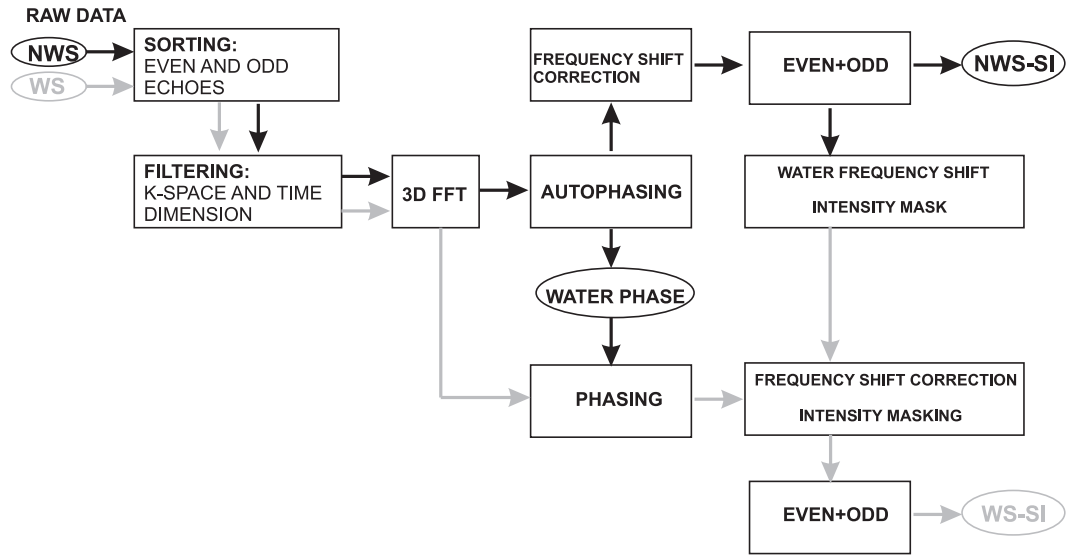


Figure 6.2: Single coil reconstruction flow chart for PEPSI data. Odd and even echoes are separately processed and added to the end after phasing and frequency shift corrections. The water reference scan (NWS) is used for phase correction and frequency referencing.

Two water-suppressed data sets were created for comparison: (i) without a time-domain filter; and (ii) with an exponential time-domain filter $e^{-\alpha t}$ (matched-filter) to maximize the SNR [45]. For the parameter of the filter (α), we used the intrinsic linewidth of the spectral line of interest adjusted to each magnetic field strength. Assuming that the intrinsic linewidth of NAA in Hz increases linearly with the field

strength (as it will be shown here - see Results section), we used 2 Hz line broadening for 1.5 Tesla, 4 Hz for 3 Tesla, 6 Hz for 4 Tesla and 10 Hz for 7 Tesla.

Each array is then subjected to 3-D Fast Fourier Transform (FFT) reconstruction to produce four distinct x - y - f arrays. The reconstructed spectra were interpolated to 2048 points using zero-filling in the time-domain. Zero order phases of the water signals are automatically determined in the NWS data and these phase corrections are applied to the corresponding WS data arrays. Spectral frequency assignment in the WS array is made using the NWS data and assuming the largest signal in the NWS data represents water. Odd and even data are then added to form NWS and WS arrays and reconstructed to obtain NWS and WS spectroscopic images (NWS-SI and WS-SI). Eddy current correction using Klose's method [81] was applied to the reconstructed spectroscopic images using the phase of NWS-SI to remove residual line shape distortion and possible water sidebands. Removal of peripheral lipid contamination using k-space extrapolation and the Papoulis-Gerchberg (PG) algorithm [82] was applied only to 7 Tesla data. The lipid threshold was selected manually to create a mask that identifies peripheral lipid regions.

For acquisitions with the phased-array coil, sensitivity-weighted combination was performed [83]. The coil sensitivity maps are estimated from spectral water images, i.e. integration along the spectral axis of the reconstructed NWS data (NWS-SI). The signal from each array coil element was reconstructed separately using the method described previously (Fig. 6.2). The combined spectroscopic image was given by:

$$S(x, y, f) = \frac{\sum_{l=1}^{N_c} S_l(x, y, f)C_l(x, y)}{\sum_{l=1}^{N_c} |C_l(x, y)|^2}, \quad (6.1)$$

where N_c is the number of coils. The procedure was applied to WS and NWS data sets.

6.2.3 Spectral Fitting

Averaged spectra in selected ROIs (Fig. 6.3) were obtained by:

$$\bar{S}(f) = \frac{1}{N_R} \sum_{(x,y) \in R} S(x, y, f), \quad (6.2)$$

where N_R is the number of voxels in the ROI. Two ROIs were defined: a rectangular brain region for comparisons using the CP coil (R1); and a ring centered within the FOV with a variable radius for the array coil (R2), which allowed obtaining a spatial distribution of the SNR in experiments with the PA coil.

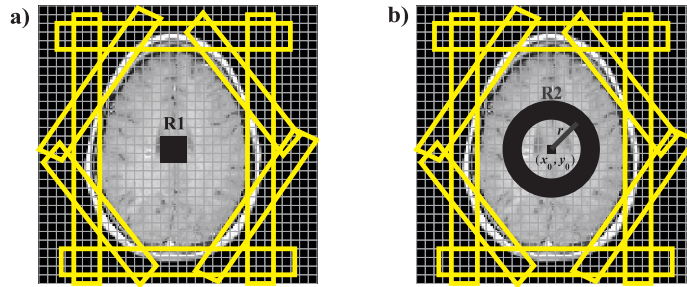


Figure 6.3: Regions of interest to compute the averaged spectrum. a) R_1 : 3×3 rectangular ROI in the center of the FOV for the CP coil. b) R_2 : ring-shaped ROI centered within the FOV for the PA coil. r is the Euclidean distance from the center. 9 voxels are chosen from R_2 to match the noise power in R_1 . The positions of the outer volume saturation bands are shown as rectangles.

The water-suppressed averaged spectrum was quantified using the jMRUI package [84]. The residual water peak was filtered with the Hankel-Lanczos singular value decomposition (HLSVD) algorithm [85]. The QUEST method (QUantification based on quantum ESTimation) [86] was used to estimate the metabolite signals from the averaged spectrum. The basis set was simulated with NMR-SCOPE [87] using the spin Hamiltonian parameters (number of spins, chemical shifts and J-couplings) given by Govindaraju et al. [88] and the spin-echo excitation module of the PEPSI

sequence for each magnetic field strength and echo time. The basis sets included 13 metabolite signals: Aspartate (Asp), Choline (Cho), Creatine (Cr), -Amino Butyric Acid (GABA), Glucose (Glc), Glutamate (Glu), Glutamine (Gln), Lactate (Lac), myo-Inositol (mI), N-Acetyl-Aspartate (NAA), Phospho-Creatine (PCr), Phospho-Choline (PCho) and Taurine (Tau).

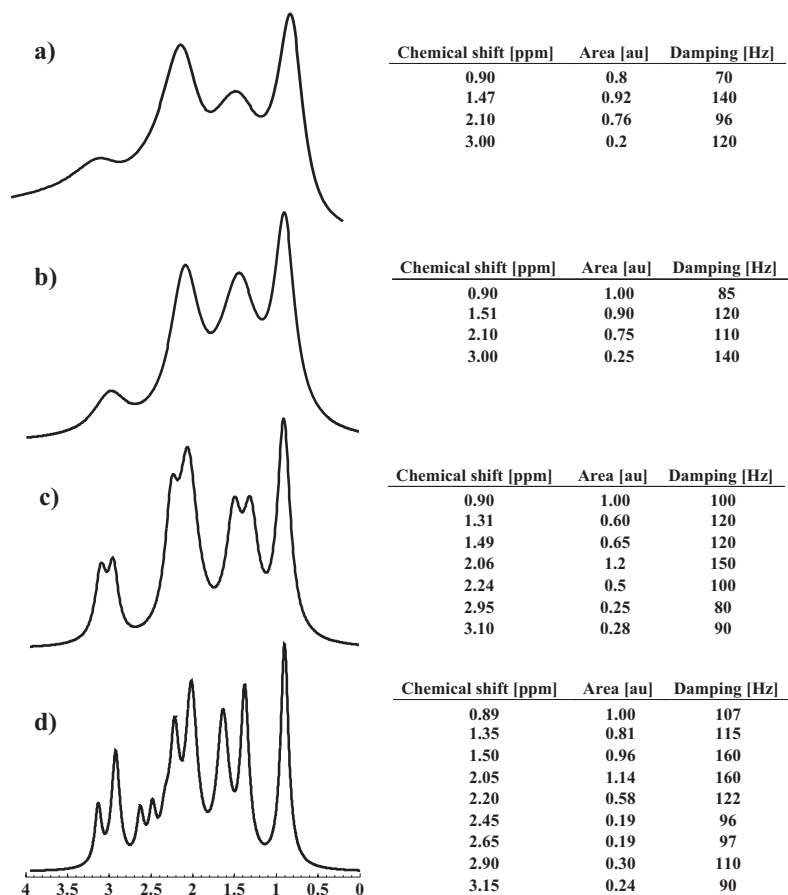


Figure 6.4: Simulated macromolecular spectra (left) and parameterization of the simulation (right) by fitting metabolite-nulled spectra with a combination of Lorentzian lines for: a) 1.5 Tesla, b) 3 Tesla, c) 4 Tesla and d) 7 Tesla.

Macromolecule (MM) information was added to the basis set by parameterization of metabolite-nulled in vivo spectra [89] for each magnetic field strength. For

1.5 and 4 Tesla, metabolite-nulled PEPSI spectra were measured using a modified pulse sequence with a slice selective adiabatic inversion pulse. Spectra were averaged across the FOV to improve SNR. For 3 and 7 Tesla, metabolite-nulled spectra of 12 healthy volunteers using PRESS and STEAM respectively were averaged. Parameterization of MM spectra was performed in jMRUI with the AMARES algorithm using Lorentzian lines. Fig. 6.4 shows the macromolecule model at each magnetic field strength and the parameters for the Lorentzian model.

6.2.4 Comparisons across field strengths

SNR and spectral LW of NAA, Cr and Cho were computed using the averaged spectrum $\bar{S}(f)$ from a selected region of interest R_i for the two types of coils used (Fig. 6.3).

SNR comparisons

SNR per unit volume and unit time was used to compare the sensitivity across magnetic field strengths. Since the SNR in MRI is proportional to the voxel volume and the square root of the scan time [90], the SNR per unit volume and unit time of the metabolite m_j is defined by:

$$SNR(m_j) = \frac{SNR_{meas}(m_j)}{V_r \sqrt{T_a}}, \quad (6.3)$$

where $SNR_{meas}(m_j)$ is the estimated SNR from the measurement. V_r is the voxel volume (cc: cubic centimeter) and T_a is the total acquisition time (min). Two types of SNR were estimated from the averaged spectrum using the results of spectral fitting:

- (i) Metabolite amplitude to noise (SNR-peak):

$$SNR_{peak}(m_j) = \frac{peak(m_j)}{\bar{\sigma}}, \quad (6.4)$$

where $peak(m_j)$ is the peak amplitude of the fitted metabolite m_j , and

(ii) Metabolite area (concentration) to noise (SNR-area):

$$SNR_{area}(m_j) = \frac{area(m_j)}{\bar{\sigma}}, \quad (6.5)$$

where $area(m_j)$ is the area of the fitted metabolite m_j .

The noise ($\bar{\sigma}$) is the standard deviation of $\bar{S}(f)$ in a spectral region without signal (maximum-length window with minimum-variance). To estimate the latter quantity the averaged spectrum is divided into N_σ regions. For each k -th region, the standard deviation is computed (σ_k). The minimum σ_k is taken for each division and the minimum σ_k of the divisions is used to get the final $\bar{\sigma}$. We used $N_\sigma = 32, 64, 128,$ and 256 .

To correct for differences in T1 related signal saturation and T2 related signal decay at different field strengths, SNR was multiplied by the following correction factor [45]:

$$CF(T_1, T_2, T_R, T_E) = \frac{1}{(1 - \exp(-T_R/T_1)) \exp(-T_E/T_2)}. \quad (6.6)$$

Literature values for T_1 and T_2 of NAA, Cr and Cho were used (Table 6.2).

Spectral line width comparisons

For spectral line width comparisons, the intrinsic line width of NAA, Cr and Cho were measured. The line width was estimated using the full-width at half-maximum (FWHM) of the fitted metabolite signal from the reconstructed WS data without the matched-filter.

To estimate the contribution of the transverse relaxation time T_2 , magnetic susceptibility and diffusion in local susceptibility related gradients to the line width LW,

B_0 [T]	T_1 [s]			T_2 [ms]		
	NAA	Cr	Cho	NAA	Cr	Cho
1.5	1.27 [91]	1.24 [91]	1.15 [91]	450 [78]	240 [78]	330 [78]
3	1.47 [91]	1.33 [91]	1.25 [91]	280 [92]	178 [92]	222 [92]
4	1.63 [77]	1.72 [77]	1.29 [77]	230 [77]	141 [77]	179 [77]
7	1.73 *	1.82 **	1.33 **	141 [93]	109 [93]	109 [93]

* I. Tkac, Personal communication.

**T1 values for Cr and Cho at 7 Tesla were extrapolated with a power function using the values at 1.5, 3 and 4 Tesla.

Table 6.2: Literature values of T1 and T2 for NAA, Cr and Cho at different magnetic field strengths.

the following model was used:

$$LW = \frac{1}{\pi T_2} + \Delta f_{macro} + \Delta f_{micro} + \Delta f_{diff}, \quad (6.7)$$

where Δf_{macro} and Δf_{micro} are the line broadening components due to macroscopic and microscopic susceptibility effects respectively and Δf_{diff} is the line broadening component due to diffusion in local susceptibility related gradients. Assuming that macroscopic susceptibility is highly reduced by the shimming procedure, i.e. line width is independent of voxel size, LW is modeled by:

$$LW = \frac{1}{\pi T_2} + \frac{1}{\pi T_{2,micro}} + \frac{1}{\pi T_{2,diff}} = \frac{1}{\pi T_2} + \frac{\gamma G_s}{\pi} + \frac{\gamma^2 G_s^2 T_E^2 D}{12\pi}, \quad (6.8)$$

where γ is the gyromagnetic ratio, G_s is the effective local susceptibility related gradient, and D is the diffusion coefficient [4]. Modeling the local susceptibility related gradient proportional to B_0 , i.e. $G_s = \alpha B_0$, line broadening (LB) across field strengths was fitted with:

$$LB = LW - \frac{1}{\pi T_2} = \alpha_1 B_0 + \alpha_2 B_0^2, \quad (6.9)$$

where $\alpha_1 B_0$ and $\alpha_2 B_0^2$ represent line broadening due to microscopic susceptibility and diffusion respectively. Literature values were used for T_2 of NAA, Cr and Cho (Table 6.2).

6.3 Results

Short echo time spectra with well defined resonances were obtained with the PEPSI method across field strengths. Spectroscopic images at 1.5, 3 and 4 Tesla were reconstructed without lipid removal by post-processing. Lipid removal using k-space extrapolation [82] was only employed at 7 Tesla to control increased lipid contamination due to B_1 -inhomogeneity.

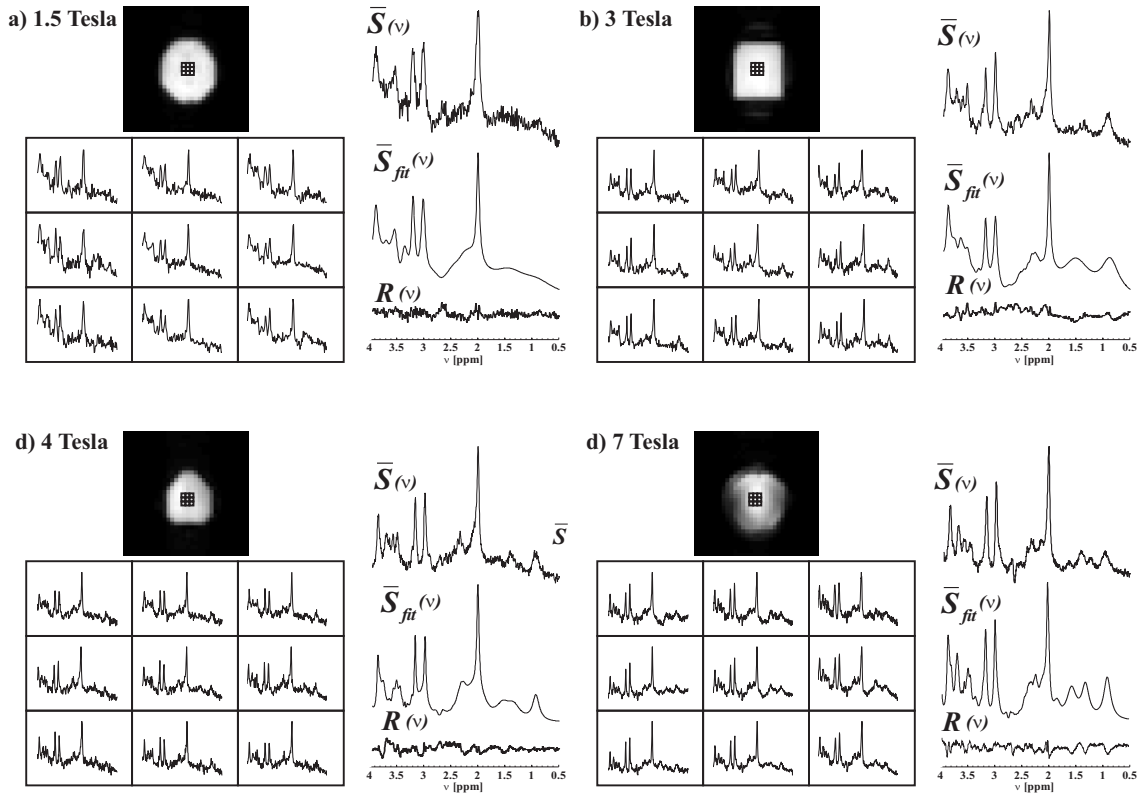


Figure 6.5: Water-suppressed PEPSI spectra using the CP coil for a) 1.5 T, b) 3 T, c) 4 T, d) 7T (voxel size: 1 cc, and total acquisition time: 8.5 min). The spectral water image, spectral array from the region R_1 , corresponding averaged-spectrum $\bar{S}(\nu)$, fitted averaged-spectrum $\bar{S}_{fit}(\nu)$ and fitting residual $R(\nu)$ are shown for each magnetic field strength.

Line shape distortion due to eddy currents was very small and removed by eddy current correction. Spectral arrays and corresponding averaged spectrum using the CP coil for a region of interest R_1 showed a considerable gain in spectral resolution at higher fields, e.g. J-coupled metabolites such as Glutamate (Glu) and Inositol (Ino) are clearly separated at 4 and 7 Tesla while Glu and NAA overlapped at 1.5 T (Fig. 6.5). The inclusion of parametric models for macromolecules at each magnetic field strength in the basis sets provided improved spectral fitting results, especially at 1.5 Tesla, reducing possible over-estimation of the metabolite peak heights and areas at that field strength due to overlapping macromolecule resonances. For example, omitting the macromolecule resonance located around 2.10 ppm produce erroneous results in the estimation of NAA.

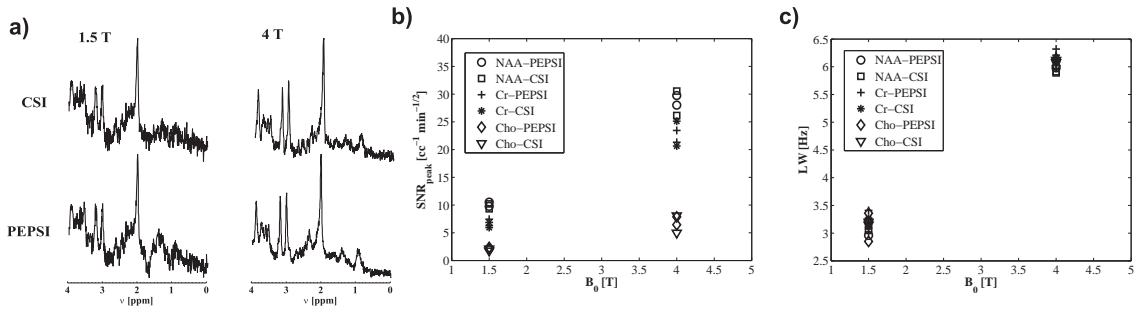


Figure 6.6: Comparison of PEPSI and PRESS-CSI spectra at 1.5 and 4 Tesla (CP coil, same subject at each B_0 , total acquisition time: 8.5 min). a) Averaged spectrum. b) SNR-peak for NAA, Cr and Cho as a function of B_0 for four measurements (two measurements at each B_0). c) Line width for NAA, Cr and Cho as a function of B_0 .

PEPSI and PRESS CSI presented spectra with similar characteristics (Fig. 6.6.a) in 4 experiments at 1.5 and 4 Tesla (two experiments on the same subject at each B_0). SNR and linewidth of NAA, Cr and Cho for PEPSI and PRESS CSI acquisitions are listed on Table 3. A quantitative comparison was performed for the data sets at each B_0 to compute the ratio in % of SNR-peak: $|\text{SNR}(\text{PEPSI}) - \text{SNR}(\text{CSI})| / \text{SNR}(\text{CSI})$ and line width: $|\text{LW}(\text{PEPSI}) - \text{LW}(\text{CSI})| / \text{LW}(\text{CSI})$ between the two pulse sequences.

B_0 [T]		SNR-peak [cc ⁻¹ min ^{-1/2}]			LW [Hz]		
		NAA	Cr	Cho	NAA	Cr	Cho
1.5	PEPSI	9.77	6.31	2.01	3.22	3.41	3.36
	PRESS-CSI	9.33	5.94	1.76	3.05	3.19	3.20
1.5	PEPSI	10.52	7.45	2.37	2.96	3.02	2.85
	PRESS-CSI	10.21	6.86	2.12	3.13	3.27	3.15
4	PEPSI	28.02	21.33	6.45	6.11	6.21	6.15
	PRESS-CSI	26.15	20.65	4.98	5.89	6.08	6.08
4	PEPSI	29.76	23.45	7.87	5.98	6.32	6.02
	PRESS-CSI	30.56	25.12	8.10	5.91	6.12	6.12

Table 6.3: SNR-peak (with T_1 - T_2 relaxation correction and matched-filtering) and LW comparison for NAA, Cr and Cho of PEPSI and PRESS-CSI at 1.5 and 4 Tesla for four different subjects in experiments with the CP coil.

SNR-peak ratios were: 3.8% for NAA, 7.1% for Cr and 12.4 for Cho at 1.5 Tesla; 2.2% for NAA, 5.2% for Cr and 7.1% for Cho at 4 Tesla. LW ratios were: 4.9% for NAA, 7.6% for Cr and 7.8 for Cho at 1.5 Tesla; 2.9% for NAA, 2.7% for Cr and 1.4% for Cho at 4 Tesla. PEPSI and PRESS-CSI showed similar SNR-peak and linewidth at 4 Tesla. At 1.5 Tesla differences were slightly higher, which are due in part to spectral fitting performance.

SNR-peak and SNR-area of NAA, Cr and Cho increased with magnetic field strength (Fig. 6.7). NAA presented a larger SNR in comparison to Cr and Cho due to its larger concentration. A power fit $y = ax^b$, shows that an increasing linear function describes well the SNR dependence with B_0 (the exponent b is close to 1). To describe the goodness of the fit we used: R-square, square of the correlation between the data values and the fit values (R^2). There was a considerable SNR gain using the matched-filter compared to the data without the filter. The use of an exponential matched-filter, with a line broadening parameter that increases linearly with the field strength, improved the SNR especially at higher fields (7 Tesla), where T_2 is shorter, obtaining a more linear dependence of the SNR on the field strength.

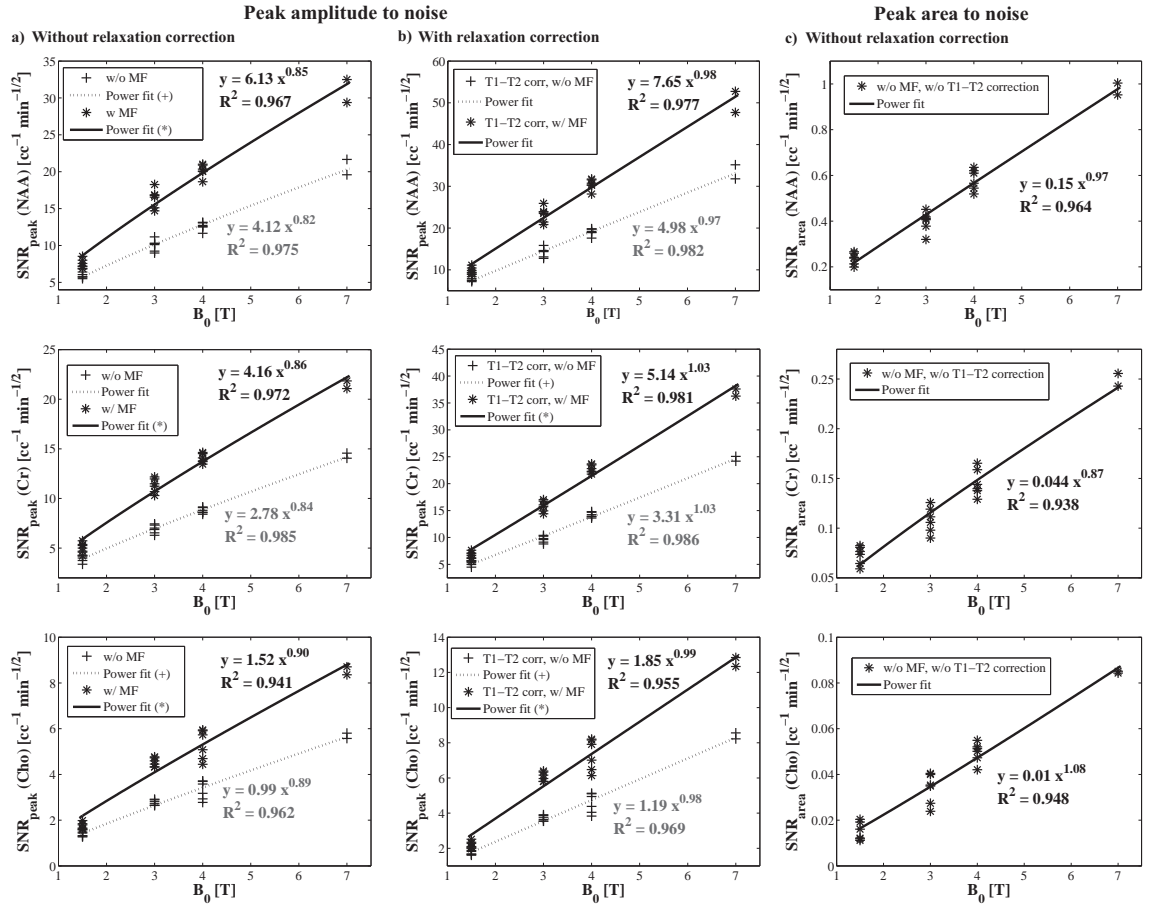


Figure 6.7: SNR-peak (peak-amplitude to noise) and SNR-area (concentration to noise) as a function of B_0 for NAA, Cho and Cr in measurements using the CP coil. a) SNR-peak with and without a matched-filter (MF) that is adjusted to the measured signal decay as a function of B_0 b) SNR-peak with relaxation correction. c) SNR-area for the reconstructed data without the matched-filter. SNR-peak with relaxation correction and SNR-area increase linearly with B_0 .

When additionally accounting for different T_1 and T_2 related saturation across field strengths, a gain in SNR close to 100% with respect to B_0 was found when using the matched-filter (Fig. 6.7.b): 97% for NAA, 100% for Cr and 98% for Cho (gains are computed using the power fit results). Concentration-to-noise ratio also showed nearly linear gains with the magnetic field strength: 96% for NAA, 83% for Cr and

100% for Cho. There was a larger variation in the concentration-to-noise ratio fit (R^2 is smaller) compared to the SNR-peak fit, which is due in part to the increased uncertainty in linewidth estimation.

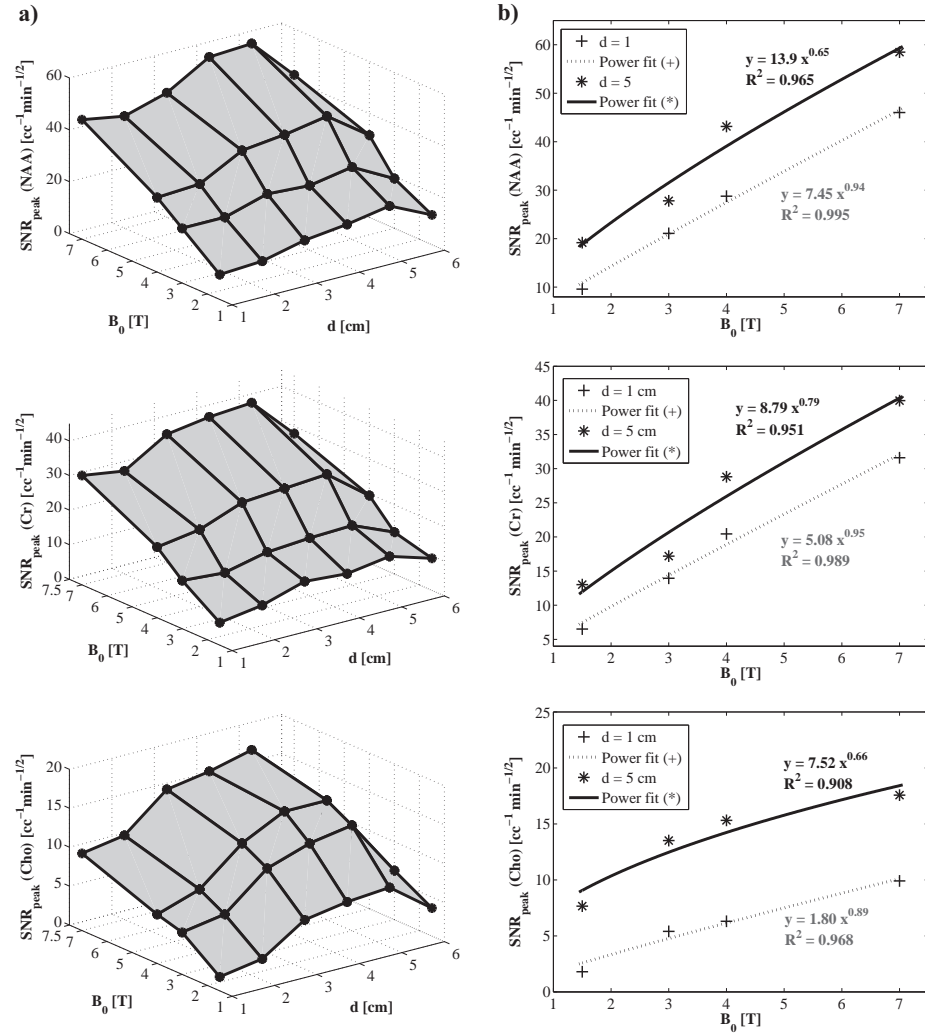


Figure 6.8: a) SNR-peak as a function of B_0 and position with respect to the center of the FOV (d : radius of the region R_2) for NAA, Cho and Cr in measurements using the 8-channel PA coil. SNR increases from the center towards the periphery of the brain ($d=5$ cm). The decay at the periphery ($d=6$ cm) is due to the OVS bands. b) SNR-peak dependence with B_0 for positions close to the center of the FOV ($d = 1$ cm) and at the edges ($d = 5$ cm).

Measurements with the PA coil suffer from an inhomogeneous SNR across the field of view due to the use of smaller receive elements. Higher SNR was obtained at the periphery of the brain as compared to the center of the array coil for NAA, Cho and Cr (Fig. 6.8.a). The periphery of the measurement volume was determined by the position of the outer volume saturation bands, which approximately form an ellipse with a minor axis of 6 cm in the frequency encoding direction. SNR in the center of the FOV was similar to the SNR of the CP coil in the VOI. SNR-peak of NAA, Cr and increased with B_0 . The SNR dependence with B_0 was more linear towards the center of the FOV (Fig. 6.8.b). SNR gains with respect to B_0 at the center (d= 1cm) were: 92% for NAA, 93% for Cr and 85% for Cho. SNR gains with respect to B_0 at the periphery (d= 1cm) were: 57% for NAA, 73% for Cr and 58% for Cho.

Linewidths of NAA, Cr and Cho increased with the magnetic field strength when measured in Hz (Fig 6.9.a). However, they decreased when measured in ppm (Fig 6.9.c). The combined contribution of static and diffusion line broadening components to the linewidth was much stronger than the contribution of intrinsic transverse relaxation T_2 (Fig. 6.9.b). Line broadening was fitted using Eq. (6.9). Since $\alpha_2 \approx 0$, the component due to diffusion can be ignored. An increasing linear function $\alpha_0 + \alpha_1 B_0$ thus describes best the dependence of the line broadening component as a function of B_0 . The constant term α_0 causes the decrease of the linewidth in ppm.

6.4 Discussion

In this work we evaluated quantitative gains in sensitivity and spectral resolution with respect to the magnetic field strength in Proton Echo Planar Spectroscopic Imaging, where a trapezoidal readout gradient is used for simultaneous spatial-spectral encoding. Using the averaged spectrum from a region of interest common to

all studies for a specific type of coil and accounting for T_1 and T_2 related saturation, SNR of NAA, Cr and Cho increased almost linearly with respect to B_0 , consistent with previous findings in imaging experiments [74] and predictions for spectroscopy [73].

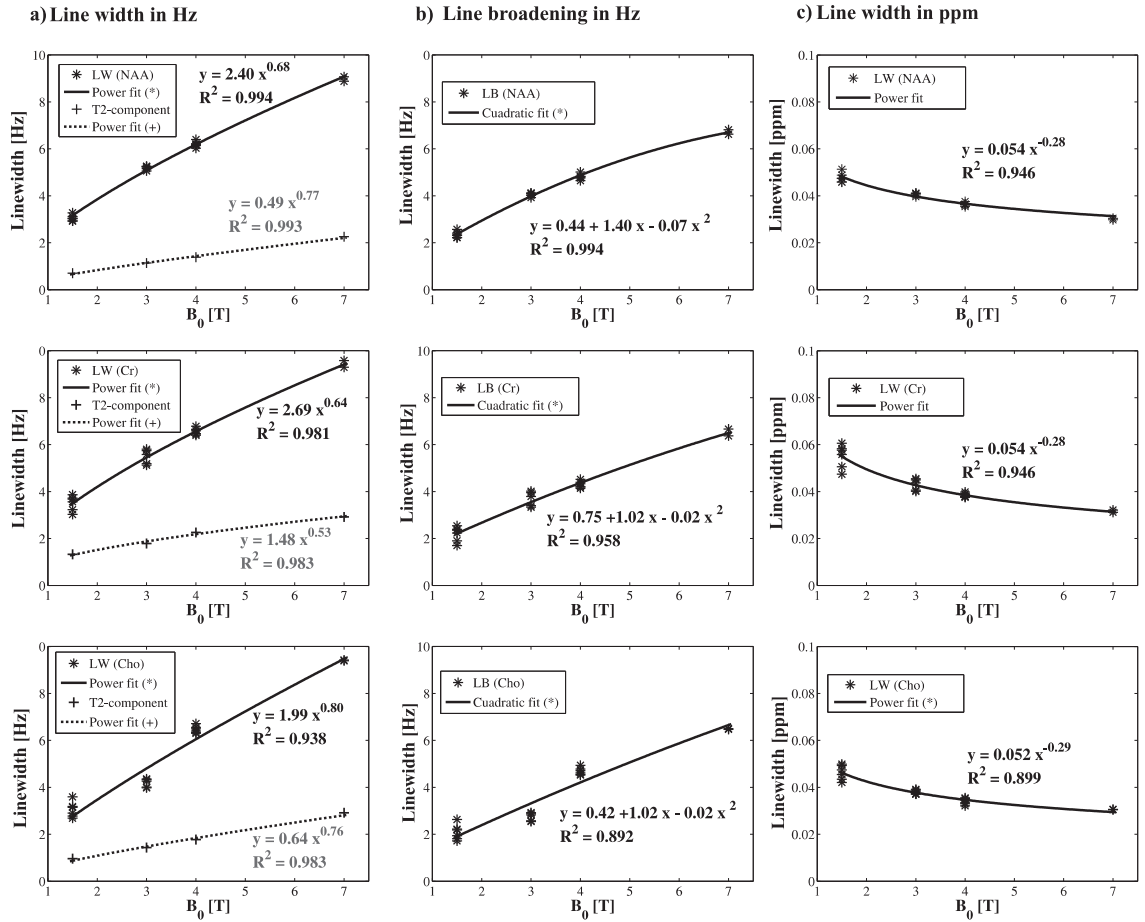


Figure 6.9: Linewidth of NAA, Cr and Cho as a function of B_0 . Decomposition of the linewidth: T_2 -component and component due to line broadening (LB). a) The complete LW in Hz and the T_2 -component increase with B_0 . b) The component due to line broadening increases almost linearly with B_0 ($\alpha_2 \ll \alpha_1$). Since $\alpha_2 \approx 0$, the diffusion contribution to line broadening is negligible. c) The same line width decreases slightly with B_0 when it is measured in ppm.

The use of an exponential matched-filter, with a line broadening parameter adapted to each B_0 , reduced the effect of different spectral linewidths across field strengths resulting in an almost linear gain of SNR with increasing B_0 .

Array coils improve SNR in comparison to the CP coil in peripheral areas close to the array coil elements, at the expense of inhomogeneous sensitivity across the field of view. SNR using the PA coil shows the expected increase with B_0 ; however, this increase is less linear than with the CP coil, which is likely due to differences in array coil performance and coil sensitivity profiles at different field strengths [27], and possibly radiation losses that increase with field strength [74].

To assess the influence of the readout gradient waveform on SNR, we compared the noise variance of a trapezoidal waveform (Figs. 6.10.b and 6.10.c) with the noise variance of an ideal rectangular gradient (Fig. 6.10.a). A general formula to compute the noise variance in the reconstructed image for a variety of possible waveforms that was derived by Pipe and Duerk [94] is given by:

$$\sigma_i = \frac{\sigma^2 \int_{t_0}^{t_1} G_i^2(t) dt}{\left(\int_{t_0}^{t_1} G_i(t) dt \right)^2}, \quad (6.10)$$

where $G_i(t)$ is the i -th waveform, σ is the standard deviation of the white noise and $[t_0, t_1]$ is the sampling interval. σ also corresponds to the noise variance in conventional phase encoded MRSI, when using the same measurement time and voxel size. Using ramp sampling with 60 μ s ramp time and 8 μ s ADC ramp sampling delay, which correspond to the parameters in this work, the increase in noise variance is 11.4% with respect to conventional phase encoding. Without ramp sampling, the increase is 42.9% (Fig. 6.10). Accordingly, the SNR loss in PEPSI caused by the interruptions of the acquisition due to gradient switching [45]) was significantly reduced using ramp sampling with regridding reconstruction. Experimentally, SNR per unit volume and unit time of PEPSI was similar to conventional CSI as reported before [29].

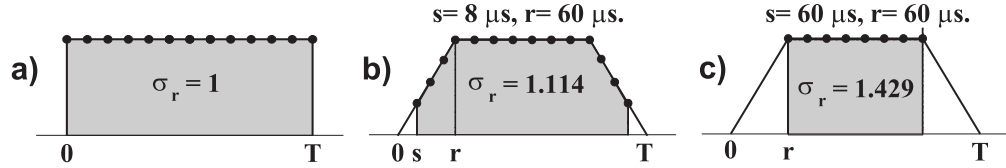


Figure 6.10: Noise variance for different gradient waveforms and sampling schemes (dots) (r: ramp time, s: ADC ramp sampling delay, T: total gradient duration). a) Ideal rectangular gradient. b) Trapezoidal gradient with ramp sampling. c) Trapezoidal gradient without ramp sampling. In all cases $T = 400 \mu\text{s}$ to achieve the same spectral width, which corresponds to the parameters used in this work to encode a 32×32 spatial matrix. The noise variance for each case is normalized to the noise variance of the ideal rectangular gradient.

There is still a small loss in SNR due to the ramp sampling delays (with full ramp sampling, the increase in noise variance is 10.7% with respect to conventional phase encoding). Full ramp sampling is not desirable with our regridding method due to the chemical shift artifact at the beginning and the end of the ramp. During ramp sampling the chemical shift displacement becomes a function of k-space encoding. High k-space information sampled at the beginning of the ramp-up of the readout gradient can become significantly displaced as compared to lower k-space information encoded at the end of the ramp-up phase. This may cause edges of chemically shifted species (e.g. peripheral lipids) to be displaced more strongly than smoothly distributed metabolites. This displacement can be limited by delaying the ramp sampling at the expense of a small loss in SNR.

Significant spectral resolution gains are obtained at higher fields consistent with previous finding for single voxel spectroscopy [79]. Linewidth of NAA, Cr and Cho in Hz increased nearly with a linear function with respect to B_0 , but when measured in ppm they decreased with increasing B_0 . In order to explain the decrease in ppm, the linewidth was decomposed into a contribution from T_2 , line broadening due to microscopic static susceptibility inhomogeneity and line broadening due to

water diffusion in local susceptibility gradients and imaging gradients. Even though T_2 decreases less than linearly with the field strength, its contribution to the final linewidth is very small compared to line broadening due to other effects, i.e. one order of magnitude smaller. Since a linear polynomial $\alpha_0 + \alpha_1 B_0$ describes the dependence of linewidth on field strength, diffusion effects appear to be small. Translating this linear line width change to the ppm scale, it was found that the decrease of the linewidth was mostly due to the constant term α_0 . The physical model used to describe the B_0 -dependence of the singlet linewidth (Eq. (6.8)) thus does not seem to adequately describe the experimental data and the origin of the constant term needs to be further investigated. However, the decrease in line width when measured in ppm, is consistent with previous findings for single voxel spectroscopy [79] and helps to improve the definition of metabolite peaks at high field strength resulting in reduced spectral overlap and improved delineation of J-coupling patterns.

6.5 Summary

In this chapter, the advantages of using high magnetic field strength for Proton Echo Planar Spectroscopic Imaging were analyzed and quantified. Quantification of short echo time spectra was performed using parametric methods including simulated models for macromolecules at each field strength. This work demonstrates feasibility of PEPSI with short echo time over a wide range of field strengths with substantial gains in sensitivity and spectral resolution with respect to field strength and a SNR per unit time and unit volume and spectral line width similar to that of conventional phase encoded spectroscopic imaging techniques.

Chapter 7

Parallel 3D-PEPSI

⁵ This chapter presents the combination of parallel imaging techniques and echo-planar spectroscopic imaging for fast 3D-MRSI of human brain. In order to maximize the acceleration capability, acceleration along two spatial dimensions is performed with the 32-channel soccer-ball receiver array. The SSVD regularization method proposed in Chapter 3 is employed to reduce noise amplification and extra lipid contamination due to residual aliasing. The practical goal is to show feasibility of large scale acceleration for 3D-MRSI with short echo time in order to map the concentrations of the main metabolites of the human brain in 1-2 min.

⁵The work in this chapter was published as: R. Otazo, S-Y. Tsai, F-H. Lin and S. Posse. “Accelerated Short-TE 3D Proton-Echo-Planar-Spectroscopic-Imaging using 2D-SENSE with a 32-Channel Array Coil”. *Magn Reson Med*. In Press. Presented in part at the 14th ISMRM Meeting, Seattle, WA, USA, 2006, pp. 69 and at the 15th ISMRM Meeting, Berlin, Germany, 2007, pp. 46.

7.1 Introduction

Magnetic Resonance Spectroscopic Imaging (MRSI) provides spatial distribution of chemical shifts [8, 9]. As traditionally implemented with phase-encoding, it is very time consuming requiring as many repetitions as there are voxels in the image, e.g. the acquisition time for a 3D experiment is given by $T_a = N_x N_y N_z T_R$, where N_x , N_y and N_z are the dimensions of the spatial grid and T_R is the repetition time. As a consequence, MRSI is usually restricted to low spatial resolution and single slice acquisition in clinical practice. The development of fast MRSI methods that enable whole brain coverage with high spatial resolution remains a major challenge in MRSI research. Many methods have been developed to provide faster spatial-spectral encoding [45], such as echo-planar techniques that allow for simultaneous spatial-spectral encoding using time-varying gradients [46]. Proton Echo Planar Spectroscopic Imaging (PEPSI) [29] is an implementation of this technique with a trapezoidal readout gradient for simultaneous encoding of one spatial dimension (x) and the spectral dimension (ν) providing a net acceleration of N_x over the conventional phase-encoding method with comparable signal-to-noise ratio (SNR) per unit time and unit volume (see Chapter 6). However, 3D-PEPSI is still very time consuming due to phase-encoding along the third spatial dimension.

Accelerated spatial encoding can be accomplished using parallel imaging techniques [15, 16], where subsampled k-space data is acquired using multiple receive coils with spatially-varying reception profiles. The knowledge of the spatially-varying coil sensitivity profiles allows for reconstruction of subsampled data. Acceleration is obtained at the expense of SNR reduction in the reconstructed image. Sensitivity-encoding (SENSE) [16] parallel imaging method has been applied to accelerate phase-encoded [95] and turbo-spin-echo (TSE) MRSI [96]. Even though SENSE reconstruction is applied in the same way as in MRI for each spectral point of the MRSI data, the low resolution characteristics of the MRSI acquisition can produce residual alias-

ing artifacts if the coil sensitivities vary within the voxel and/or the coil sensitivities present discontinuities. In order to reduce these artifacts Dydak *et al.* [95] used extrapolation of the sensitivity maps to avoid discontinuities at the border; Zhao *et al.* [66] employed a two-step SENSE reconstruction to optimize the sensitivity maps; Sanchez *et al.* [67] proposed to use coil sensitivities with higher spatial resolution to optimize the point spread function (PSF) with respect to variation of the coil sensitivities within a voxel. Using 2-D SENSE with TSE-MRSI, Dydak *et al.* have shown 3D-MRSI within 20 min with a 2×2 acceleration along x and y using a $32 \times 32 \times 8$ spatial matrix [97].

Acceleration in parallel imaging is limited by the available SNR and the spatially varying noise amplification factor in the reconstruction (g-factor). Several methods were proposed to reduce the loss in SNR in order to achieve higher accelerations, such as acceleration along more than one spatial dimension, e.g. 2D-SENSE [98] and the use of very high field scanners which increases the baseline SNR and also improve sensitivity encoding by taking advantage of the stronger spatial modulation of the coil profiles [27]. Other works have described the adaptation of the array coil geometry to minimize g-factor [99], regularization in the reconstruction to improve conditioning of the encoding matrix and thus reduce g-factor [48], and arrays with a large number of small elements to increase sensitivity and disparate coil sensitivity encoding along all spatial dimensions [20, 21, 24].

The use of 2D acceleration combined with an array coil with a large number of elements is expected to provide high acceleration capability for 3D encoding. For example, accelerations factors as high as 16 were demonstrated in vivo for imaging experiments using 32-element arrays designed for multidimensional spatial encoding [21]. Moreover; in contrast to single surface coils, large array coils also provide an improved depth penetration for volumetric applications [22].

This goal of this work is to develop a fast method for volumetric MRSI in human

brain at short echo time (TE). Short TE acquisitions are advantageous to maximize sensitivity and to resolve J-coupled metabolites at the expense of the presence of strong lipid and macromolecules resonances that complicates the spectral quantification. The method uses a combination of 3D-PEPSI encoding with acceleration along the two phase-encoding dimensions and 2D-SENSE reconstruction with SSVD regularization (Chapter 3). The 32-channel soccer-ball receiver array coil is employed to maximize the acceleration capability. SSVD regularization and optimization of coil sensitivity estimation are demonstrated to improve the reconstruction of the Point Spread Function (PSF) at high acceleration factors and therefore reduce contamination from peripheral lipids. The experimental goal is to demonstrate feasibility of *in vivo* 3D-MRSI at 3 Tesla and TE=15 ms in 1 minute for a 32x32x8 spatial matrix and 0.7 cc nominal voxel size.

7.2 Accelerated PEPSI Encoding

The 3D-PEPSI sequence [29] consists of water suppression (WS), outer volume suppression (OVS), spin-echo RF excitation, phase-encoding for y and z and the echo-planar readout module for simultaneous encoding of x and f (Fig. 7.1.a). WS is performed using a 3-pulse WET module [42]. OVS is applied along the perimeter of the brain to suppress peripheral lipids. Data acquisition includes water suppressed (WS) and non water suppressed (NWS) measurements. The WS data contains metabolite information and the NWS data contains water information which is used as a reference for spectral phase correction, frequency alignment, Eddy current correction and absolute metabolite concentration estimation.

Spatial-spectral encoding is performed in k-space, where three orthogonal gradients and the evolution of time traverse a path in four dimensions (k_x, k_y, k_z, t) , the Fourier space corresponding to (x, y, z, f) . k_y and k_z are sampled on a Cartesian grid

by phase-encoding prior to readout. k_x and t are sampled simultaneously during the readout interval on a zig-zag trajectory defined by a periodic trapezoidal gradient (Fig. 7.1.b). Two-dimensional acceleration is performed by sub-sampling uniformly the k-space data along the k_y and k_z dimensions by factors R_y and R_z respectively. The acquisition time is then given by $T_a = \frac{N_y N_z}{R_y R_z} T_R$.

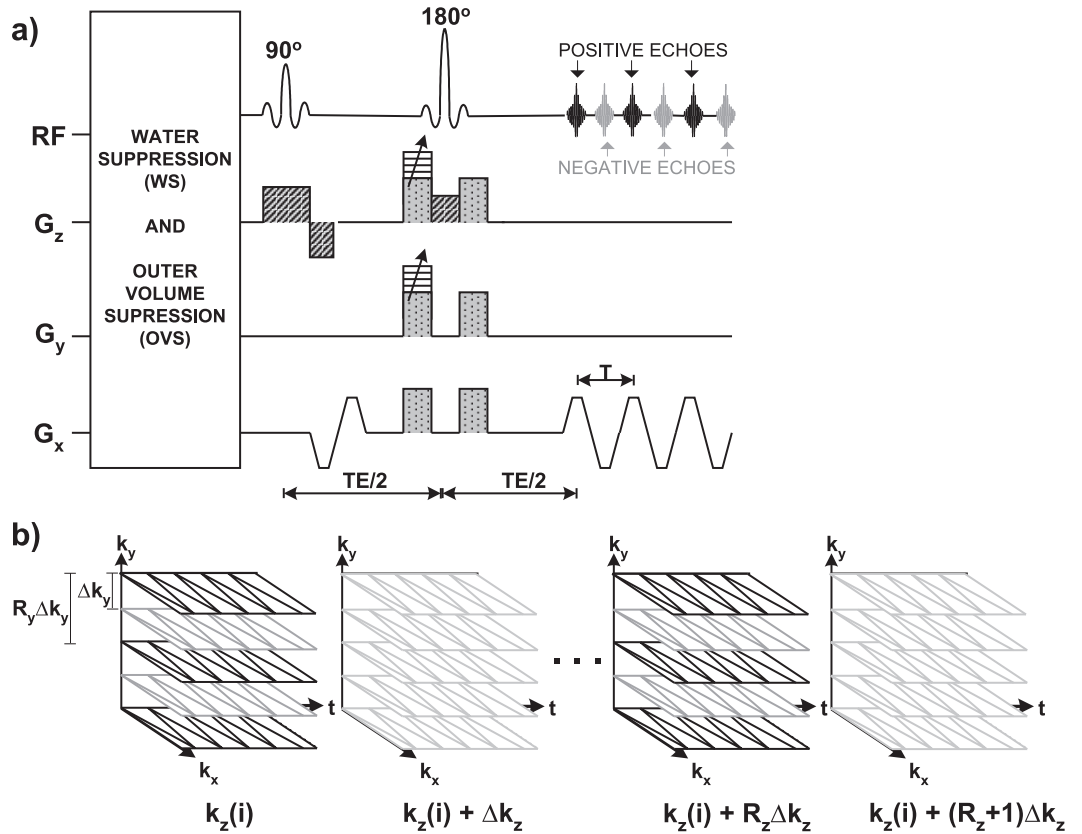


Figure 7.1: a) 3D-PEPSI pulse sequence with water suppression (WS), outer volume suppression (OVS), spin-echo RF excitation, phase encodes on G_y and G_z for y and z encoding and trapezoidal G_x gradient for simultaneous encoding of x and f . b) The resulting k-space trajectory is composed by parallel planes of zig-zag k_x - t trajectories. Δk_y and Δk_z determine the Cartesian sampling grid for k_y and k_z . The black lines represents the trajectory after sub-sampling k_y and k_z by a factor R_y and R_z respectively.

7.3 SSVD-SENSE-PEPSI Reconstruction

SENSE-PEPSI reconstruction is performed by first reconstructing the accelerated spatial dimensions and then the spectral dimension by separate processing of positive and negative echoes (Fig. 7.2). Accelerated positive and negative echoes ($\mathbf{Y}^p(\mathbf{k}, t)$ and $\mathbf{Y}^n(\mathbf{k}, t)$ respectively, where \mathbf{k} is the k-space vector) are sorted into separate arrays after time reversal of the data acquired with negative gradients. A spatial Fourier transform is then applied to obtain the spatially aliased signals $\mathbf{y}^p(\mathbf{r}, t)$ and $\mathbf{y}^n(\mathbf{r}, t)$, where \mathbf{r} is the position vector. 2D-SENSE with SSVD regularization as described below is applied to each time point of $\mathbf{y}^p(\mathbf{r}, t)$ and $\mathbf{y}^n(\mathbf{r}, t)$ to remove aliasing along y and z . Coil-by-coil SENSE reconstruction are computed by multiplying the 2D-SENSE reconstruction by each of the individual coil profiles ($c^p(\mathbf{r})$ for positive echoes and $c^n(\mathbf{r})$ for negative echoes) to obtain $\hat{\mathbf{s}}^p(\mathbf{r}, t)$ and $\hat{\mathbf{s}}^n(\mathbf{r}, t)$. This step is required to correct the spectral phase of the data from each coil separately due to the different spectral phase pattern presented by each coil. After reconstructing the spatial dimensions, the water-suppressed (WS) data from each coil is separately

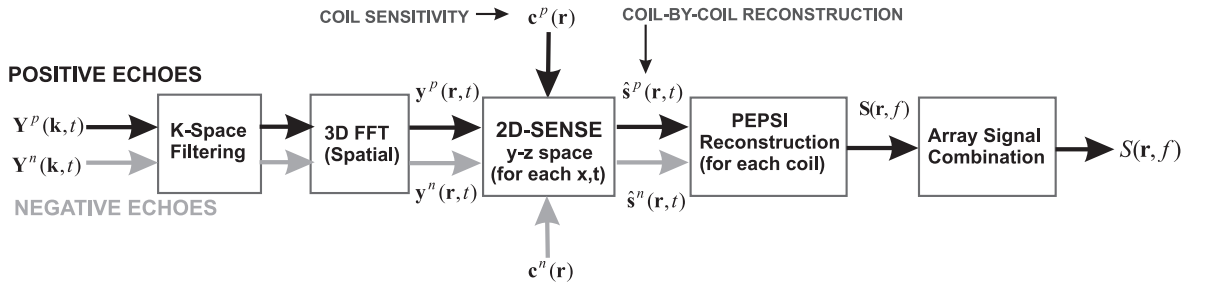


Figure 7.2: SENSE-PEPSI reconstruction diagram. Accelerated positive and negative echoes are reconstructed separately using 2D-SENSE reconstruction for each $x-t$ point. Coil-by-coil PEPSI reconstruction is then performed where positive and negative echoes are combined after spectral phase correction. The final spectroscopic image $S(\mathbf{r}, f)$ data is obtained by sensitivity-weighted combination of the coil-by-coil reconstruction.

phase-corrected and frequency aligned along the spectral dimension using the corresponding water reference, i.e. non-water-suppressed (NWS) data set. Zero-order phases of the water signals are automatically determined in the NWS data, and these phase corrections are applied to the corresponding WS data arrays. Spectral frequency assignment in the WS data is made assuming that the largest signal in the NWS data represents water. Positive and negative echo data are then added. Eddy-current correction [81] is applied to the reconstructed NWS and WS data using the phase of the reconstructed NWS data to remove residual line shape distortion and possible water sidebands. The resulting multi-coil spatial-spectral signal $\mathbf{S}(\mathbf{r}, f)$ is then combined using a sensitivity-weighted combination to obtain the final spectroscopic image $S(\mathbf{r}, f)$, i.e. SENSE reconstruction of fully-encoded data:

$$S(\mathbf{r}, f) = \frac{\sum_{l=1}^{N_c} w_l^*(\mathbf{r}) S_l(\mathbf{r}, f)}{\sum_{l=1}^{N_c} w_l^*(\mathbf{r}) w_l(\mathbf{r})}, \quad (7.1)$$

where $S_l(\mathbf{r}, f)$ is the reconstructed signal for the l -th coil, $w_l(\mathbf{r})$ is the coil sensitivity given by the reconstructed NWS data, and $*$ denotes complex conjugation.

7.3.1 2D-SENSE with SSVD Regularization

2D-SENSE reconstruction is performed on the y - z space for each point of the x - t space. The discretized signal acquired by each coil in k -space with reduced encoding given by uniform sub-sampling of k_y and k_z by factors R_y and R_z respectively can be represented for each time point as:

$$Y_l(k_x, k_y, k_z) = \sum_{x,y,z} s(x, y, z) c_l(x, y, z) e^{j2\pi(k_x x + R_y k_y y + R_z k_z z)}, \quad l = 1, 2, \dots, N_c, \quad (7.2)$$

where $s(x, y, z)$ is the object function to be reconstructed, $c_l(x, y, z)$ is the coil sensitivity function and N_c is the number of coils. Applying a spatial discrete Fourier transform (DFT), we obtain the spatially aliased signals:

$$y_l(x, y, z) = \sum_{m_y=0}^{R_y-1} \sum_{m_z=0}^{R_z-1} s(x, y + m_y \hat{W}_y, y + m_z \hat{W}_z) c_l(x, y + m_y \hat{W}_y, y + m_z \hat{W}_z), \quad (7.3)$$

where $\hat{W}_y = W_y/R_y$ and $\hat{W}_z = W_z/R_z$ are the reduced FOV along y and z (W_y and W_z represent the full FOV). Concatenating the signals acquired by each coil in a column vector \mathbf{y} ($N_c \times 1$), the encoding equation with 2D acceleration for each point in the aliased images is given by $\mathbf{y} = \mathbf{E}\mathbf{s}$, where the entries of the encoding matrix \mathbf{E} ($N_c \times R_y R_z$) are given by the coil sensitivity functions at the corresponding positions and the vector \mathbf{s} ($R_y R_z \times 1$) corresponds to the set of voxels to be reconstructed. SSVD reconstruction (Chapter 3) was applied to solve the system. SSVD regularization procedure will improve SNR at the expense that certain features will be omitted in the reconstructed image, e.g. blurring in positions with strongly overlapped coil sensitivities. Therefore it allows a tunable tradeoff between ideal accuracy and practical image quality and SNR. To tune the parameter c_0 , the reconstruction of the data to estimate the coil sensitivity maps with simulated acceleration is employed for different values of c_0 between 10 and 100 with steps of 5. The value of c_0 that proportioned the smallest root mean square error (RMSE) was chosen.

7.3.2 Coil Sensitivity Estimation

Coil sensitivity maps are estimated using spectral water images from an extra fully-sampled NWS acquisition with fewer time points, e.g. 16 echoes. The reference signal is appropriate since it is acquired with the same readout as the accelerated PEPSI data, which is advantageous to avoid spatial registration errors. Following the inverse Fourier transform law, the integral along the spectral domain is contained in the first time point, which it is used as the spectral water image for each coil. The change in contrast due to a shorter T_R and anatomical features were removed by normalizing the reference signal of each coil by the sum-of-squares (SoS) combination of the multi-coil reference data (Chapter 2, section 2.4.4). Refinement of the raw sensitivity maps is performed using a 3-rd order polynomial fit.

7.4 Low Spatial Resolution Effects

MRSI presents intrinsically low SNR due to the relative low metabolite concentrations compared to water and lipids constraining the sampling of k-space to a few points in the central region, e.g. common image matrix sizes are 16×16 or 32×32 . Reconstruction from truncated k-space data can be represented as the convolution of the true object function and the Point Spread Function (PSF) of the reconstruction method. The PSF is the impulse response of the reconstruction method describing the signal origin in that voxel. For truncated k-space data sampled at the Nyquist rate (no acceleration), the PSF limits the spatial resolution of the reconstructed image to its effective width and produces Gibbs ringing due to its oscillatory nature. In MRSI, spatial ringing can produce strong spectral contamination from lipid components located at the periphery of the brain. For accelerated MRSI data, where truncated k-space data are sampled at a multiple of the Nyquist rate, the PSF will be also aliased. Residual aliasing in SENSE reconstruction could result if the sensitivity functions vary over the effective width of the PSF and/or the sensitivity maps present discontinuities, e.g. the border of the object [66]. The following approaches are presented to reduce residual aliasing in SENSE reconstruction:

- Apodization of accelerated data in k-space using a Hamming window to reduce the side lobes of the PSF at the expense of spatial resolution loss.
- Extrapolation of the coil sensitivity maps following the polynomial model beyond the border of the brain to avoid discontinuities.
- SSVD regularization to reduce the effect of inconsistencies between the polynomial model and the true coil sensitivities especially in the extrapolation region.

Data truncation effects for 2D-SENSE reconstruction were evaluated by computing the PSF. The PSF was computed by reconstructing a simulated source point at a

specific spatial position using interpolated coil sensitivity profiles in order to have 4 points along each dimension within each voxel.

7.5 Experimental Validation

7.5.1 Data Acquisition

3D-PEPSI acquisitions were performed on healthy volunteers using a 3T MR scanner (Tim Trio, Siemens Medical Solutions, Erlangen, Germany) equipped with Sonata gradients (maximum amplitude: 40 mT/m, slew rate: 200 mT/m/ms) and the 32-channel soccer-ball array [25]. Outer volume suppression was applied along the perimeter of the brain using 14 slices: 8 slices were manually positioned in the axial plane and 6 slices were fixed on the boundaries of the 3D slab. Three accelerations were employed: $R = 4$ ($R_y = 2, R_z = 2$), $R = 8$ ($R_y = 4, R_z = 2$) and $R = 12$ ($R_y = 6, R_z = 2$). For comparisons the fully-encoded data was also acquired. Data acquisition includes water suppressed (WS) and non water suppressed (NWS) scans. Data were acquired in an axial orientation using a $32 \times 32 \times 8$ spatial matrix to reconstruct 8 axial slices (FOV: $240 \times 240 \times 100$ [mm³], nominal voxel size: 0.7 cc). Fully encoded data were acquired in 8 min using $T_R = 2$ sec, $T_E = 15$ msec. The readout gradient consisted of 512 periods. The spectral bandwidth after positive and negative echo separation was 1087 Hz. A second NWS scan with much shorter readout duration (16 periods) and $T_R = 500$ msec was acquired to estimate coil sensitivity maps (2 min). Data were collected with 2-fold over sampling for each readout gradient separately to improve regridding performance and using a ramp sampling delay of $8\mu\text{s}$ to limit chemical shift artifacts. After regridding, 2-fold oversampling was removed. The data sets were filtered in k-space using a regular Hamming window along the x and y dimensions which increased the effective voxel size to 1.8 cc.

7.5.2 Spectral Fitting, Metabolite Images and Error Quantification

Spectra were quantified using LCModel fitting [44]. Basis sets included 18 metabolites which were generated by simulating the spectral pattern of each metabolite using density matrix simulations based on chemical-shift and J-coupling values [100]. The PEPSI sequence was approximated as a simple spin-echo sequence without slice selective gradients and assuming infinitely short RF pulses.

Metabolic concentration values in the reconstructed WS data were computed in reference to the NWS data using the water-scaling method with the following scale factors: water concentration= 55 molar and attenuation correction for water and metabolites= 1.0. Combined absolute concentrations in milliMolar [mM] units were presented in this work: NAA=NAA+NAAG, Cr= Cr+PCr and Glu= Glu+Gln. Choline (Cho) was represented by GPC only. Errors in metabolite quantification in LCmodel (%SD) are expressed in Cramer-Rao lower bound (CRLB), i.e. the lowest bound of the standard deviation of the estimated metabolite concentration expressed as percentage of this concentration, which when multiplied by 2.0 represent 95% confidence intervals of the estimated concentration values.

Metabolite concentration images were created using the following thresholds to accept voxels: (a) CRLB \leq 20% for NAA and Cr, CRLB \leq 30% for Cho, and CRLB \leq 50% for Glu and (b) spectral linewidth (FWHM) \leq 0.2 ppm. Error maps were computed using the absolute value of the difference between the accelerated data reconstruction and the fully-encoded data reconstruction. Finally, the metabolite concentration maps were interpolated to a $128 \times 128 \times 8$ matrix using bilinear interpolation to improve visualization.

Lipid images were created by spectral integration between 0.5 and 1.6 ppm of the reconstructed absorption mode spectra.

7.6 Results

7.6.1 g-Factor

The g-factor obtained from 1D acceleration was reduced considerably by 2D acceleration (Fig. 7.3). As a result, the average SNR decrease given by $\bar{g}\sqrt{R}$ where \bar{g} is the average g-factor for $R = 8 \times 1$ is 12.6 but only 4.4 for $R = 4 \times 2$. Therefore, there is a 2.8-fold gain in average SNR performance when using 2D-SENSE for an 8-fold acceleration. However; for high accelerations ($R = 4 \times 2$ and $R = 6 \times 2$), g-factor still presented large values at central zones (Fig. 4.a). SSVD reconstruction reduced g-factor for $R = 4 \times 2$ and $R = 6 \times 2$ specially in central zones where the coil sensitivities have low value and overlap thus producing an ill-conditioned encoding matrix. The threshold of $c_0 = 25$ on the condition number of the encoding matrix represented a good tradeoff to achieve both reasonable numerical conditioning and good unaliasing

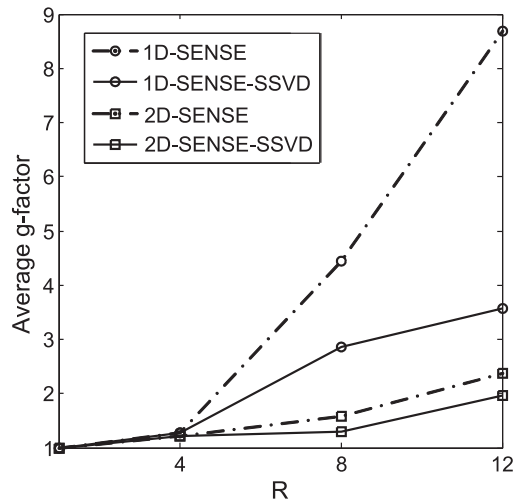


Figure 7.3: Average g-factor for simulated 1D and 2D accelerations using the estimated sensitivity maps. For SENSE-SSVD reconstruction, a threshold $c_0 = 25$ on the condition number of the encoding matrix was employed.

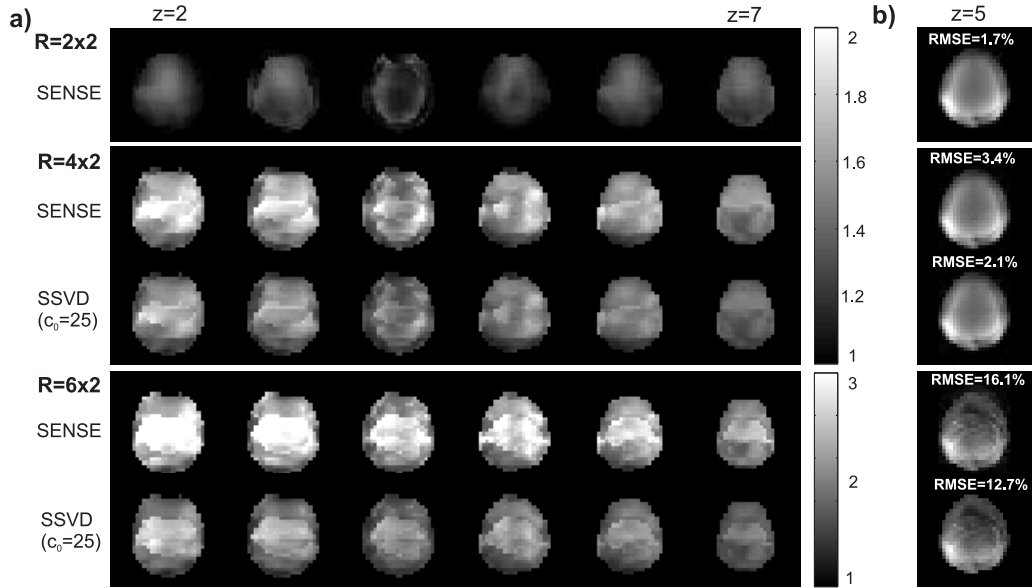


Figure 7.4: a) g-factor maps for slices 2-7 and b) reconstruction of the 1-st time-domain point of the NWS data from slice 5 for different accelerations. The threshold on CN was set using the reconstruction with $R = 4 \times 2$ ($c_0 = 25$). RMSE is the average RMS error with respect to the fully-encoded data ($R = 1 \times 1$).

performance. For $R = 2 \times 2$, the encoding matrix was well-conditioned and therefore the SSVD solution did not affect the reconstruction. Even though SENSE-SSVD provided low and more uniform g-factors at high accelerations, the SNR penalty due to highly undersampled data (\sqrt{R} -factor) imposed the limit for the maximum feasible acceleration. SENSE-SSVD reconstruction of the 1-st time-domain point of the accelerated NWS data presented good performance up to $R = 4 \times 2$ (Fig. 4.b).

7.6.2 Point Spread Function

2D-SENSE reconstruction of the accelerated data with coil sensitivity extrapolation beyond the border of the brain provided a properly unaliased PSF (Fig. 7.5). Without sensitivity extrapolation, SENSE reconstruction may lead to residual aliasing

artifacts due to discontinuities at the object border. The SSVD solution improved aliasing suppression for larger accelerations ($R = 4 \times 2$ and $R = 6 \times 2$). The aliasing peaks along the y dimension were reduced by 35 dB approximately for $R_y = 2$ and $R_y = 4$. For $R_y = 6$, standard SENSE failed to remove the aliasing, e.g. peak to the left. With SSVD the aliasing peaks for $R_y = 6$ were at least reduced by 20 dB.

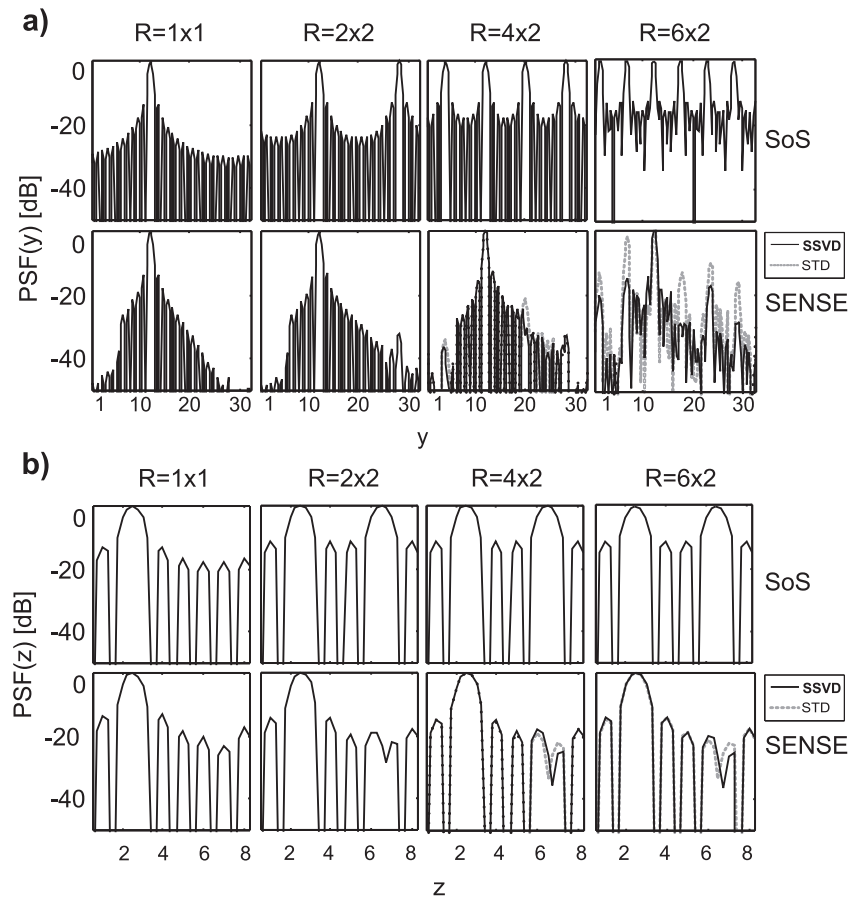


Figure 7.5: PSF along y (a) and z (b) for different accelerations. The source point was located at the border of the brain, where there is a discontinuity of the reference signal to estimate the coil sensitivities. The top row shows the aliased PSF for SoS reconstruction of the accelerated data and the bottom row the unaliased PSF for SENSE reconstruction. Note that the reconstruction using SSVD presented better aliasing suppression.

The aliasing peak along the z dimension was reduced by 20 dB approximately for $R_z = 2$. The PSF of SENSE reconstruction is asymmetric which is due in part to asymmetries in the array coil configuration. Note that for $R = 1 \times 1$, the PSF of SENSE reconstruction presented lower side lobes than the one for sum-of-squares (SOS) reconstruction, which results in reduced contamination from outside voxels. This is due to the better defined coil sensitivity functions used in SENSE. For SoS reconstruction, coil sensitivities are assumed to be equal to the spatial SNR profiles of the data; for SENSE a polynomial fit was employed.

7.6.3 Metabolite Maps and Spectra

Metabolite concentration mapping was feasible up to $R = 4 \times 2$ ($T_a = 1$ min) with a moderate reduction in spatial-spectral quality when compared to the fully-encoded reconstruction: RMSEs were less than 5%; and the increase in average CRLBs were 5.1%, 6.8%, 10.7% and 13.9% for NAA, Cr, Cho and Glu respectively. $R = 2 \times 2$ ($T_a = 2$ min) presented similar results to the fully-encoded reconstruction: RMSEs were less than 3%; and the increase in average CRLBs were 2.0%, 2.5%, 5.6% and 5.4% for NAA, Cr, Cho and Glu respectively. Fig. 7.6 shows the concentration maps for the three major single resonances NAA, Creatine and Choline. Fig. 7.7.a shows the corresponding results for Glutamate (a multiplet resonance with comparatively

Metabolite	Concentration [mM]		
	$R = 1 \times 1$	$R = 2 \times 2$	$R = 4 \times 2$
NAA	9.2±3.4	9.4±3.8	9.5±4.3
Cr	7.3±2.4	7.2±2.2	7.2±2.8
Cho	1.6±0.7	1.4±0.8	1.4±0.9
Glu	8.3±3.6	8.5±3.9	8.8±5.2

Table 7.1: Average absolute concentrations and standard deviations.

low sensitivity). Table 1 shows average concentration values for each acceleration, which are within the range of concentration values reported in previous studies [101]. The inferior slices (2 and 3) suffered from larger errors since the coil sensitivities are lower in those brain regions. The accuracy of spectral quantification, indicated by the CRLB from LCModel fitting, decreased with acceleration due to reduced SNR specially in the inferior slices for the reason mentioned above. The Glutamate

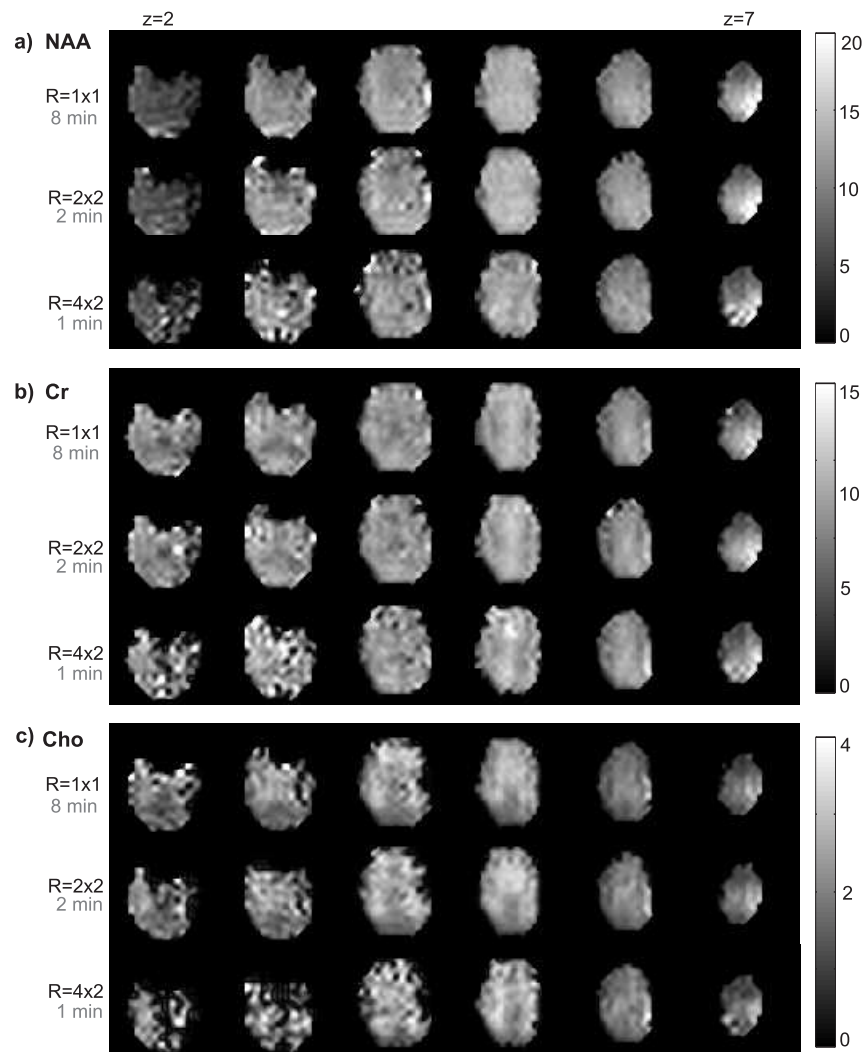


Figure 7.6: Metabolite concentration maps of a) NAA, b) Creatine and c) Choline.

image shows similar intensity in central and lateral gray matter (GM), and much lower intensity in white matter (WM) (approximately 50% less in the voxel from Fig. 7.7.a), consistent with previous studies (ratio $\text{Glu(GM)}/\text{Glu(WM)} = 2.4 \pm 0.5$ [102]). Examples of spectra show decreased SNR with higher acceleration as expected and small distortions around the lipid region (1.3 ppm) due to imperfections in the estimation of coil sensitivity information at the periphery (Fig. 7.7.b).

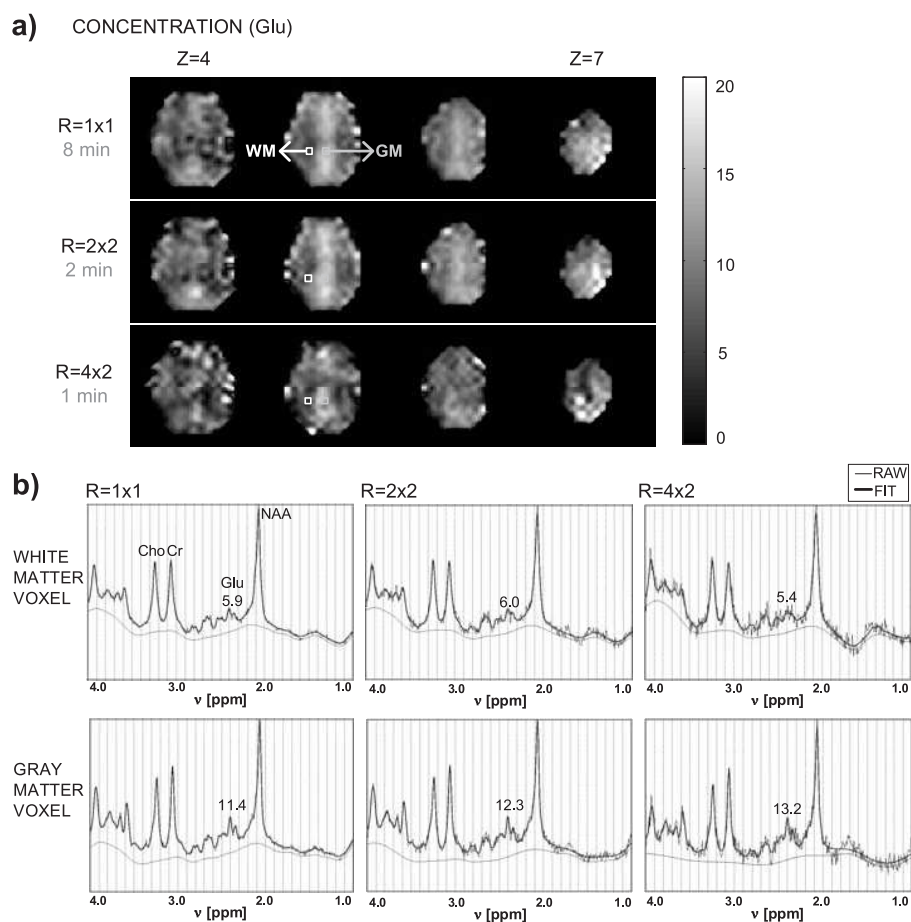


Figure 7.7: a) Glutamate concentration maps at different accelerations for slices 4-7. b) Raw absorption mode spectrum (black line) and corresponding LCMoel fit (red line) for a gray matter (GM) voxel and a white matter (WM) voxel (voxel locations are indicated in part a). The remaining baseline is given by the smooth black curve. The concentration of Glutamate is given in each case.

However, extra lipid contamination was highly reduced by extrapolation of the sensitivity maps and the SSVD reconstruction. Fig. 7.8.a shows lipid maps for slice 5 from the fully-encoded data ($R = 1 \times 1$ and $R = 4 \times 2$ using standard SENSE (STD) and SSVD reconstruction. Accelerated data reconstruction showed lipid contamination due to residual aliasing specially in central zones where the encoding matrix is ill-conditioned as shown in the g-factor maps in Fig. 7.4.a. On average the lipid contamination in standard SENSE reconstruction was reduced by a factor of 1.6 when using SSVD reconstruction. Fig. 7.8.b shows an example from a white matter region where the lipid contamination was reduced by a factor of 1.8.

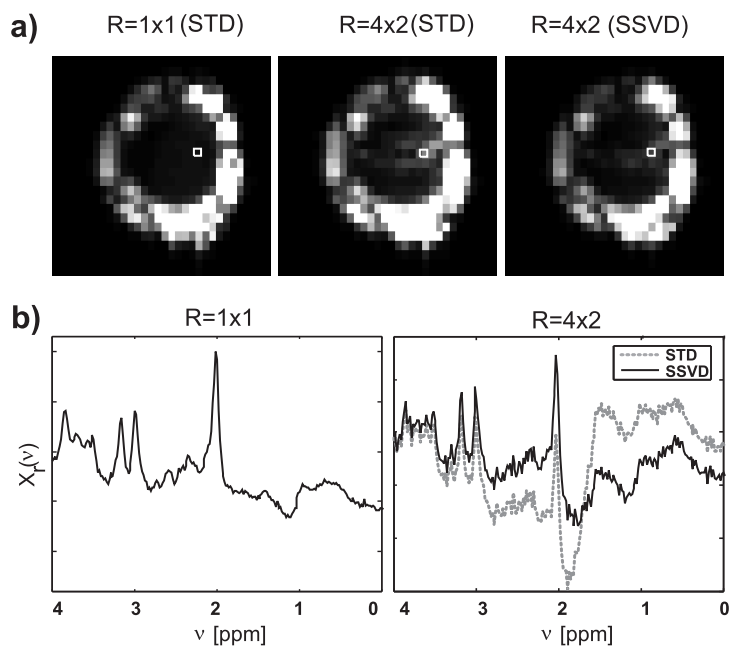


Figure 7.8: a) Lipid image from slice 5 for $R = 1 \times 1$ and $R = 4 \times 2$ using standard SENSE (STD) and SSVD reconstruction. b) Absorption mode spectrum from the voxel indicated in part a. Note the reduction in lipid contamination due to residual aliasing in areas with high g-factor seen in Fig. 7.4.b when using SSVD reconstruction as compared to standard SENSE reconstruction.

7.7 Discussion

In this Chapter, feasibility of fast volumetric metabolic imaging in human brain was demonstrated using a combination of 3D-PEPSI encoding with large scale two-dimensional acceleration and SENSE reconstruction with the 32-channel soccer-ball array coil. The acquisition of short T_E (15 ms) 3D-PEPSI with a $32 \times 32 \times 8$ spatial matrix can be accelerated up to 1 min to map the concentrations of N-Acetyl-Aspartate (NAA), Creatine (Cr), Choline (Cho) and Glutamate (Glu) at the expense of a moderate reduction in spatial-spectral quality. The short encoding time constitutes a major advance as compared to previous studies using parallel MRSI, such as data presented in [97] that required 20 min of encoding time for the same spatial matrix.

Acceleration applied simultaneously to the k_y and k_z phase-encoding dimensions increased the acceleration capability by reducing the large SNR loss from high 1D accelerations. The conditioning of the reconstruction improved considerably by exploiting sensitivity encoding along two dimensions and therefore reduced g-factor as described in [98]. The difference between 1D-SENSE and 2D-SENSE for the same net acceleration factor is given by the g-factor. 2D-SENSE presents a lower and more spatially uniform g-factor than 1D-SENSE (see Fig. 7.3 and Fig. 7.4). For example, the average SNR decrease for $R = 8 \times 1$ is 12.6 but only 4.4 for $R = 4 \times 2$. Therefore, there is a 2.8-fold gain in average SNR performance when using 2D-SENSE in this work for an 8-fold acceleration.

Even though the combination of the 32-channel soccer-ball array and two-dimensional acceleration improved the conditioning of the encoding matrix, g-factor was still high in positions with low-value and overlapped coil sensitivities. When the sensitivities of the receiver coils severely overlap, different rows of the encoding matrix become nearly identical. This causes the encoding matrix to become nearly singular and

therefore highly susceptible to amplify noise and errors in the coil sensitivity estimation associated with small singular values. Regularization of the encoding matrix inversion can be performed by constraining the SVD solution. SSVD regularization (Chapter 3) proved to work adequately for SENSE to reduce g-factor at the expense of spatial resolution. Since MRSI is intrinsically a low spatial resolution technique, this effect is small. The SSVD was tuned using the 1st time-domain point of the NWS data (maximum SNR), and the same procedure was applied to later time points which are noisy.

The use of sensitivity extrapolation beyond the borders of the object improved the reconstruction of the PSF consistent with previous findings [95] and SSVD reconstruction reduced the effect of errors in coil sensitivity modeling. These two factors were very important to reduce extra-cranial lipid contamination due to residual aliasing. SSVD regularization reduced the lipid contamination inside the brain as compared to standard SENSE reconstruction by a factor of 1.6 on average due to better aliasing suppression in regions with ill-conditioned encoding matrix.

The maximum attainable acceleration was evaluated quantitatively using the RMSE of the metabolite concentration with respect to the non accelerated acquisition and the CRLB from LCModel spectral fitting. The CRLB represents the combined influence of SNR, spectral line width and spectral shape on the accuracy of the fit. Based on these parameters, $R = 4 \times 2$ presented an acceptable reduction in spatial-spectral quality to map the concentrations of NAA, Cr, Cho and Glu.

In future work, we are planning to implement the technique at 7 Tesla using the 32-channel soccer-ball array. The use of high magnetic field strength has been demonstrated to improve the performance of parallel imaging reconstruction by increasing the baseline SNR and providing stronger spatial modulation of the coil sensitivities [27]. However, in order to take advantage of the larger acceleration capability and to achieve adequate volume coverage for 3D acquisitions it is necessary to maximize the

uniformity of the spectral quality using improved volumetric shim algorithms and automatic placement of the OVS slices.

7.8 Summary

A high-speed method for 3D-MRSI of human brain was developed using the combination of echo-planar MRSI and parallel imaging with a large-N receiver array. The SSVD regularization from Chapter 3 was employed to reduce noise and errors in regions with low-value and overlapped coil sensitivities. As a result, the method improved the reconstruction of the PSF and reduced lipid contamination inside the brain from peripheral regions. *In vivo* results show that single-average 3D-MRSI with a $32 \times 32 \times 8$ spatial matrix and 0.7 cc nominal voxel size at 3 Tesla can be accelerated with minimum acquisition time of 1 min to map the concentrations of the main metabolites. The short encoding time makes the method suitable for volumetric mapping of metabolites as an add-on in clinical MR studies.

Chapter 8

Superresolution Parallel PEPSI

³ The superresolution SENSE (SURE-SENSE) method introduced in Chapter 5 is applied to PEPSI encoding for fast metabolic imaging with high spatial resolution in human brain using the 32-channel soccer-ball array.

8.1 Introduction

MRSI is constrained by low SNR and slow encoding methods [45]. As a consequence, k-space coverage is sacrificed to achieve an adequate SNR within a feasible acquisition time. The lack of high k-space information leads to limited spatial resolution and Gibbs ringing when the Fourier transform is directly applied to reconstruct the image. For proton MRSI in human brain, the effect of truncated k-space sampling can be particularly severe due to the presence of an intense signal arising from subcutaneous lipids in the scalp. The resulting lipid resonances cover a large spectral region and overlap with the metabolite resonances. Gibbs ringing produces lipid contamination

³The work in this chapter was submitted as part of a full paper to Magnetic Resonance in Medicine: R. Otazo, F-H. Lin, G.C. Wiggins, R. Jordan and S. Posse. “Superresolution Parallel Magnetic Resonance Imaging”.

inside the brain which reduces the spectral quality and complicates the quantification of metabolites (Fig. 8.1). Several methods were developed to reduce this effect [103]. For example, the lipid resonance can be saturated in the acquisition by an inversion recovery scheme [104] at the expense of sensitivity loss. The outer volume suppression (OVS) method [105] saturates the signal from the periphery at the expense of spatial coverage loss. Post-processing methods such as k-space extrapolation of the lipid signal using the Papoulis-Gerchberg algorithm were also proposed [82].

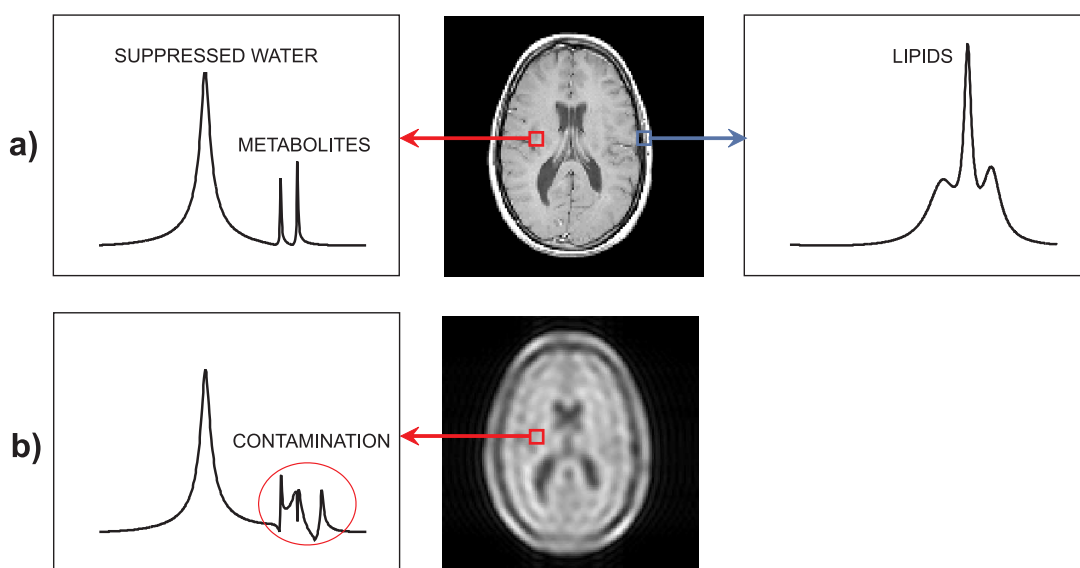


Figure 8.1: a) High spatial resolution MRSI: spectrum from a voxel inside the brain and at the periphery where lipids are located. b) Low spatial resolution MRSI: lipid contamination from conventional Fourier reconstruction due to Gibbs ringing.

In this Chapter, the SURE-SENSE parallel imaging method introduced in Chapter 5 is applied to PEPSI encoding for fast metabolic imaging with high spatial resolution in human brain using the 32-channel soccer-ball array. Acceleration of PEPSI encoding is performed by performing a low spatial resolution acquisition. SURE-SENSE reconstruction is performed using coil sensitivities estimated from the fully-sampled water reference acquisition.

8.2 Methods

8.2.1 Data Acquisition

Human brain MRSI data with two spatial dimensions were acquired with Proton Echo Planar Spectroscopic Imaging (PEPSI) [29, 106] in axial orientation using a $64 \times 64 \times 512$ spatial-spectral matrix (x, y, ν) . Data acquisition was performed on a 3 Tesla MR scanner (Tim Trio, Siemens Medical Solutions, Erlangen, Germany) using the 32-channel soccer-ball array coil [25] (Fig. 1.1). The FOV was $256 \times 256 \text{ mm}^2$ and the slice thickness was 20 mm resulting in a voxel size of 0.32 cc (in-plane spatial resolution of 16 mm^2). The spectral width was set to 1087 Hz. The 2D-PEPSI sequence (see Fig.7.1) consisted of water-suppression (WS), outer-volume-suppression (OVS), spin-echo RF excitation, phase-encoding for y and the echo-planar readout module for simultaneous encoding of x and t . Data acquisition included water-suppressed (WS) and non-water-suppressed (NWS) scans. The NWS scan was performed without the WS and OVS modules; and it was used as a reference to estimate the coil sensitivity maps, spectral phase correction, Eddy current correction and absolute metabolite concentration. The high resolution NWS and WS PEPSI data sets were acquired in 2 min each using single signal average. Low resolution data was obtained from the 32×32 central k-space matrix which represents an acceleration factor of 2.

8.3 SURE-SENSE-PEPSI Reconstruction

SURE-SENSE reconstruction (see Chapter 5) is applied to the low resolution data using the high resolution coil sensitivity maps for each spectral point separately. For error quantification purposes, the high resolution acquisition was reconstructed by applying DFT reconstruction to each coil and sensitivity-weighted combination of

the individual coil images (DFT-SW), i.e. standard SENSE reconstruction for the fully encoded data. For comparison purposes, the low resolution acquisition was conventionally reconstructed using the DFT-SW procedure with low resolution coil sensitivity maps and the result was interpolated to the high resolution spatial grid by zero-filling the k-space data. The interpolated conventional reconstruction will be referred to as DFT-SW-ZF reconstruction. PEPSI reconstruction as described in Chapter 7 is then applied to get the spectroscopic image.

8.4 Spectral Fitting and Metabolite Images

Water images were obtained by spectral integration of the reconstructed NWS data. Lipid images were computed by spectral integration of the reconstructed WS data from 0 to 2.0 ppm. Metabolite images were obtained by spectral fitting using LCModel [44] with analytically modeled basis sets [106]. Metabolite imaging performance was assessed using the MSE with respect to the high resolution metabolite image. Spectral fitting errors in LCModel were computed using the Cramer-Rao Lower Bound (CRLB, the lowest bound of the standard deviation of the estimated metabolite concentration expressed as percentage of this concentration), which when multiplied by 2.0 represent 95% confidence intervals of the estimated concentration values. A threshold of 20% was imposed on the CRLB to accept voxels.

8.5 Results

Superresolution SENSE reconstruction reduced the strong effect of k-space truncation in the simulated low resolution (32×32) MRSI data set, resulting in metabolite maps with better spatial resolution and spectra with higher quality as compared to the conventional DFT reconstruction with k-space zero-filling (Fig. 8.2).

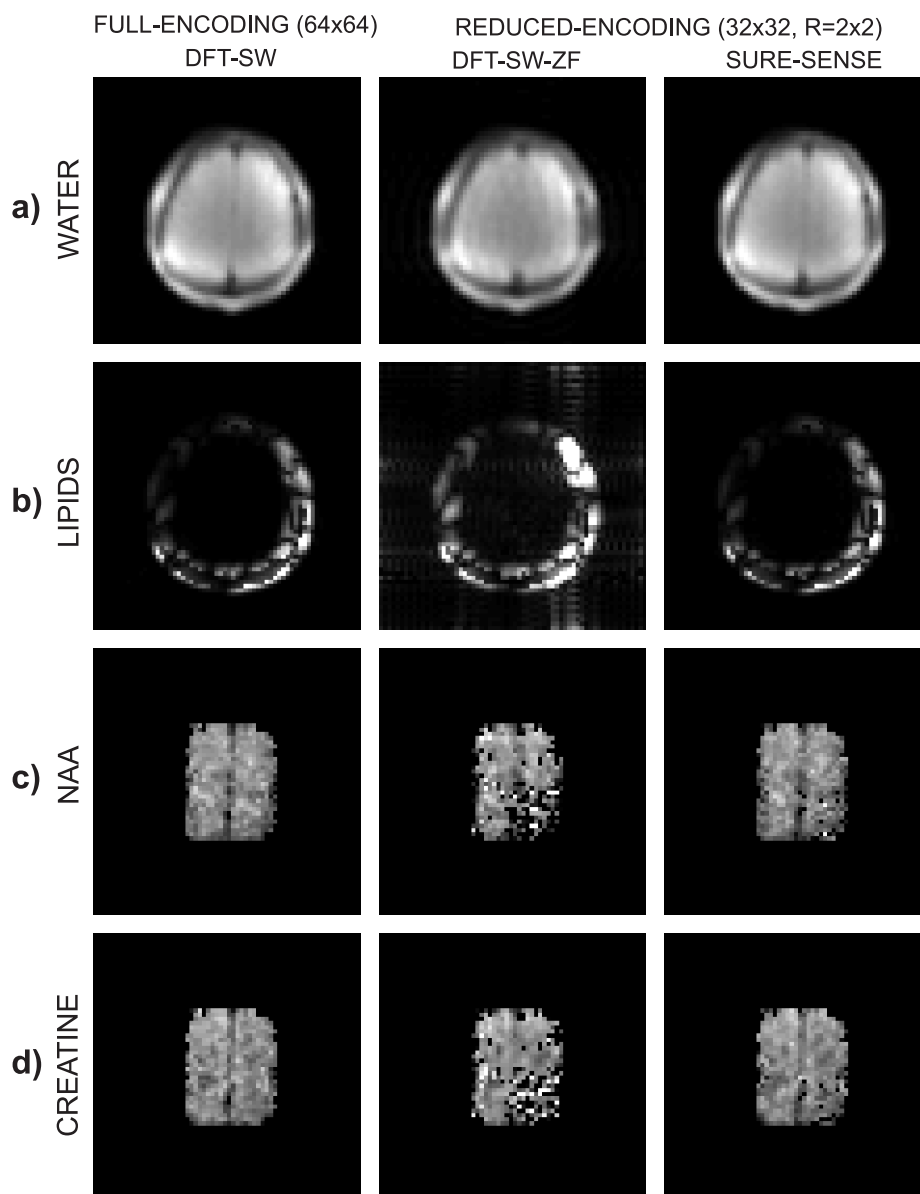


Figure 8.2: Human brain MRSI reconstruction. Conventional DFT with sensitivity-weighting (DFT-SW) reconstruction of the fully-encoded data (spatial-encoding matrix size: 64×64), DFT-SW with zero-filling (DFT-SW-ZF) and superresolution SENSE (SURE-SENSE) reconstruction of the data with reduced spatial encoding (spatial-encoding matrix size: 32×32 , $R = 2 \times 2$) for a) water, b) lipids, c) N-Acetyl-Aspartate (NAA) and d) Creatine.

The maps of NAA and Creatine were very similar to the fully-encoded (64×64) reconstruction. Average error in NAA and Creatine concentration maps were 0.57 mM and 0.45 mM respectively for DFT-SW-ZF, and significantly smaller for SURE-SENSE (0.21 mM and 0.17 mM, respectively).

The accuracy of spectral quantification, indicated by the CRLB from LCModel fitting, decreased with acceleration as expected due to reduced SNR in the reconstructed image as a result of the shorter corresponding data acquisition time. Average CRLB for NAA and Cr were 10.2% and 9.7% respectively for the fully-encoded reconstruction, while 13.7% and 12.4% for SURE-SENSE. However, the high lipid contamination inside the brain from conventional DFT reconstruction of truncated k-space data was reduced 3.1-fold on average by SURE-SENSE, which resulted in better spectral quality and more accurate quantification as shown in Fig. 8.3.

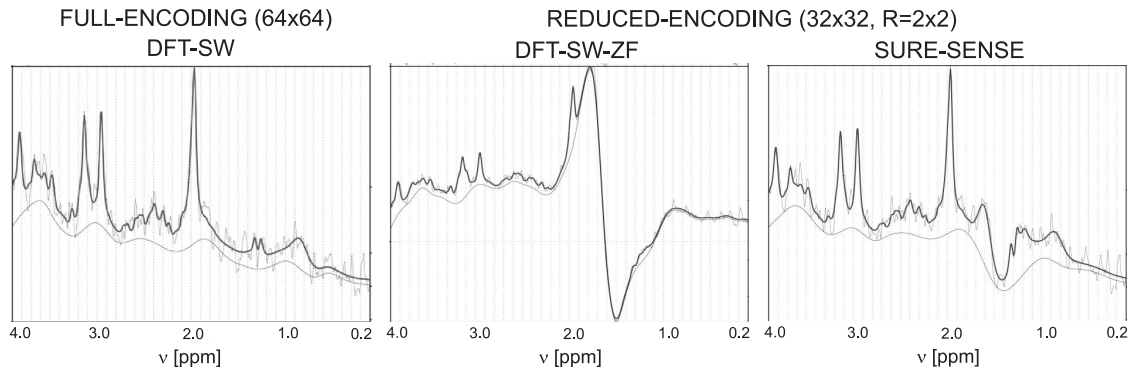


Figure 8.3: Raw absorption mode spectrum (thin black line) and corresponding LCModel fit (bold black line) for a central voxel. The remaining baseline is given by the smooth curve. More than 3-fold reduction in lipid contamination is obtained with SURE-SENSE in comparison to conventional Fourier reconstruction of the low resolution data.

8.6 Discussion

The superresolution SENSE method introduced in Chapter 5 was applied to spectroscopic imaging in human brain, where the effect of limited k-space sampling can be particularly severe due to the presence of an intense signal arising from subcutaneous lipids in the scalp. Superresolution SENSE reconstruction reduced the strong lipid contamination, e.g. 3-fold on average for the implementation given in this work, and improved the spatial resolution of metabolite maps in human brain MRSI when compared to conventional reconstruction of reduced k-space sampling.

Using echo-planar MRSI (PEPSI) and SURE-SENSE reconstruction, metabolite mapping with 0.3 cc of spatial resolution and an equivalent acquisition time of only 1 min was feasible with a spatial-spectral quality comparable to the fully-encoded acquisition. SURE-SENSE will be also advantageous to increase the spectral width in PEPSI especially at high magnetic field since it allows for acceleration along the x dimension which can provide shorter readouts. Future work includes the implementation of SURE-SENSE-PEPSI at 7 Tesla to extend the spectral width limited by the gradient performance at that magnetic field strength.

8.7 Summary

In this Chapter, the superresolution SENSE (SURE-SENSE) method introduced in Chapter 5 is applied to PEPSI encoding for fast metabolic imaging with high spatial resolution in human brain using the 32-channel soccer-ball array. The short acquisition time makes the method suitable for high resolution mapping of metabolites as an add-on in clinical MR studies.

Chapter 9

Conclusions and Future Work

Novel encoding and reconstruction techniques for parallel MRI were investigated in this dissertation. The main goal was to improve the actual reconstruction methods and to develop new approaches for massively parallel MRI systems that take advantage of the higher information content provided by the large number of small receivers. The contributions of this dissertation were distributed in six chapters. The first three contributions are devoted to general parallel MRI reconstruction methods. The last three contributions presented applications for MR spectroscopic imaging.

Parallel MRI reconstruction requires to solve an inverse problem which is susceptible to become ill-conditioned in regions where the information provided by the different coils is similar, e.g. the center of a circular array. Large amplification of noise and effects of systematic errors in coil sensitivity estimation may occur due to instabilities in the inversion process. Regularization of the inverse problem is an essential tool to desensitize the solution from data noise and model errors. Chapter 3 presented a novel method for regularization of the matrix inverse problem based on the SVD representation of the encoding matrix for SENSE reconstruction as an efficient alternative to the commonly used Tikhonov regularization. Note that for

SENSE, where a small system is inverted on each iteration, the common method of truncating the SVD is not appropriate due to the small size of the encoding matrix. The SSVD method shifts the set of singular values of the encoding matrix away from zero using a small portion of the largest singular value. In future work, weighting the set of singular values, e.g. stronger weights to higher singular values, will be considered to optimize the performance of SVD-based regularization for SENSE reconstruction. A two step regularization approach will be also investigated, where first Tikhonov regularization will be applied using prior information about the object being imaged [48] and then the SSVD approach will be applied to improve conditioning of the final matrix inverse problem.

A general framework for parallel MRI with arbitrary k-space sub-sampling was presented in Chapter 4. The reconstruction in this case is computationally intensive since each point in the sub-encoded images can be given by a combination of all the points in the fully-encoded image and the complete encoding matrix needs to be inverted. The iterative reconstruction technique using the conjugate gradient algorithm originally proposed by Pruessmann *et al.* [54] for the case of non-Cartesian sampling was adapted for arbitrary k-space sampling on a Cartesian grid with pre-conditioning to achieve faster convergence. Pre-conditioning represented an efficient way to regularize the inverse problem providing a well-conditioned transformed encoding matrix with all the singular values clustered around a single point. The high performance of the pre-conditioning method is due to the availability of an appropriate transformation matrix which in this case is given by the diagonal projection matrix $\mathbf{E}^H \mathbf{E}$ for the case of full sampling of k-space. In future work, the inclusion of prior information in the forward model such as magnetic field inhomogeneities will be studied. Moreover, computationally efficient implementation of parallel MRI reconstruction with variable k-space sub-sampling using parallel computing will be also investigated.

Uniform sub-sampling of k-space is not optimal for parallel MRI if the coil sensitivities overlap, which is the case in practice. A variable k-space sub-sampling scheme using the k-space density of the coil sensitivities was derived in Chapter 4. The idea is to sample densely at the center of k-space and more sparsely as we move away from the center. This variable density sampling scheme is based on the property that a large portion of the information is concentrated within a small region of low k-space values whereas the edge information is distributed over a much broader region of higher k-space values. The method reduces the mean square error of SENSE reconstruction with uniform k-space sub-sampling and it is particularly suitable for reconstruction with regularization. In future work, a fast algorithm for optimal selection of k-space samples that minimizes the mean square error expression derived in Chapter 4 will be investigated. Moreover, the selection of k-space samples based on other criteria such as contrast enhancement will be a topic of future research.

Parallel MRI has been introduced has a method to accelerate the encoding process by sub-sampling k-space while maintaining the total extent to have the same spatial resolution. The rationale for this sub-encoding scheme is that the coil sensitivity maps are very smooth and retrieve k-space information only from the neighborhood of the actual gradient-encoding point. New array coil designs with a large number of small elements provide stronger variation of the coil sensitivities. In Chapter 5, a novel parallel MRI method known as superresolution sensitivity encoding (SURE-SENSE) was proposed for large-N arrays. In analogy to superresolution image reconstruction from picture and video processing, where multiple low resolution images with sub-pixel differences are combined, parallel MRI reconstruction was formulated as a superresolution problem. While strong sensitivity variation may result in residual aliasing artifacts in conventional parallel MRI method due to sensitivity variation within the image pixel, SURE-SENSE is taking advantage of the stronger sensitivity variation to perform intra-pixel reconstruction. Acceleration in SURE-SENSE is performed by acquiring only the central region of k-space instead

of increasing the sampling distance over the complete k-space matrix. The increase in spatial resolution will be determined by the degree of coil sensitivity variation within the acquired low resolution voxel. Superresolution SENSE is intrinsically an ill-conditioned problem since the intra-pixel variation of the coil sensitivity maps is lower than across aliased points separated by larger distances. Pre-conditioning reduced the g-factor for SURE-SENSE reconstruction close to one at the expense of slight spatial resolution reduction in the reconstructed image due to the attenuation of small singular values, which are related to high spatial frequencies. As we have shown in our results, this tradeoff is quite acceptable when the data is acquired with large-scale array coils that provide strongly modulated coil sensitivity profiles and high SNR. SURE-SENSE compares favorably the performance of standard SENSE reconstruction for low spatial resolution imaging where intra-pixel sensitivity variation is stronger. However, superresolution SENSE is not limited to low resolution MRI as we have shown and future work will characterize the optimal operating regimes of the method. Superresolution parallel MRI reconstruction in k-space and comparison to the proposed spatial-domain reconstruction will be also explored.

MR spectroscopic imaging is constrained by low SNR and slow encoding methods. As a consequence, k-space coverage is sacrificed to achieve an adequate SNR within a feasible acquisition time, which restricts MRSI to low spatial resolution and single slice acquisition in clinical practice. In this dissertation, the Proton Echo Planar Spectroscopic Imaging (PEPSI) technique was improved for fast MRSI in human brain with high spatial resolution using parallel imaging approaches. In Chapter 6, advantages of high field strength such as linear increase in SNR of metabolites and increase in spectral resolution were demonstrated. Moreover, improved spectral fitting was demonstrated by modeling the baseline using macromolecule information acquired experimentally at different magnetic field strengths. Therefore, the use of high magnetic field strength along with improved modeling is expected to provide high accuracy in metabolite concentration estimation. In Chapter 7, 3D-PEPSI was

Chapter 9. Conclusions and Future Work

combined with 2D-SENSE parallel imaging technique using the 32-channel soccer-ball array for volumetric MRSI in clinically feasible acquisition times. The SSVD regularization from Chapter 3 was employed to reduce noise and errors in regions with low-value and overlapped coil sensitivities. As a result, the method improved the reconstruction of the point spread function and reduced lipid contamination inside the brain from peripheral regions. *In vivo* results have demonstrated that single-average 3D-MRSI with a $32 \times 32 \times 8$ spatial matrix and 0.7 cc nominal voxel size at 3 Tesla can be accelerated with minimum acquisition time of 1 min to map the concentrations of the main metabolites. In Chapter 8, the superresolution SENSE method introduced in Chapter 5 was applied to PEPSI encoding using the 32-channel soccer-ball array. SURE-SENSE-PEPSI demonstrated feasibility of metabolite mapping with 0.3 cc of spatial resolution and an acquisition time of only 1 minute. Future work on parallel PEPSI includes the implementation of the technique at 7 Tesla using a 32-channel soccer ball array for mapping of J-coupled metabolites. The spectral width of PEPSI at 7 Tesla could be limited by the gradient performance. SURE-SENSE will be applied to PEPSI at 7 Tesla to provide larger spectral width since it allows for acceleration of the readout dimension.

The contributions presented in this dissertation are expected to provide methods that substantially enhances the utility of parallel MRI for clinical research and to offer a framework for fast MRSI of human brain with high spatial and spectral resolution.

References

- [1] A. Kumar, D. Welte, and R. Ernst. NMR Fourier zeugmatography. *J. Magn. Reson.*, 18:69–85, 1975.
- [2] P. Mansfield. Multi-planar image formation using NMR spin echoes. *Journal of Physics C*, 10:L55–L58, 1977.
- [3] A.B. Ahn, J.H. Kim, and Z.H. Cho. High speed spiral-scan echo planar NMR imaging-I. *IEEE Transactions on Medical Imaging*, MI-5(1):1–6, 1986.
- [4] E. Haacke, R. Brown, M. Thompson, and R. Venkatesan. *Magnetic Resonance Imaging: Physical Principles and Sequence Design*. John Wiley and Sons, 1999.
- [5] Z-P. Liang and P. Lauterbur. *Principles of Magnetic Resonance Imaging: A Signal Processing Perspective*. IEEE Series in Biomedical Engineering, 2000.
- [6] G. Wright. Magnetic Resonance Imaging. *IEEE Signal Process. Mag.*, pages 56–66, January 1997.
- [7] P.C. Lauterbur. Image formation by induced local interactions: examples employing nuclear magnetic resonance. *Nature*, 242:190–191, 1972.
- [8] T.B. Brown, B.M. Kincaid, and K. Ugurbil. NMR chemical shift imaging in three dimensions. *Proc. Natl. Acad. Sci. USA*, 79(11):3523–3526, 1982.
- [9] A.A. Maudsley and S.K. Hilal. Spatially resolved high resolution spectroscopy by four-dimensional NMR. *J. Magn. Reson.*, 51:147–152, 1983.
- [10] S. Ogawa, T.M. Lee, A.R. Kay, and D.W. Tank. Brain magnetic resonance imaging with contrast dependent on blood oxygenation. *Proc. Natl. Acad. Sci. USA*, 87:9868–9872, 1990.

References

- [11] J.W. Belliveau, D.N. Kennedy, R.C. McKinstry, B.R. Buchbinder, R.M. Weisskoff, M.S. Cohen, J.M. Vevea, T.J. Brady, and B.R. Rosen. Functional mapping of the human visual cortex by magnetic resonance imaging. *Science*, 254:716–719, 1991.
- [12] M. Hutchinson and U. Raff. Fast MRI data acquisition using multiple detectors. *Magn. Reson. Med.*, 6(1):87–91, 1988.
- [13] J.R. Kelton, R.L. Magin, and S.M. Wright. An algorithm for rapid image acquisition using multiple receiver coils. In *ISMRM Proceedings*, page 1172, 1989.
- [14] J.B. Ra and C.Y. Rim. Fast imaging using subencoding data sets from multiple detectors. *Magn. Reson. Med.*, 30(1):142–145, 1993.
- [15] D.K. Sodickson and W.J. Manning. Simultaneous acquisition of spatial harmonics (SMASH): fast imaging with radiofrequency coil arrays. *Magn. Reson. Med.*, 38(4):591–603, 1997.
- [16] K.P. Pruessmann, M. Weiger, M.B. Scheidegger, and P. Boesiger. SENSE: sensitivity encoding for fast MRI. *Magn. Reson. Med.*, 42(5):952–962, 1999.
- [17] M. A. Griswold, P. M. Jakob, R. M. Heidemann, M. Nittka, V. Jellus, J. Wang, B. Kiefer, and A. Haase. Generalized autocalibrating partially parallel acquisitions (GRAPPA). *Magn. Reson. Med.*, 47(6):1202–1210, 2002.
- [18] W.E. Kyriakos, L.P. Panych, D.F. Kacher C-F. Westin, S.M. Bao, R.V. Mulkern, and F.A. Jolesz. Sensitivity profiles from an array of coils for encoding and reconstruction in parallel (SPACE RIP). *Magn. Reson. Med.*, 44(2):301–308, 2000.
- [19] N. Aggarwal and Y. Bresler. Accelerated parallel magnetic resonance imaging by adaptive k-space sampling. In *IEEE International Symposium on Biomedical Imaging: Nano to Macro*, pages 892–895, 2004.
- [20] Y. Zhu, C.J. Hardy, D.K. Sodickson, R.O. Giaquinto, C.L. Dumoulin, G. Kenwood, T. Niendorf, H. Lejay, C.A. McKenzie, M.A. Ohliger, and N.M. Rofsky. Highly parallel volumetric imaging with a 32-element RF coil array. *Magn. Reson. Med.*, 52(4):869–877, 2004.
- [21] D.K. Sodickson, C.J. Hardy, Y. Zhu Y, R.O. Giaquinto, P. Gross, G. Kenwood, T. Niendorf, H. Lejay, C.A. McKenzie, M.A. Ohliger, A.K. Grant, and N.M. Rofsky. Rapid volumetric MRI using parallel imaging with order-of-magnitude accelerations and a 32-element RF coil array: feasibility and implications. *Acad. Radiol.*, 12(5):626–635, 2005.

References

- [22] D.K. Sodickson, R.F. Lee, and R.O. Giantino. Depth penetration of RF coils for sequential and parallel MR imaging. In *ISMRM Proceedings*, page 469, 2003.
- [23] F-H. Lin, L.L. Wald, S.P. Ahlfors, M.S. Hamalainen, K.K. Kwong, and J.W. Belliveau. Dynamic magnetic resonance inverse imaging of human brain function. *Magn. Reson. Med.*, 56(4):787–802, 2006.
- [24] L. Wald and G. Wiggins. *Parallel Imaging in Clinical MR Applications*, chapter 44 - New coil systems for highly parallel MR acquisition strategies, pages 497–510. Springer, 2007.
- [25] G.C. Wiggins, C. Triantafyllou, A. Potthast, A. Reykowski, M. Nittka, and L.L. Wald. 32-channel 3 Tesla receive-only phased-array head coil with soccer-ball element geometry. *Magn. Reson. Med.*, 56(1):216–223, 2006.
- [26] G.C. Wiggins, V. Alagappan, A. Potthast, M. Schmitt, C. J. Wiggins, H. Fischer, K. Jahns, T. Benner, J. Polimeni, and L.L. Wald. Design optimization and SNR performance of 3T 96 channel phased array head coils. In *ISMRM Proceedings*, page 243, 2007.
- [27] F. Wiesinger, P.F. Van de Moortele, G. Adriany, N. De Zanche, K. Ugurbil, and K.P. Pruessmann. Parallel imaging performance as a function of field strength - an experimental investigation using electrodynamic scaling. *Magn. Reson. Med.*, 52(5):953–964, 2004.
- [28] J.H. Ardenkjaer-Larsen, B. Fridlund, A. Gram, G. Hansson, L. Hansson, M.H. Lerche, R. Servin, M. Thaning, and K. Golman. Increase in signal-to-noise ratio of $> 10,000$ times in liquid-state NMR. *Proc. Natl. Acad. Sci. USA*, 100(18):10158–10163, 2003.
- [29] S. Posse, R. Tedeschi, R. Risinger, R. Ogg, and D. LeBihan. High speed ^1H spectroscopic imaging in human brain by echo planar spatial-spectral encoding. *Magn. Reson. Med.*, 33(1):34–40, 1995.
- [30] F. Bloch, W. Hansen, and M. Packard. Nuclear induction. *Physics Review*, 69:127, 1946.
- [31] E.M. Purcell, H.C. Torrey, and R.V. Pound. Resonance absorption by nuclear magnetic moments in a solid. *Physics Review*, 69:37–38, 1946.
- [32] J. Jackson, C. Meyer, D.G. Nishimura, and A. Macovski. Selection of a convolution function for Fourier inversion using regridding. *IEEE Trans. Med. Imaging*, 10(3):473–478, 1991.

References

- [33] G.E. Sarty, R. Bennet, and R.W. Cox. Direct reconstruction of non-cartesian k-space data using a nonuniform fast Fourier transform. *Magn. Reson. Med.*, 45(5):908–915, 2001.
- [34] D.K. Sodickson and C.A. McKenzie. A generalized approach to parallel magnetic resonance imaging. *Med. Phys.*, 28(8):1629–1643, 2001.
- [35] K.P. Pruessmann. Encoding and reconstruction in parallel MRI. *NMR Biomed.*, 19(3):288–299, 2006.
- [36] D.J. Larkman and R.G. Nunes. Parallel Magnetic Resonance Imaging. *Phys. Med. Biol.*, 52(7):R15–R55, 2007.
- [37] P.M. Jakob, M.A. Griswold, and R.R. Edelman. AUTO-SMASH: a self-calibrating technique for SMASH imaging. *MAGMA*, 7:42–54, 1998.
- [38] U. Katscher, P. Bornert, C. Leussler, and J.S. van den Brink. Transmit SENSE. *Magn. Reson. Med.*, 49(1):144–150, 2001.
- [39] W.C. Dickinson. Dependence of the F19 nuclear resonance position on chemical compound. *Physics Review*, 77:736, 1950.
- [40] W. Proctor and F.C. Yu. The dependence of a nuclear magnetic resonance frequency upon chemical compound. *Physics Review*, 77:717, 1950.
- [41] A. Haase, J. Frahm, W. Hanicke, and D. Matthaei. ^1H NMR chemical shift selective (CHESS) imaging. *Phys. Med. Biol.*, 30(4):341–344, 1985.
- [42] R.J. Ogg, P.B. Kingsley, and J.S. Taylor. WET, a T1- and B1-insensitive water-suppression method for in vivo localized ^1H NMR spectroscopy. *J. Magn. Reson.*, 104(1):1–10, 1994.
- [43] B. J. Soher, K. Young, and A. A. Maudsley. Representation of Strong Baseline Contributions in ^1H MR Spectra. *Magn. Reson. Med.*, 45(6):966–972, 2001.
- [44] S.W. Provencher. Estimation of metabolite concentrations from localized in vivo proton NMR spectra. *Magn. Reson. Med.*, 30(6):672–679, 1993.
- [45] R. Pohmann, M. von Kienlin, and A. Haase. Theoretical evaluation and comparison of fast chemical shift imaging methods. *J. Magn. Reson.*, 129(2):145–160, 1997.
- [46] P. Mansfield. Spatial mapping of the chemical shift in NMR. *Magn. Reson. Med.*, 1(3):370–386, 1984.

References

- [47] E. Adalsteinsson, P. Irarrazabal, S. Top, C. Meyer, A. Macovski, and D.M. Spielman. Volumetric spectroscopic imaging with spiral-based k-space trajectories. *Magn. Reson. Med.*, 39(6):889–898, 1998.
- [48] F-H. Lin, K.K. Kwong, J.W. Belliveau, and L.L. Wald. Parallel imaging reconstruction using automatic regularization. *Magn. Reson. Med.*, 51(3):559–567, 2004.
- [49] P.C. Hansen. *Rank-Deficient and Discrete Ill-Posed Problems: Numerical Aspects of Linear Inversion*. SIAM, 1998.
- [50] A.N. Tikhonov and V.A. Arsenin. *Solution of Ill-posed Problems*. Winston and Sons, 1977.
- [51] K.F. King and L. Angelos. SENSE image quality improvement using matrix regularization. In *ISMRM Proceedings*, page 1771, 2001.
- [52] L. Ying, D. Xu, and Z-P. Liang. On Tikhonov regularization for image reconstruction in parallel MRI. In *Proceedings of the 26th International Conference of the Engineering in Medicine and Biology Society (IEEE-EMBS)*, pages 1056–1059, 2004.
- [53] W.S. Hoge, D.H. Brooks, B. Madore, and W. Kyriakos. On the regularization of SENSE and SPACE-RIP in parallel imaging. In *IEEE International Symposium on Biomedical Imaging: Nano to Macro*, pages 241–244, 2004.
- [54] K.P. Pruessmann, M. Weiger, P. Bornert, and P. Boesiger. Advances in sensitivity encoding with arbitrary k-space trajectories. *Magn. Reson. Med.*, 46(4):638–651, 2001.
- [55] Y. Saad. *Iterative methods for sparse linear systems*. PWS Publishing Company, 1996.
- [56] Z-P. Liang, F. Boada, T. Constable, E.M. Haacke, P.C. Lauterbur, and M.R. Smith. Constrained reconstruction methods in MR imaging. *Rev. Magn. Reson. Med.*, 4:67–185, 1992.
- [57] S. Plevritis and A. Macovski. Spectral extrapolation of spatially bounded images. *IEEE Trans. Med. Imaging*, 14(3):487–497, 1995.
- [58] R.A. Jones, O. Haraldseth, T.B. Muller, P.A. Rinck, and A.N. Oksendal. K-space substitution: A novel dynamic imaging technique. *Magn. Reson. Med.*, 29(6):830–834, 1993.

References

- [59] Z-P. Liang and P.C. Lauterbur. A generalized series approach to MR spectroscopic imaging. *IEEE Trans. Med. Imaging*, 10(2):132–137, 1991.
- [60] Z-P. Liang and P.C. Lauterbur. An efficient method for dynamic magnetic resonance imaging. *IEEE Trans. Med. Imaging*, 13(4):677–686, 1994.
- [61] M. Elad and A. Feuer. Restoration of a single superresolution image from several blurred, noisy, and undersampled measured images. *IEEE Trans. Image Process.*, 6(12):1646–1658, 1997.
- [62] S.C Park, M.K. Park, and M.G. Kang. Super-resolution image reconstruction: a technical overview. *IEEE Signal Process. Mag.*, 20(3):21–36, 2003.
- [63] S. Peled and Y. Yeshurun. Superresolution in MRI: application to human white matter fiber tract visualization by diffusion tensor imaging. *Magn. Reson. Med.*, 45(1):29–35, 2001.
- [64] H. Greenspan, G. Oz, N. Kiryati, and S. Peled. MRI inter-slice reconstruction using super-resolution. *Magn. Reson. Imaging*, 20(5):437–446, 2002.
- [65] E. Carmi, S. Liu, N. Alon, A. Fiat, and D. Fiat. Resolution enhancement in MRI. *Magn. Reson. Imaging*, 24(2):133–154, 2006.
- [66] X. Zhao, R.W. Prost, Z. Li, and S-J. Li. Reduction of artifacts by optimization of the sensitivity map in sensitivity-encoded spectroscopic imaging. *Magn. Reson. Med.*, 53(1):30–34, 2005.
- [67] J. Sanchez-Gonzalez, J. Tsao, U. Dydak, M. Desco, P. Boesiger, and K.P. Pruessmann. Minimum-norm reconstruction for sensitivity-encoded magnetic resonance spectroscopic imaging. *Magn. Reson. Med.*, 55(2):287–295, 2006.
- [68] M.P McDougall and S.M. Wright. 64-channel array coil for single echo acquisition magnetic resonance imaging. *Magn. Reson. Med.*, 54(2):386–392, 2005.
- [69] D. Hoult and P. Lauterbur. The sensitivity of the zeugmatographic experiment involving human samples. *J. Magn. Reson.*, 34:425–433, 1979.
- [70] W.A. Edelstein, G.H. Glover, C.J. Hardy, and R.W. Redington. The intrinsic signal-to-noise ratio in NMR imaging. *Magn. Reson. Med.*, 3(4):604–618, 1986.
- [71] O. Ocali and E. Atalar. Ultimate intrinsic signal-to-noise ratio in MRI. *Magn. Reson. Med.*, 39(3):462–473, 1998.
- [72] D. Hoult and D. Phil. Sensitivity and power deposition in a high-field imaging experiment. *J. Magn. Reson. Imaging*, 12(1):46–67, 2000.

References

- [73] K. Ugurbil, G. Adriany, P. Andersen, W. Chen, M. Garwood, R. Gruetter, P.G. Henry, S.G. Kim, H. Lieu, I. Tkac, T. Vaughan, P.F. Van De Moortele, E. Yacoub, and X.P. Zhu. Ultrahigh field magnetic resonance imaging and spectroscopy. *Magn. Reson. Imaging*, 21(10):1263–1281, 2003.
- [74] J.T. Vaughan, M. Garwood, C.M. Collins, W. Liu, L. DelaBarre, G. Adriany, P. Andersen, H. Merkle, R. Goebel, M.B. Smith, and K. Ugurbil. 7T vs. 4T: RF power, homogeneity, and signal-to-noise comparison in head images. *Magn. Reson. Med.*, 46(1):24–30, 2001.
- [75] P.B. Barker, D.O. Hearshen, and M.D. Boska MD. Single-voxel proton MRS of the human brain at 1.5T and 3.0T. *Magn. Reson. Med.*, 45(5):765–769, 2001.
- [76] O. Gonen, S. Gruber, B.S. Li, V. Mlynarik, and E. Moser. Multivoxel 3D proton spectroscopy in the brain at 1.5 versus 3.0 T: signal-to-noise ratio and resolution comparison. *AJNR Am J Neuroradiol*, 22:1727–1731, 2001.
- [77] S. Posse, C.A. Cuenod, R. Risinger, D. Le Bihan, and R.S. Balaban. Anomalous transverse relaxation in ^1H spectroscopy in human brain at 4 Tesla. *Magn. Reson. Med.*, 33(2):246–252, 1995.
- [78] H.P. Hetherington, J.W. Pan, W.J. Chu, G.F. Mason, and B.R. Newcomer. Biological and clinical MRS at ultra-high field. *NMR Biomed.*, 10(8):360–371, 1997.
- [79] R. Gruetter, S.A. Weisdorf, V. Rajanayagan, M. Terpstra, H. Merkle, C.L. Truwit, M. Garwood, S.L. Nyberg, and K. Ugurbil. Resolution improvements in *in vivo* ^1H NMR spectra with increased magnetic field strength. *J. Magn. Reson.*, 135(1):260–264, 1998.
- [80] R. Bartha, D.J. Drost, R.S. Menon, and P.C. Williamson. Comparison of the quantification precision of human short echo time ^1H spectroscopy at 1.5 and 4.0 Tesla. *Magn. Reson. Med.*, 44(2):185–192, 2000.
- [81] U. Klose. In vivo proton spectroscopy in presence of eddy currents. *Magn. Reson. Med.*, 14(1):26–30, 1990.
- [82] C.I. Haupt, N. Schuff, M.W. Weiner, and A.A. Maudsley. Removal of lipid artifacts in ^1H spectroscopic imaging by data extrapolation. *Magn. Reson. Med.*, 35(5):678–687, 1996.
- [83] P.B. Roemer, W.A. Edelstein, C.E. Hayes, S.P. Souza, and O.M. Mueller. The NMR phased array. *Magn. Reson. Med.*, 16(2):192–225, 1990.

References

- [84] A. Naressi, C. Couturier, J.M. Devos, M. Janssen, C. Mangeat, R. de Beer, and D. Graveron-Demilly. Java-based graphical user interface for the MRUI quantitation package. *12*:141–152, 2001.
- [85] L. Vanhamme, R.D. Fierro, S. Van Huffel, and R. de Beer. Fast removal of residual water in proton spectra. *J. Magn. Reson.*, 132:197–203, 1998.
- [86] H. Ratiney, M. Sdika, Y. Coenradie, S. Cavassila, D. van Ormondt, and D. Graveron-Demilly. Time-domain semi-parametric estimation based on a metabolite basis set. *NMR Biomed.*, 18:1–13, 2005.
- [87] D. Graveron-Demilly, A. Diop, A. Briguet, and B. Fenet. Product-operator algebra for strongly coupled spin systems. *J. Magn. Reson.*, A101:233–239, 1993.
- [88] V. Govindaraju, K. Young, and A.A. Maudsley. Proton NMR chemical shifts and coupling constants for brain metabolites. *NMR Biomed.*, 13(3):129–153, 2000.
- [89] U. Seeger, U. Klose, I. Mader, W. Grodd, and T. Nagele. Parameterized evaluation of macromolecules and lipids in proton MR spectroscopy of brain diseases. *Magn. Reson. Med.*, 49:19–28, 2003.
- [90] A. Macovski. Noise in MRI. *Magn. Reson. Med.*, 36(3):494–497, 1996.
- [91] T. Ethofer, I. Mader, U. Seeger, G. Helms M. Erb, W. Grodd, A. Ludolph, and U. Klose. Comparison of longitudinal metabolite relaxation times in different regions of the human brain at 1.5 Tesla and 3 Tesla. *Magn. Reson. Med.*, 50:1296–1301, 2003.
- [92] V. Mlynarik, S. Gruber, and E. Moser. Proton T1 and T2 relaxation times of human brain metabolites at 3 Tesla. *NMR Biomed.*, 14:325–331, 2001.
- [93] S. Michaeli, M. Garwood, X.H. Zhu, L. DelaBarre, P. Andersen, G. Adriany, H. Merkle, K. Ugurbil, and W. Chen. Proton T2 relaxation study of water, N-acetylaspartate, and creatine in human brain using Hahn and Carr-Purcell spin echoes at 4T and 7T. *Magn. Reson. Med.*, 47(4):629–633, 2002.
- [94] J.G. Pipe and J.L. Duerk. Analytical resolution and noise characteristics of linearly reconstructed magnetic resonance data with arbitrary k-space sampling. *Magn. Reson. Med.*, 34(1):170–178, 1995.
- [95] U. Dydak, M. Weiger, K.P. Pruessmann, D. Meier, and P. Boesiger. Sensitivity-encoded spectroscopic imaging. *Magn. Reson. Med.*, 46(4):713–722, 2001.

References

- [96] U. Dydak, K.P. Pruessmann, M. Weiger, J. Tsao, D. Meier, and P. Boesiger. Parallel spectroscopic imaging with spin-echo trains. *Magn. Reson. Med.*, 50(1):196–200, 2003.
- [97] U. Dydak. Parallel Spectroscopic Imaging. In *2nd International Workshop on Parallel MRI*, pages 120–121, 2004.
- [98] M. Weiger, K.P. Pruessmann, and P. Boesiger. 2D SENSE for faster 3D MRI. *MAGMA*, 45(3):495–504, 2001.
- [99] J.A. de Zwart, P.J. Ledden, P. Kellman, P. van Gelderen, and J.H. Duyn. Design of a SENSE-optimized high-sensitivity MRI receive coil for brain imaging. *Magn. Reson. Med.*, 47:1218–1227, 2002.
- [100] P.G. Henry, M. Marjanska, J.D. Walls, J. Valette, R. Gruetter, and K. Ugurbil. Proton-observed carbon-edited NMR spectroscopy in strongly coupled second-order spin systems. *Magn. Reson. Med.*, 45(2):250–257, 2006.
- [101] B. J. Soher, P. van Zijl, D.H. Duyn, and P.B. Barker. Quantitative proton MR spectroscopic imaging of the human brain. *Magn. Reson. Med.*, 35(3):356–363, 1996.
- [102] M.A. McLean, F.G. Woermann, G.J. Barker, and J.S. Duncan. Quantitative analysis of short echo time 1H-MRSI of cerebral gray and white matter. *Magn. Reson. Med.*, 44(3):401–411, 2000.
- [103] A. Ebel and A.A. Maudsley. Comparison of methods for reduction of lipid contamination for in vivo proton MR spectroscopic imaging of the brain. *Magn. Reson. Med.*, 46(4):706–712, 2001.
- [104] A. Ebel, A. Govindaraju, and A.A. Maudsley. Comparison of inversion recovery preparation schemes for lipid suppression in 1H MRSI of human brain. *Magn. Reson. Med.*, 49(5):903–908, 2003.
- [105] D.C. Shungu and J.D. Glickson. Sensitivity and localization enhancement in multinuclear in vivo NMR spectroscopy by outer volume presaturation. *Magn. Reson. Med.*, 30(6):661–671, 1993.
- [106] S. Posse, R. Otazo, A. Caprihan, J. Bustillo, H. Chen, P.G. Henry, M. Marjanska, C. Gasparovic, C. Zuo, V. Magnotta, B. Mueller, P. Mullins, P. Renshaw, K. Ugurbil, K.O. Lim, and J.R. Alger. Proton echo-planar spectroscopic imaging of J-coupled resonances in human brain at 3 and 4 Tesla. *Magn. Reson. Med.*, 58(2):236–244, 2007.